NOTE TO USERS

This reproduction is the best copy available.

UMI®

FROM ASTEROIDS TO COMETS: GAS AND DUST PRODUCTION

OF THE SMALL-BODIES IN THE SOLAR SYSTEM

(Spine title: From Asteroids to Comets)

(Thesis format: Integrated-Article)

by

Alyssa M. Gilbert

Graduate Program in Astronomy

A thesis submitted in partial fulfillment
of the requirements for the degree of
Doctor of Philosophy

The School of Graduate and Postdoctoral Studies
The University of Western Ontario
London, Ontario, Canada

Canada

THE UNIVERSITY OF WESTERN ONTARIO
School of Graduate and Postdoctoral Studies

CERTIFICATE OF EXAMINATION

<u>Supervisor</u>

_____
Dr. Paul Wiegert

Supervisory Committee

_____
Dr. Peter Brown

_____
Dr. Aaron Sigut

<u>Examiners</u>

_____
Dr. Margaret Campbell-Brown

_____
Dr. Martin Houde

_____
Dr. JJ Kavelaars

_____
Dr. Lalu Mansinha

The thesis by

Alyssa Marie <u>Gilbert</u>

entitled:

From Asteroids to Comets: Gas and Dust Production of the

Small-Bodies in the Solar System

is accepted in partial fulfillment of the
requirements for the degree of
Doctor of Philosophy

_____
Date

_____
Chair of the Thesis Examination Board

Abstract

Comets are considered to be among the most pristine objects in our Solar System. Active comets have been studied for centuries, but the topic of transition objects (TOs) is relatively new in the area of planetary science. In either case, understanding the composition, activity and dynamics of these objects will help us understand the physical and dynamical evolution of comets, their connection to asteroids, and the environment and formation of the early Solar System.

The overall theme of this thesis is to search for and study cometary activity on small-bodies in our Solar System. In particular, three separate, but related, projects are presented. Two studies utilized spectroscopic observations from the 1.2 m Elginfield telescope, the 1.8 m Dominion Astrophysical Observatory (DAO), and the 1.5 m Cerro-Tololo Inter-American Observatory (CTIO), to search for TOs and/or to observe active comets at different points in their orbit and of different dynamical ages. A third study used archived images from the Canada-France-Hawaii Telescope Legacy Survey (CFHTLS) to search for cometary activity on objects otherwise classified as asteroids.

1. The Elginfield and DAO telescopes were used to test the feasibility of a spec-

troscopic search program for TOs from these platforms. Even in this initial test mode, the data collected constitutes the largest spectroscopic search for TOs to date. However, previous results could not be improved upon, and this project was not deemed feasible with the current observations.

2. Five active comets were observed spectroscopically with the CTIO. Of particular interest were observations of new Oort cloud comet, 2006 VZ13, which passed perihelion during these observations. Gas and dust production rates and ratios were derived for three molecular species (CN, C_2, and C_3), and each comet was classified based on criteria from previous studies.

3. Using the CFHTLS, over 950 asteroidal objects were examined for evidence of comae or tail using a three-level technique, while over 11,000 objects were visually inspected. This is the largest search for main-belt comets (MBCs) of any kind to date, which also examined the general main-belt population. One unknown object was found to show cometary activity. Upper limits were derived for the expected number of weakly and strongly active MBCs in the main-belt.

Key words: Comets, asteroids, transition objects, main-belt comets, activated asteroids, solar system, cometary activity, physical evolution, orbit, Jupiter Tisserand parameter, optical spectra, optical observations, emission lines, gas production rate, dust production rate, Elginfield telescope, Dominion Astrophysical Observatory, Cerro-Tololo Inter-American Observatory, Canada-France-Hawaii Telescope, Legacy Survey, spectrograph, CCD camera.

iv

Coauthorship

This thesis contains material from the following manuscripts:

- Gilbert, A.M., Wiegert, P.A. 2009. Searching for main-belt comets using the Canada-France-Hawaii Telescope Legacy Survey. Icarus 201, 714-718.

- Gilbert, A.M., Wiegert, P.A., Unda-Sanzana, E., Vaduvescu, O. 2009. Spectroscopic observations of new Oort cloud comet 2006 VZ13 and four other comets. Submitted to MNRAS.

These manuscripts are reproduced, in their entirety or portions thereof, in Chapters 1 − 4. All manuscripts were written by Alyssa Gilbert. All data acquisition, reduction, and analysis was performed by Alyssa Gilbert with the exception of the following:

In Chapter 2, Mike Debruyne helped test the SBIG spectrograph and CCD and mount them on the Elginfield telescope. Brian Dalrymple created the mounting device. David Balem provided the system efficiency function and atmospheric extinction for the SITe-2 and SITe-5 CCDs at the DAO.

In Chapter 3, Eduardo Unda-Sanzana and Ovidiu Vaduvescu were instrumental in getting observing time on the CTIO telescope. Claudio Aguilera and Alberto

Mitranda acquired the data.

In Chapter 4, the data was acquired with MegaCam, a joint project of CFHT and CEA/DAPNIA, at the CFHT which is operated by the National Research Council (NRC) of Canada, the Institut National des Science de l'Univers of the Centre National de la Recherche Scientifique (CNRS) of France, and the University of Hawaii. This work is based in part on data products produced at TERAPIX and the CASD as part of the CFHTLS, a collaborative project of NRC and CNRS. Source Extractor and computer code written by Paul Wiegert were used to search the images for asteroids. Paul Wiegert also calculated the orbit of the unknown comet. David Clark helped search the CFHT archives for images of the (then) three known main-belt comets and the unknown comet.

Paul Wiegert contributed ideas throughout this thesis work.

To my parents, for their continued support;
and to my husband, who never let me give up.

Thou too, O Comet, beautiful and fierce,
Who drew the heart of this frail Universe
Towards thine own; till, wrecked in that convulsion,
Alternating attraction and repulsion,
Thine went astray, and that was rent in twain;
Oh, float into our azure heaven again!

- Percy Shelley, *Epipsychidion*, 1821.

Acknowledgements

First and foremost, I would like to thank my PhD supervisor, Dr. Paul Wiegert, for all of his help and support throughout my thesis work. His dedication to his students, and to their learning, is unmatched. He has a keen ability to say exactly what is needed to be heard, especially in times of crisis - which there are many in graduate school! I am fortunate to have worked with him over the past four years.

I would like to thank the members of my advisory committee, Dr. Peter Brown and Dr. Aaron Sigut, for their input and advice throughout this process. Also many thanks to Dr. John Landstreet for his helpful meetings and emails while I was on the bottom of IRAF's very steep learning curve, and to Dr. David Gray for his help with the Elginfield telescope, and for great advice about observational astronomy in general.

There are some key people that have helped me with this thesis that I would like to acknowledge: Dave Balem and Dmitry Monin for help with the DAO telescope and data reduction; Kevin Brown and Mike Debruyne for ideas and advice regarding the Elginfield telescope; Rob Weryk and Wayne Edwards for their insight and computer programming advice; Alan Chamberlin for providing his PhD thesis; and many others

that have given advice or suggestions along the way.

On a more personal note, I am extremely thankful for my parent's boundless support and encouragement over the last 30 years. I am grateful for the opportunities they have given me throughout my life, which have molded me into the person I am today. I hope that I make them as proud as I am of them each and every day. I also am thankful for my brother, who is great at all the things I am not; and, for their unconditional, and sometimes annoyingly in-your-face, love, I thank my cats (past and present): Kitt, Nikki, Othello, Claude, Isaac, and Isabella.

Finally, I was blessed, as I was working on my PhD thesis, to have met my husband, Kyle Gilbert. His strength, encouragement, determination, humor, and great patience have helped me through the past few years. If it were not for him, I sincerely believe that I would not be writing this thesis. I look forward to what life will bring for us.

For my Master's thesis, I studied an X-ray binary system that is 10,000 light years away. For my PhD, I wanted to come home - or at least to our Solar System! Comets have always been a sense of wonder and amazement for me because, even though they have been observed for thousands of years, we still know relatively little about them. The past four years have been full of many ups and downs, but in the end it was an amazing journey. This thesis is the culmination of blood, sweat, tears, and laughter, and it is my great pleasure to be able to share it with my friends, family, and colleagues.

Table of Contents

List of Tables

List of Figures

List of Abbreviations and Symbols

AA	Activated Asteroid
AU	Astronomical Unit (1.49598×10^8 km)
CADC	Canadian Astronomical Data Centre
CASD	Center for Astronomy
CCD	Charged Coupled Device
CEA	Commissariat à l'Énergie Atomique
CFHT	Canada-France-Hawaii Telescope
CFHTLS	Canada-France-Hawaii Telescope Legacy Survey
CNRS	Centre National de la Recherche Scientifique
CTIO	Cerro-Tololo Inter-American Observatory
DAO	Dominion Astrophysical Observatory
DAPNIA	Institut de Recherche sur les Lois Fondamentales de l'Univers
Dec	Declination
EC	Ecliptic Comet
EOC	Evolved Oort Cloud (comet)
FOV	Field of View
FWHM	Full-Width-Half-Maximum
HTC	Halley-Type Comet
IRAF	Image Reduction and Analysis Facility
JFC	Jupiter Family Comet
JPL	Jet Propulsion Laboratory
KB	Kuiper Belt
LPC	Long Period Comet
MBA	Main-Belt Asteroid
MBC	Main-Belt Comet
MPC	Minor Planet Center
NEO	Near-Earth Object
NIC	Nearly Isotropic Comet
NOC	New Oort Cloud (comet)
NRC	National Research Council
OC	Oort Cloud
RA	Right Ascension
RMS	Root Mean Square
SBIG	Santa-Barbara Instrument Group
SD	Scattered Disk

SGS	Self-Guided Spectrograph
SPC	Short Period Comet
TERAPIX	Traitement Élémentaire, Réduction et Analyse des PIXels de megacam
TO	Transition Object
UT	Universal Time
VW	Very Wide

a	semi-major axis
a_J	semi-major axis of Jupiter
$\bar{a}$	weighted mean grain radius
A	bond albedo; telescope aperture
$Af\rho$	effective dust scattering area
dM/dt	mass loss rate
D	diameter of body
e	eccentricity
E	energy
$\mathrm{Ei}(x)$	exponential integral
Exp.	exposure time
f	filling factor
F	absolute flux
F_λ	mean flux in wavelength band
$F_\odot$	solar flux
g	g-factor (fluorescence efficiency)
h	Planck's constant (6.6262×10^{-27} erg s^{-1})
i	inclination
l	scale length
L	luminosity
$M_\oplus$	mass of the Earth (5.974×10^{24} kg)
mol(s)	short for molecule(s)
n	numerical representation of planets
$n(r)$	number density
N	number of molecules
N_c	molecular column density
N_p	number of photons
q	perihelion distance
Q	aphelion distance; production rate
r_e	effective radius
r_H	heliocentric distance
r_o	radius of coma
R_o	radius of slit at distance of object
sr	steradian
T	time of perihelion passage; exposure time; T value (in T test)
T_J	Jupiter Tisserand parameter

U	relative velocity
V	absolute magnitude in the visible band
v_e	molecule expansion velocity
$\bar{x}$	mean
X	constant of integration
$\mathring{A}$	angstroms
α	risk factor
Δ	geocentric distance
Δv	vibrational transition
η	ratio of scattering cross sections
θ	slit width
λ	wavelength
ν	frequency; degrees of freedom
ρ	linear radius of telescope aperture at object; grain density
σ	standard deviation
τ	lifetime of molecule
ϕ	projected radius of object
ω	argument of perihelion
Ω	longitude of ascending node; solid angle of aperture
$'$	arcminutes
$''$	arcseconds

Chapter 1

Introduction

Who vagrant transitory comets sees,
Wonders because they're rare; but a new star
Whose motion with the firmament agrees,
Is miracle; for there no new things are.

- John Donne, *To the Countess of Huntingdon*, 1633.

1.1 Motivation

The overall theme of this thesis is the study of cometary activity on the small-bodies

(asteroids and comets) in our Solar System. The study of these objects is fundamental

to our understanding the formation and evolution of planetary systems, including our

own. The Sun and planets have been subjected to substantial alterations over the

past 4.5 billion years since they formed. The small-bodies, on the other hand, are

geologically quiet, and have remained relatively unchanged since their formation.

Key information can be obtained from the small-bodies that has been erased from

the larger ones. Comets in particular are considered to be among the most primitive objects in our Solar System because they formed at vast distances from the Sun, where the relatively cold temperatures preserved the pristine chemical conditions.

Asteroids and comets likely formed in different regions of the early Solar System, providing a picture of the composition with distance from the Sun. Even though the small-bodies have very different distributions in the Solar System, they almost certainly form a continuum: from the very rocky to the very icy. Very few intermittently active objects (known as transitional objects, main-belt comets, or activated asteroids) are known. Determining physical and chemical properties of these small-bodies is important to the understanding of the formation of planetary systems, both of our own and in general.

In addition, the orbital structure of the small-body reservoirs (asteroid belt, Kuiper belt, and Oort cloud - discussed in the following sections) gives information on the dynamical processes that occurred in the early Solar System, such as the migration (movement) of the giant planets, close encounters between the Sun and nearby stars, or gravitational effects from galactic tides (still an effect today).

Finally, one of the prevailing theories for the source of water on Earth is that it originates from the impact of bodies rich in water ice. Whether this is from comets or asteroids with ices is still unknown; however, a complete understanding of small-body evolution will answer this question. In addition, icy bodies are a rich source of complex hydrocarbons (organic compounds) which, along with water, are the seed chemicals for the origin of life.

The following chapter is a review of cometary and asteroidal astronomy. It is

not meant to be comprehensive; instead, it acts as an introduction to the topics pertinent to this thesis. For further details on the subject, and related topics, several books and compendiums can be consulted (Bottke et al., 2002; Brandt & Chapman, 2004; Festou, Keller & Weaver, 2004; de Pater & Lissauer, 2005; Fernández, 2005; McFadden, Weissman & Johnson, 2007; Jewitt, Morbidelli & Rauer, 2008).

1.2   Historical Overview

This section is meant to give a short summary of the history of the small-bodies in our Solar System: comets and asteroids. For a more comprehensive review, see Sagan & Druyan (1985), Bottke et al. (2002), Brandt & Chapman (2004), Festou, Keller & Weaver (2004), and references therein.

1.2.1   Comets

For most of human history, comets have been observed with awe and mystery. Many people, including Aristotle (384-322 B.C.), believed that comets were an omen of an impending disaster. When comets were visible in the night sky, they often became common subjects in paintings and other art. Figure 1.1 depicts comet Halley during its 1456 passing.

Cometary Movement

Early philosophers, such as the Babylonians, Pythagoreans, and Hippocrates, all believed that comets were planet-like, with orbits, but appeared infrequently. However, it was Aristotle's views that would continue to be accepted for over two thousand

Figure 1.1: Painting of Comet Halley following apparition of 1456. Artist unknown. Available from www.barry.warmkessel.com.

years. He believed, since comets were continually changing and the heavens could not, that comets were in fact an atmospheric phenomenon.

It was not until the passing of The Great Comet of 1577 that views changed. Tycho Brahe (1546-1601) used measurements of the comet's position obtained by himself and others to calculate its distance from Earth, and found it to be at least four times the distance to the Moon. He also derived an orbit for the object that was non-circular, or oval (the first time an astronomer suggested that a celestial body might not move in a circular orbit). His work was confirmed by many astronomers shortly thereafter, but some astronomers, including Johannes Kepler (1571-1630) and Galileo Galilei (1564-1642), disagreed on how comets moved in the heavens.

Kepler derived elliptical orbits for the planets, but he did not believe other bodies in the Solar System were governed by the same laws. Other astronomers, such as Giovanni Borelli (1608-1679), Johannes Hevelius (1611-1687), and Giovanni Domenico Cassini (1625-1712), hypothesized comets indeed moved on elliptical or even parabolic paths (see section 1.5.1). Isaac Newton (1642-1727) demonstrated that an object obeying his universal law of gravitation must follow a path indicated by one of the conic sections (circle, ellipse, parabola, or hyperbola). Edmond Halley (1656-1742) made computations based on Newton's theory and was able to predict comet positions to within 5 arcminutes. He also predicted comet Halley's return in 1759 and, when it did, comets were understood to be subject to the laws of physics, not as omens of disaster or evil.

Tail and Coma

It was well known by the sixteenth century that comet tails always pointed away from the Sun. In 1550, Gerolamo Cardano (1501-1576) was one of the first astronomers to postulate that comets were *"...a globe formed in the sky and illuminated by the Sun, the rays of which, shining through the comet, give the appearance of a beard or tail."* (Hellman, 1944). Tycho also suggested that the tails are caused by sunshine passing through the comet. Kepler had a very modern view of the formation of the tails: *"The direct rays strike upon it, penetrate its substance, draw away with them a portion of this matter, and issue thence to form the track of light we call the tail of the comet."* (Oliver, 1930). Newton observed the brightness of comets was related to their distance from the Sun, and also concluded that the tails originated from the atmosphere of comets.

In 1835, however, F. W. Bessel's (1784-1846) observations of Halley's Comet included much more detailed information. He noted structures such as rays, jets, fans, cones, and other forms near the nucleus. These features were also recorded by other astronomers, and it was hypothesized that they were caused by an electrical force, perhaps from the Sun. Later, in 1900, Svante Arrhenius (1859-1927) suggested this repulsive force was the radiation pressure of sunlight.

As cometary spectroscopy developed through the beginning of the twentieth century, it was learned the long, straight tails of comets were composed of ionized molecules, while the broad, curved tails were composed of dust. In 1929, Herman Zanstra (1894-1972) showed fluorescence fully accounted for the emission lines observed in the spectra of comets (Zanstra, 1929). This basic picture of the physical

composition of comets would be built upon through subsequent years (see sections 1.4 and 1.7).

Modern Era

The modern era of our understanding of comets began in the 1950s with three major advances in cometary science: the icy-conglomerate model of the nucleus (Whipple, 1950a,b, 1955), the concept of the Oort cloud as a reservoir for comets (Oort, 1950), and the discovery of the solar wind (Biermann, 1951). The following sections will discuss advances in our understanding of comets, and related topics, that are pertinent to this thesis.

1.2.2 Asteroids

In 1596, Kepler was the first to suggest the existence of a missing planet between the orbits of Mars and Jupiter (Kepler, 1596). Almost two hundred years later, Johann Daniel Titius (1729-1796) noticed an apparent mathematical sequence representing the orbital distances of the planets from the Sun. This was popularized by Johann Elert Bode (1747-1826), and is known as the Titius-Bode law:

$$a = \frac{4 + 3(2^n)}{10},$$
(1.1)

where a is the semi-major axis (distance from the Sun in AU) and n is a numerical representation of each planet (Mercury $= -\infty$, Venus $= 0$, Earth $= 1$, and so on). This law correctly predicted the distances of all the known planets at the time (Mercury at ~ 0.4 AU, Venus at ~ 0.7 AU, etc.), but also predicted the existence of a planet at 2.8 AU from the Sun, between the orbits of Mars and Jupiter.

The orbit of Uranus, which was discovered in 1791, seemingly confirmed this relation, and reinforced the expectation for a planet between Mars and Jupiter. Many astronomers began to search for this missing planet, and Ceres was discovered (with $a = 2.77$ AU) by Giuseppe Piazzi (1746-1826) in 1801. Three other asteroids were found over the next six years: Pallas, Juno, and Vesta. In 1891, Maximilian Wolf (1863-1932) began a search for asteroids using photography, and found almost 250 asteroids between Mars and Jupiter. This region is now known as the main asteroid belt (or main-belt) where it is estimated to house $\sim 10^6$ asteroids with diameters larger than 1 km (Cheng, 2004).

1.3   Formation of the Solar System

The origin and formation of the Solar System is one of the most fundamental problems in astronomy, and is crucial for understanding how life on Earth originated. Our models of Solar System and planetary formation are based on our planetary system, as well as observations of circumstellar disks, other planetary systems, and star forming regions. Any theory for the formation of our Solar System must explain: motions and spacing of orbits; planetary rotation; age (dating from rocks); sizes and densities of planets; the asteroid belt; comets; satellite systems; meteorites; composition; geological (surface) structure; and angular momentum distribution (de Pater & Lissauer, 2005).

The current accepted model of the formation of the Solar System is known as the nebular hypothesis (Alfvén, 1963). In short, it begins in dense molecular clouds (cold,

dark clouds within the Milky Way galaxy where molecules, typically H_2, are formed). When the pressure in a small region of the cloud (known as the proto-solar nebula) is small relative to gravity, the cloud collapses, and spins faster through conservation of angular momentum. The gas and dust in the disk collide and coalesce (grow together, or fuse) in the proto-planetary disk. These particles continue to accrete into the small-bodies (asteroids and comets) and planets.

The process of gas and dust creating the small-bodies and planets is important to this thesis, and is discussed more thoroughly here. For more extensive coverage of Solar System formation, see Part II of Festou, Keller & Weaver (2004), Chapter 12 of de Pater & Lissauer (2005), Chambers & Halliday (2007), and references therein. The following information is compiled using these references.

As the disk cools, compounds will condense into microscopic grains. Assuming the disk is of solar composition (i.e., mass fractions of approximately 0.73, 0.25, and 0.02 for hydrogen, helium, and other elements, respectively), the first condensates are silicates and iron compounds. In the outer portion of the disk, temperatures are much lower, and large quantities of water ice and other ices condense. The distance from the Sun at which water ice will condense is known as the snowline, and is generally assumed to be 3 AU. Small, solid bodies grow from inelastic collisions between the particles to form km-sized bodies (planetesimals). At this point, gas drag and gravity from the Sun are the dominant forces.

As the mass of the planetesimals increases, their gravity becomes more important because it increases the relative velocities and collisional rates between the bodies. Some objects grow large enough to dominate the evolution of the objects close by,

and these are called planetary embryos. These embryos continue to collide with each other and grow into planetary cores (proto-planets).

The cores of the largest proto-planets begin to accrete hydrogen and helium envelopes. The terrestrial planets (Mercury, Venus, Earth, and Mars) are too small to hold hydrogen and helium in their atmospheres. However, the cores of the larger, gas giant planets (Jupiter, Saturn, Uranus, and Neptune) do have sufficient mass, and the accretion rapidly increases their mass and size.

As mentioned above, the Titius-Bode law predicts a planet between Mars and Jupiter. We now know there are millions of asteroids in this region, but the total mass of these bodies is $< 10^{-3}$ $M_\oplus$ (where $M_\oplus$ is the mass of the Earth, 5.974×10^{24} kg). Assuming the distribution of gas and dust in the proto-planetary disk was smooth, the currently observed mass of the main-belt is far less (i.e., $\lesssim 0.1\%$) than would be expected for a planet at that distance. The orbits of the asteroids are also more eccentric and inclined to the plane of the Solar System compared to those of the planets. Proximity to Jupiter is most likely the cause of both the mass depletion and orbital properties. Gravitational perturbations from Jupiter can cause the orbits of the objects to become Jupiter-crossing, or can increase the collisional velocities of the small-bodies. The former objects would interact with Jupiter and either be accreted or ejected from the Solar System, while the latter could cause high-velocity collisions that would vaporize the asteroids.

Planetesimals formed between $3 - 30$ AU from the Sun could be ejected from the planetary region by gravitational interactions with the giant gas planets. Most of the small-bodies near Jupiter and Saturn were ejected from the Solar System. The

objects near Uranus and Neptune received smaller gravitational kicks, and their semi-major axes (a) evolved in a random-walk fashion. When their $a \sim 10^4$ AU, galactic perturbations lift their perihelion distance (q) out of the Solar System. This formed the Oort cloud (OC), where comets are stored for billions of years. Planetesimals formed beyond the orbit of Neptune ($a > 30$ AU) created the Kuiper belt (KB) and scattered disk (SD). See section 1.5 for more details on small-body dynamics and evolution.

1.4 Physical Properties of Comets

Comets have two phases: inactive and active. A comet is inactive when it is far from the Sun (usually $a \gtrsim 3$ AU), and does not form a coma or tail. A comet may also become extinct (i.e., not able to form a coma or tail), break up, or get ejected from the Solar System (see section 1.6). When a comet is active, it has five main components: the central nucleus, the coma, the hydrogen envelope or cloud, the dust tail, and the plasma or ion tail (Figure 1.2).

1.4.1 Nucleus

The nucleus, about $1 - 15$ km in radius, is the source of all cometary activity. It consists of a mixture of volatile ices and silicate dust particles (see below). This is known as the icy conglomerate, or dirty snowball, model (Whipple, 1950a,b). The composition of cometary nuclei, and if it is different from comet to comet, has been difficult to determine. In fact, only six cometary nuclei have been studied in situ: Giacobini-Zinner in 1985 (Brandt et al., 1984), Halley in 1986 (Reinhard & Battrick,
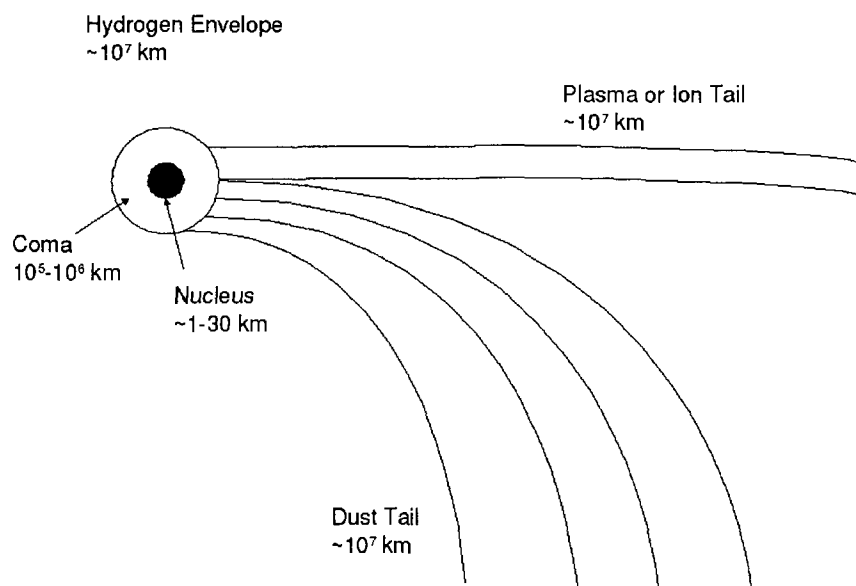
Figure 1.2: A schematic drawing of a comet, showing the nucleus, coma, hydrogen envelope, and tails. Adapted from Figure 10.1c in de Pater & Lissauer (2005).

1986), Grigg-Skjellerup in 1992 (Patzold et al., 1993), Borrelly in 2001 (Boice et al., 2002), Wild 2 in 2004 (Tsou et al., 2004), and Tempel 1 in 2005 (A'Hearn et al., 2005). In astronomical images, inactive or extinct cometary nuclei look similar to asteroids; however, there are some physical distinctions, which are listed in Table 1.1.

The particles which sublimate (i.e., phase change directly from solid to gas form) directly from the nucleus due to solar heating are known as parent molecules. Their existence is derived from observations of the daughter molecules [products of photodissociation (absorption of photons leads to a break-up of a molecule) of parent molecules] in the coma. The principal ice in comets is water ice, since the majority of gases observed are water and its dissociation (a general process in which compounds separate or split into smaller constituents) products, H and OH (Brandt & Chapman, 2004). Other molecules inferred to be present on the nucleus are CO, CO_2,

Table 1.1: Typical physical characteristics of cometary nuclei compared with asteroids.

Characteristic	Comets[a]	Asteroids[b]
Rotation Period (hours)	$5 - 70$	$\gtrsim 2$
Density (g cm^{-3})	$\gtrsim 0.6$	$1.2 - 3.5$
Albedo[c]	$0.02 - 0.06$	$0.05 - 0.50$
Radii (km)	$1 - 15$	$\lesssim 500$
Color	grey-red	red

[a]Information from Lamy et al. (2004).

[b]Information from Bottke et al. (2002) and references therein.

[c]i.e., what percentage of incident sunlight is reflected.

CHO-bearing molecules (i.e., formaldehyde - H_2CO), symmetric hydrocarbons (i.e., methane - CH_4), sulfur-bearing molecules (i.e., hydrogen sulfide - H_2S), nitrogen-bearing molecules (i.e., ammonia - NH_3), and noble gases. For an extensive review of the composition of cometary nuclei, as derived from observations of cometary comae, see Bockelée-Morvan et al. (2004) and references therein.

1.4.2 Coma and Hydrogen Envelope

When a comet approaches the Sun, solar heating causes the release of gas and dust from the nucleus by sublimation which forms the coma. Comae are more-or-less spherical in shape and centered on the nucleus. They range up to 10^{5-6} km in diameter and typically reach a maximum size when the comet is $1.5 - 2.0$ AU from the Sun (Brandt & Chapman, 2004).

The coma is composed of ions, neutral molecules, and dust particles. These may be the daughter products of the parent molecules that originate on the comet nucleus. The gas is assumed to flow away from the nucleus at a constant rate of about 1 km s^{-1} (i.e., A'Hearn et al., 1995). Most of the information known about the composition

of comets is from spectroscopic observations of the gas and dust in the coma. See section 1.7 for more details of spectroscopic observations of the coma, and what information can be derived from such observations.

The hydrogen envelope extends out to 10^7 km from the nucleus. The hydrogen atoms in the envelope arise from the photodissociation of H_2O and OH. The distance the hydrogen particles travel before being photoionized (an incident photon ejects one or more electron from a molecule, atom, or ion) determines the size of the envelope (Fernández, 2005).

1.4.3   Dust and Ion Tails

Dust tails can reach lengths of 10^7 km and are usually curved, broad, featureless, slowly changing, and yellow in colour (Brandt & Chapman, 2004). They are formed when gases sublimate off the nucleus, bringing dust along with them. Dust particles can have speeds ranging from $1 - 1000$ m s^{-1}, depending on their size (i.e., larger particles are more difficult to lift off the nucleus). At distances of tens of nuclear radii, the dust decouples from the gas and is subjected to radiation pressure from the Sun. This pressure blows submicrometer-sized particles outward from the Sun. Particles become spatially separated in the dust tail depending on their size, velocity, and release time, causing the tail to appear curved. Dust tails always point away from the Sun, although during particular observational geometries the tail will appear to point toward the Sun. This phenomenon is known as an anti-tail, and is formed by large particles that do not receive the large acceleration that send the smaller particles into the dust tail (Brandt, 2007).

Plasma or ion tails are straight, have fine structure, are blue in color, point in the anti-solar direction, and change on time scales of minutes to hours. They can reach, and even exceed, lengths of 10^7 km and have diameters of about 10^5 km (de Pater & Lissauer, 2005). They get their name from the fact that they are composed of ionized molecules (from the photoionization of parent molecules in the coma), and are blue in color due to an abundance of CO^+ (Brandt, 2007). The ions interact with the solar magnetic field and form the tail. Speeds of the ions are on the order of 10 km s^{-1} near the nucleus and accelerate to $\lesssim 100$ km s^{-1} far from the head (Brandt & Chapman, 2004).

The gas coma and ion tail are visible to various telescopes because the molecules, atoms, and ions emit radiation at wavelengths from UV to radio. The dust coma and tail are visible to the eye because the small dust particles scatter solar light (Jewitt, Morbidelli & Rauer, 2008). This light allows for the spectroscopic study of comets (discussed in section 1.7, and Chapters 2 and 3). For an extensive overview of the nucleus, coma, hydrogen envelope and tails, see parts IV through VI in Festou, Keller & Weaver (2004), Fernández (2005), Brandt (2007), and references therein.

1.5 Small-Body Dynamics

1.5.1 Orbits

The most basic problem in orbital dynamics is the two body problem, which considers the gravitational interaction between two bodies orbiting about their center of mass. In the absence of nongravitational effects and planetary perturbations (see following
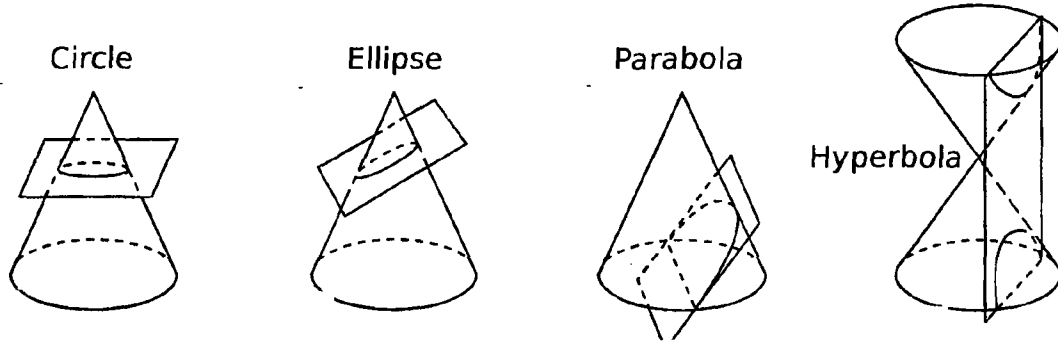
Figure 1.3: A schematic drawing of the conic sections.

section), a small-body will orbit the Sun on a path that is a conic section with the Sun at one focus (Figure 1.3). If the sum of the kinetic and gravitational potential energy is negative, the small-body is bound to the Sun and will travel in an ellipse (eccentricity, is $0 \leq e < 1$). If the total energy is positive, the small-body will move in a hyperbola ($e > 1$). If the energy is exactly zero, the orbit is a parabola ($e = 1$).

The closest and furthest distance to the Sun, perihelion (q) and aphelion (Q), respectively, are given by

$$q = a(1 - e) \quad \text{and} \quad Q = a(1 + e), \quad (1.2)$$

where a is the semi-major axis. The general solution to the two-body problem is characterized by six orbital elements. These parameters specify the size, shape, and orientation of the orbit, as well as the location of the body along the orbit (Figure 1.4):

1. q, the perihelion (distance of closest approach to the Sun),

2. e, the eccentricity,

3. T, the time of perihelion passage,

4. i, the inclination of the orbit with respect to the plane of the ecliptic,
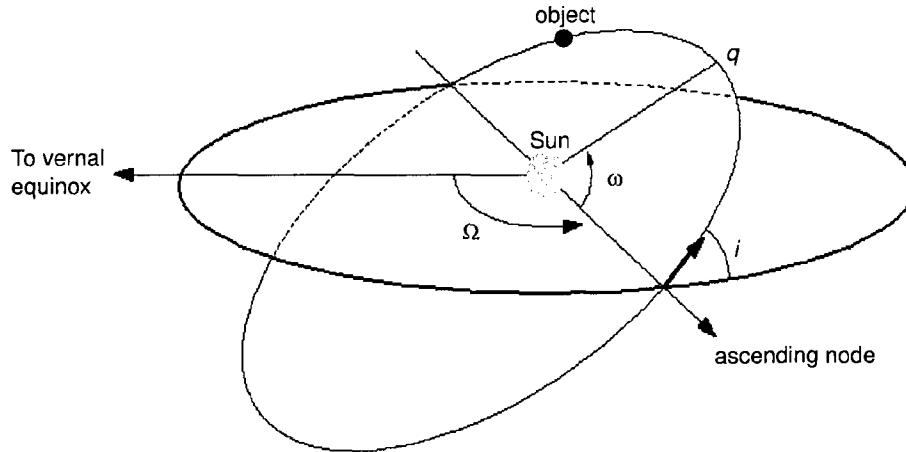
Figure 1.4: A schematic drawing of the orbital elements for the two-body problem.

5. Ω, the longitude of the ascending node (measured East from the vernal equinox),

6. ω, the argument of perihelion (angular distance of perihelion from the ascending node).

The two-body solution works well for an object orbiting about the Sun, with little interaction with other bodies. However, many of the small-bodies (asteroids and comets) also interact with the planets, and a three-body problem is needed to consider the gravitational interaction between three objects. If it is assumed that the third body has negligible mass compared with the other two, and the two larger bodies revolve about each other in circular co-planar orbits, the problem is called the restricted circular three-body problem. This is a good approximation for small-bodies in the Solar System, because the Sun and Jupiter make up the majority of the mass (i.e., the gravitational perturbations from the other planets are much smaller).

The Tisserand parameter is an approximation of the Jacobi constant, which is an invariant of the dynamics of a small-body within the restricted circular three-body

problem. The Jupiter Tisserand parameter, a constant of motion, is given by

$$T_J = \frac{a_J}{a} + 2\cos i \sqrt{\frac{a}{a_J}(1 - e^2)}, \tag{1.3}$$

(Tisserand, 1896; Levison, 1996) where a_J is the semi-major axis of Jupiter, and a, e, and i are the semi-major axis, eccentricity, and inclination of the small-body, respectively. Objects with $T_J < 2$ have weak interactions with Jupiter, while those with $2 < T_J < 3$ have strong interactions (see following section). It should be noted that as i approaches 90°, T_J reduces to a_J/a, and the classification scheme can be misleading in these cases.

The Tisserand parameter is also a measure of the relative velocity between the small-body and Jupiter during a close encounter:

$$U = \sqrt{3 - T_J}, \tag{1.4}$$

where U is the relative velocity between the small-body and Jupiter (expressed in units of the planet's orbital velocity). Objects with low velocities relative to Jupiter suffer stronger encounters. This parameter is well preserved as the orbit of an object changes over its life time. For a complete review of Solar System dynamics, see Murray & Dermott (2005).

1.5.2 Dynamical Classes of Comets

By the mid-nineteenth century, it was understood that comets had orbits larger than those of the planets (Lardner, 1853). At this time, comets were divided into two general populations: those with orbital periods of less than 200 years (short-period comets, SPCs) and those with periods greater than 200 years (long-period comets,

LPCs). This division was arbitrary, but was used in order to determine whether a newly discovered comet had been observed before (since, at the time, orbit determinations had only been reliable for about 200 years). The SPCs were further divided into Jupiter family comets (JFCs - periods less than 20 years), and Halley type comets (HTCs - periods between 20 and 200 years). However, grouping comets by orbital period caused issues: the orbits of comets change over time and, because of this, a comet can jump between classes over its lifetime (see section 1.5.4).

One modern classification scheme is to distinguish comets using the Jupiter Tisserand parameter (Equation 1.3). Comets with $T_J < 2$ have weak interactions with Jupiter and are referred to as nearly isotropic comets (NICs), and include HTCs and LPCs. JFCs have $2 < T_J < 3$ (strong interactions with Jupiter) and are part of the ecliptic comet (EC) class. The ECs also include Encke-type comets ($a < a_J$, $T_J > 3$) and Centaurs ($a > a_J$, $T_J > 3$), which cannot cross the orbit of Jupiter. Figure 1.5 shows this classification scheme. The differences in inclination, orbital period, and T_J between the three major classes implies that they are from different source regions.

This is indeed the case, and there are two main reservoirs of comets: the Kuiper belt and the Oort cloud. The Kuiper belt is a relatively low-inclination population that extends from $30 - 50$ AU (Edgeworth, 1943; Kuiper, 1951), whereas the Oort cloud is an isotropic cloud of icy bodies that extends from 5,000 AU to as far as 100,000 AU (Oort, 1950). JFCs are generally thought to originate in the classical Kuiper belt (Ducan, Levison & Dones, 2004), which initially formed outside the orbit of Neptune. The LPCs, with their wide range of inclinations, are believed to originate in the Oort cloud (Dones et al., 2004).
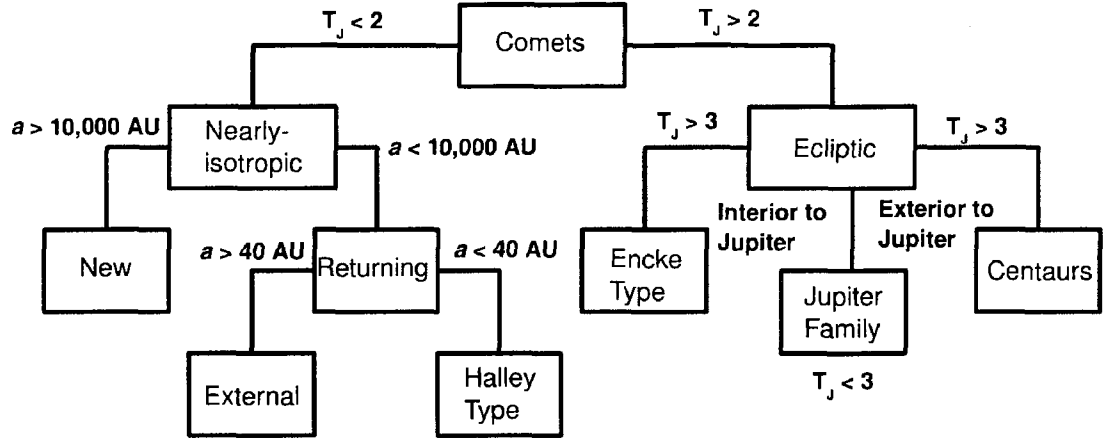
Figure 1.5: A flow chart showing the cometary classification scheme (adapted from Figure 4 in Levison & Dones, 2007).

The HTCs hold intermediate properties: their inclinations are widely distributed, but not isotropic, and their orbital periods are short. Levison & Duncan (1997) determined the classical Kuiper belt could not be a source region for these objects. Instead, they may originate in the scattered disk, which is an extension of the Kuiper belt out to ~ 1000 AU but has a higher inclination distribution (Duncan & Levison, 1997). They could also be from a slightly flattened inner Oort cloud ($a \lesssim 20,000$ AU; Levison, Dones & Duncan, 2001).

Two different lifetimes of a comet are discussed throughout this thesis: dynamical and physical. The dynamical age of a comet (or any small-body) is the lifetime of the object against gravitational perturbations that substantially modify its orbit (i.e., it is ejected from the Solar System or impacts the Sun or a planet). The physical age of a comet is how long it is able to create a coma and tail.
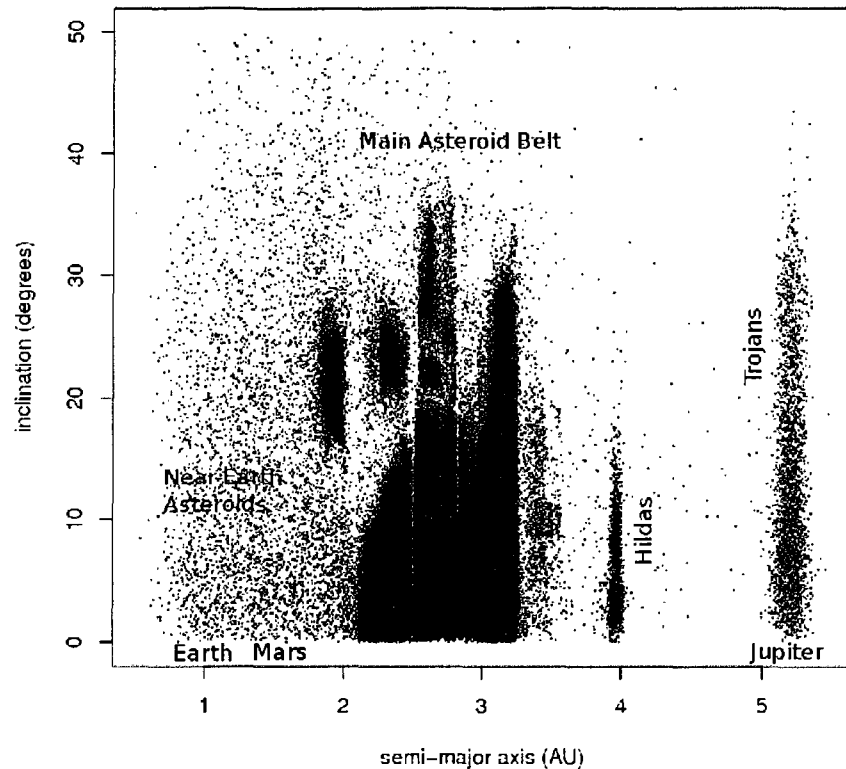
Figure 1.6: Plot of orbital inclination as a function of semi-major axis for asteroids within 5.5 AU from the Sun; orbital elements were found using the Jet Propulsion Laboratory (JPL) small-body search engine: http://ssd.jpl.nasa.gov/sbdb_query.cgi.

1.5.3 Dynamical Classes of Asteroids

The largest reservoir for asteroids in the inner Solar System is the main asteroid belt, situated between the orbits of Mars and Jupiter (1.8 − 4.0 AU from the Sun). Figure 1.6 shows a plot of inclination versus semi-major axis for all of the asteroids with $a < 5.5$ AU. There appears to be a sharp inner boundary at about 2.2 AU. There is also a sharp gap at 3.28 AU. Asteroids at this distance would have exactly half the orbital period of Jupiter, and are said to be in a 2:1 mean-motion resonance with the giant planet. There are other gaps (3:1, 5:2, etc.), and these are known as the Kirkwood gaps (Kirkwood, 1890). The gaps are not physically visible in the asteroid belt, because the asteroids have a wide range of eccentricities.

Beyond 3.5 AU, there are two clusters of asteroids: the Hildas at 3.97 AU (corresponding to the 3:2 mean-motion resonance with Jupiter), and the Trojans at 5.2 AU (located along Jupiter's orbit). The Trojan asteroids reside in dynamically stable zones located 60° ahead and behind Jupiter (known as Lagrangian points, of which there are five; Lagrange, 1772). Almost 2,000 Trojan asteroids have been discovered, and there are almost twice as many objects in the region ahead of Jupiter as there are in the region behind it (Britt, Colsolmagno & Lebofsky, 2007).

Another major group of small-bodies is the Centaurs. These have orbits between Jupiter and Neptune (5.5 − 30 AU). Intially, this group referred to any inactive (i.e., noncometary) small-body beyond Jupiter whose orbit crosses the orbit of a major planet. However, Chiron, the first object discovered in this class, has been observed to have an intermittent coma (Bus et al., 1991). These objects are most likely icy bodies that are perturbed inward from the scattered disk or Kuiper belt (see following section); however, because they reside at vast distances from the Sun, they usually do not warm sufficiently to allow the sublimation of ices.

In the inner Solar System, there are three groups of asteroids that cross the orbits of the inner planets: Amor, Aten, and Apollo asteroids (Figure 1.7). Amor asteroids come in from the asteroid belt and cross the orbit of Mars, but do not cross the Earth's orbit. Aten asteroids have semi-major axes interior to Earth's orbit, but they cross the orbit of Earth. Apollo asteroids have semi-major axes greater than 1 AU, and also cross the orbit of Earth. These three groups make up the near-Earth object (NEO) population, and are perturbed into the inner Solar System by a variety of nongravitational mechanisms (not discussed in this thesis; see Yeomans et al., 2004;
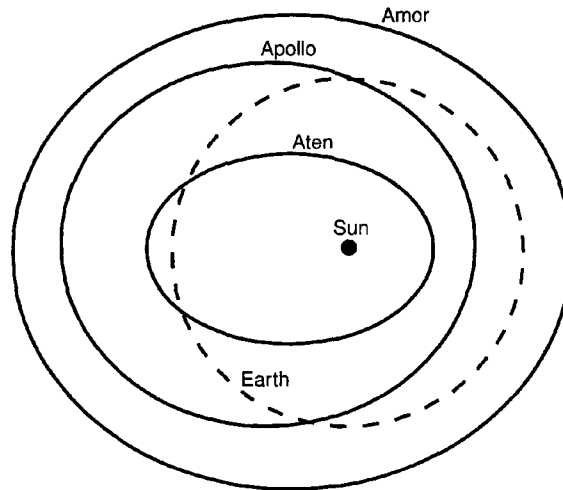
Figure 1.7: Schematic representation of the orbits of Amor, Aten, and Apollo asteroids (solid lines) with respect to the orbit of Earth (dotted line).

Morbidelli et al., 2002, and references therein).

1.5.4   Orbital Evolution of Comets

SPCs (JFCs and HTCs), with low inclinations and typically prograde orbits (orbital motion is in the same direction as the planets), most likely originate in the Kuiper belt or scattered disk. To evolve from this region, an object has to pass from a Neptune-dominated region to a Jupiter-dominated one. The object is transferred from one to the other, being gravitationally dominated by only one planet at a given time. At each transfer, the perihelion is converted to aphelion, and the object is taken away from the outer planet (Horner et al., 2003). The Tisserand parameter (discussed above) is conserved, so the inclination cannot grow to large values. Therefore, the final inclination distribution of the JFCs and HTCs is similar to that of the Kuiper belt and scattered disk. For more details, see Levison & Duncan (1997), Ducan, Levison & Dones (2004), and references therein.

Oort (1950) noted the presence of many new comets (i.e., comets passing near the Sun and sublimating gases for the first time) with $a > 10^4$ AU and a wide range of inclinations. This is evidence that the LPCs originate in a distant region beyond Neptune that must have a spherical shape: the Oort cloud. The LPCs with $a < 10^4$ AU are returning comets that have had their orbits perturbed by the outer planets. At the large distances from the Sun, the evolution of Oort cloud objects is governed by the galactic tide (the gravitational field resulting from the mass distribution of the galaxy), and by passing stars and giant molecular clouds. These interactions may change the object's eccentricity, the perihelion distance may decrease, and it may become a planet-crosser. It then enters the inner Solar System as a new comet. Subsequent gravitational perturbations from the planets decrease the semi-major axis of the comet, or eject it from the Solar System completely. See A'Hearn (2004), Dones et al. (2004) and references therein for additional details.

1.6 Transition Objects

Physical lifetimes of LPCs have been derived to be $\sim 10^4$ years (Levison & Duncan, 1997). Therefore, the comets observed today must be relatively new, and the population must be continually replenished from the Oort cloud (Jewitt, 2004). This leads to the question: what happens to these old comets? Oort (1950) suggested that comets from the Oort cloud will "fade" (will no longer be visible) after a few perihelion passages by either disintegrating or becoming inactive. Wiegert & Tremaine (1999) confirmed this result through modeling, and reported only 10% of comets sur-

vive more than 50 passages, while only 1% survive more than 2,000 passages. This is very different than the JFC population, which have physical lifetimes of $\sim 10^5$ years and remain active for about 1,000 revolutions.

A number of possible mechanisms could cause this fading: the comet could form a crust or be depleted of volatiles, both of which would prevent sublimation (Weissman, Bottke & Levison, 2002); it could disrupt due to any number of processes (rotation, tidal disruption, internal gas pressure, thermal heating, impacts; Binzel et al., 2004); or it could be ejected from the Solar System, as discussed above (Levison & Duncan, 1997).

The first two processes, which prevent sublimation, are known as devolatilization. In this case, a comet is classified as extinct. This is different from an inactive comet, where a comet is in a part of its orbit where it is not sublimating volatiles. Comets become extinct when they can no longer form a coma at any point in their orbit. Extinct comets may look like asteroids, but are decidedly different: they had volatiles on the surface and were able to form a coma at some point, whereas asteroids have minimal volatiles and never show a coma.

Asteroids and comets also differ dynamically, and the standard criterion used to differentiate between a cometary or asteroidal orbit is the Tisserand parameter with respect to Jupiter (T_J; Equation 1.3). Comets typically have $T_J < 3$, while asteroids have $T_J > 3$. However, there are exceptions, such as comet 2P/Encke, which has $T_J = 3.03$ (Jewitt, 2004). Another example is the group of almost 400 NEOs which have $T_J < 3$ [1]. The orbits of these NEOs are very similar to those of JFCs (Jewitt,

---

[1]Found using the JPL small-body search engine: http://ssd.jpl.nasa.gov/sbdb_query.cgi.

Table 1.2: Orbital parameters of the four known MBCs.[a]

Object	a (AU)	e	i (^{o})	T_J
133P/Elst-Pizarro	3.156	0.165	1.4	3.184
P/2005 U1 (Read)	3.165	0.253	1.3	3.153
176P/LINEAR	3.196	0.192	0.2	3.166
P/2008 R1	2.726	0.342	15.9	3.216

[a]Values from Jewitt, Yang & Haghighipour (2009); a is the semi-major axis, e is the eccentricity, i is the inclination, and T_J is the Jupiter Tisserand parameter (given by Equation 1.3)

Morbidelli & Rauer, 2008). Spectroscopic observations by Binzel et al. (2004) indicate the albedos (a measure of the ability of an object to reflect sunlight) of the NEOs with $T_J < 3$ is very different from those with $T_J > 3$. The former have darker albedos, which is common of cometary nuclei (Table 1.1), giving evidence that many JFCs may become extinct and appear as asteroids.

Objects that display cometary activity but are in asteroid-like orbits are known as transition objects (TOs), main-belt comets (MBCs), or activated asteroids (AAs) (Hsieh & Jewitt, 2006a). The origin of these TOs is unknown: did they have cometary orbits but somehow evolved to the asteroid belt, or did they form there in situ? They may be comets that are extinct (TOs or MBCs), or they may be asteroids with higher volatile content (AAs).

Hsieh & Jewitt (2005, 2006b) carried out the first survey to search for MBCs and, so far, only four MBCs have been found: 133P/Elst-Pizzaro (Elst et al., 1996), P/2005 U1 (Read et al., 2005), 176P/LINEAR (Hsieh & Jewitt, 2006a), and P/2008 R1 (Jewitt, Yang & Haghighipour, 2009). Table 1.2 lists the orbital parameters of these objects. This thesis describes two observational techniques to search for TOs and

MBCs: spectroscopy (described in section 1.7 and Chapter 2) and imaging (described in Chapter 4).

1.7 Spectroscopy

A schematic drawing of a typical spectrograph is shown in Figure 1.8. It consists of an entrance slit at the focus of the telescope, a collimator, a prism or grating to disperse the light, and a camera that focuses the light on to a detector. Spectrographs sample the emitted energy distribution from an astronomical source in wavelength bins. Generally, spectrographs have resolutions (bin sizes) of $20 - 40$ Å or better in order to differentiate spectral features (emission or absorption lines) from the background (continuum). For a more in depth overview of spectrographs and observation methods, see Chapters 3 and 10 in Gray (2005) and Chapter 6 in Howell (2006).

Two common measurements from a spectrum of an astronomical source are the shape of the spectral lines, and the flux level (how many photons are observed) as a function of wavelength. The latter measurement is used in this thesis, and is discussed below, as well as in Chapters 2 and 3.

Spectroscopic observations of the coma are the key to understanding the composition of comets. Giovanni Donati (1828-1873) made the first spectroscopic observations of a comet coma (Tempel), and observed three faint emission lines (later determined to be the Swan band sequence of C_2). Sir William Huggins (1824-1910) also observed a cometary coma spectrum in 1866 and saw a reflected solar continuum in addition to the three emission lines observed by Donati. By 1900, many comet comae had
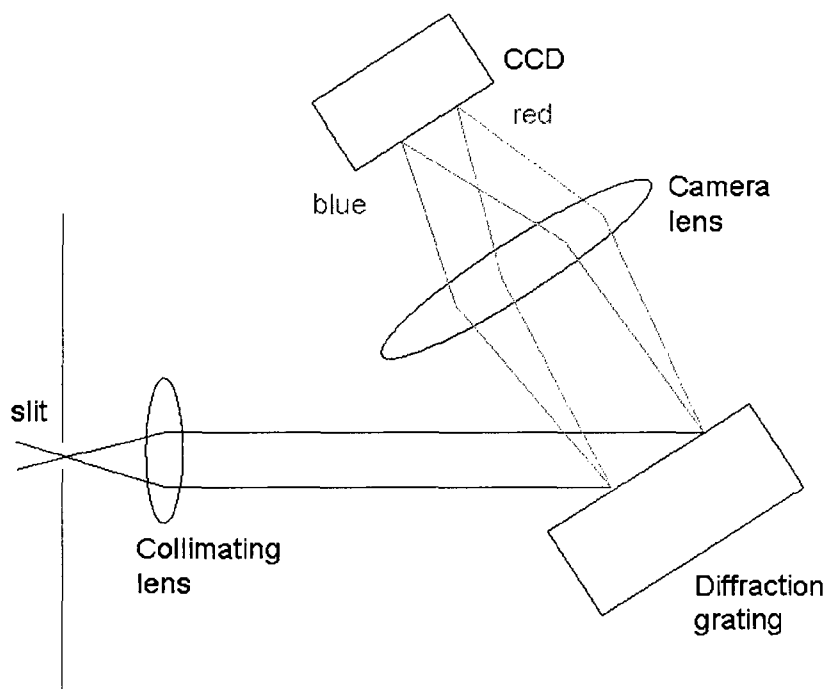
Figure 1.8: A schematic drawing of a typical spectrograph, showing the slit, collimator, prism/grating, camera and detector.

been observed to show a typical spectrum with lines of C_2, CN, C_3, CH, Na, and a continuous reflection spectrum (Brandt & Chapman, 2004). Now more than 50 chemical species in the coma are known (Feldman, Cochran & Combi, 2004).

The sublimation of ices on the nucleus is dictated by the balance between the incident solar radiation on the surface, the reflected radiation, the re-radiated energy, and energy used for internal heating and sublimation of the ices (Jewitt, Morbidelli & Rauer, 2008). The sublimated gases, and the dust that is ejected with them, expand away from the nucleus and form the coma. The parent molecules are subjected to different chemical destruction and excitation processes, and high resolution spectroscopy has shown that the dominant excitation process is resonance fluorescence by solar radiation (i.e., Feldman, Cochran & Combi, 2004).

Resonance fluorescence is when the absorption of a solar photon of a given frequency excites an electron in an atom or molecule, and is followed by spontaneous emission of a photon of the same frequency in a single-step decay process (de Pater & Lissauer, 2005). This causes a transition between the ground state and first excited level and, after a delay, back to the original state of the atom or molecule. The strength of an emission line is derived using the fluorescence efficiency (the luminosity per molecule), or g-factor (erg s^{-1} molecule^{-1}), calculated at a heliocentric distance, r_H, of 1 AU. This factor typically has values on the order of $10^{-12} - 10^{-13}$ erg s^{-1} molecule^{-1}, and is assumed to scale with distance as r_H^{-2} for most molecules (i.e., A'Hearn et al., 1995). However, the g-factor for the CN molecule (of particular interest in this thesis) deviates from this dependence due to the Swings effect: due to the heliocentric velocity of the comet, the solar spectrum is Doppler shifted in the frame of reference of the comet (i.e., Tatum, 1984).

There are other excitation mechanisms occurring in the coma such as collisional excitation (of neutrals, ions or electons) and dissociation (radiative and collisional) of parent molecules (Rodgers et al., 2004). In general, it is assumed resonance fluorescence is the dominant excitation mechanism, and models can be used to deduce the abundances of the parent molecules from the derived abundances of the observed daughter species. Therefore, the additional excitation mechanisms are outside the scope of this thesis and will not be reviewed here. For more information, see Feldman, Cochran & Combi (2004), Chapter 10 of de Pater & Lissauer (2005), Chapter 3 of Jewitt, Morbidelli & Rauer (2008), and references therein.

The strength (size) of an emission line can be used to derive the observed flux by

counting the number of photons in the emission line (see Chapters 2 and 3 for more details). If an emission line is caused solely by resonance fluorescence, the conversion from observed flux of the line to column density, N_c, of the molecule that produces that line is given by

$$N_c = \frac{4\pi F}{g\Omega},$$ (1.5)

(see Appendix A for derivation) where F is the observed flux in the telescope aperture (erg cm^{-2} s^{-1}), Ω is the solid angle of the aperture (sr), and g is the g-factor defined above (erg s^{-1} molecule^{-1}).

To convert column density to a gas production rate by the nucleus, various simple models can be implemented. These models do not take into account parameters such as velocities, temperatures, or other physical and chemical processes, since they are difficult to measure, particularly at large distances from the Sun (Jewitt, Morbidelli & Rauer, 2008).

If the whole coma can be observed in the field of view (FOV) and resonance fluorescence is assumed to be the main excitation mechanism, the gas production rate of the nucleus is given by

$$Q = \frac{4\pi\Delta^2 F}{g\tau},$$ (1.6)

where Δ is the geocentric distance (cm), and τ is the lifetime against photodissociation of the molecule (s). The production rate, Q, is in units of molecules s^{-1}.

Since comet comae are so large, spectroscopic observations do not cover the whole coma in the FOV, so a model needs to be applied in order to correct for the molecules that are not directly observed. For this thesis, it is assumed resonance fluorescence

is the main excitation mechanism, the molecules travel the total distance of their scale length before photo-destruction, and the coma is spherically symmetric. The production rate in this scenario is given by

$$Q = \frac{16\pi\Delta v_e F}{3g\theta},$$ (1.7)

where v_e is the velocity of the observed molecule (cm s^{-1}) and θ is the slit width (radians). See Appendix A for derivation.

Another model that is commonly used is the Haser model (Haser, 1957). Instead of assuming the molecules travel the distance of their scale length before photodissociation, it is assumed there is an exponential decay. In the case where the scale length of the daughter molecule is longer than that of the parent (valid for this thesis), the production rate of the observed molecule is

$$Q = \frac{4\pi\Delta^2 v_e F}{gX}$$ (1.8)

where X is a constant of integration that must be solved numerically (see Appendix A for derivation).

There are other, more realistic, models of the coma (for example, Festou, 1981; Combi & Smyth, 1988; Combi, Harris & Smyth, 2004) that take into account temporal variations of Q due to non-isotropic outgassing, rotation, orbital variations, outbursts, and additional chemical processes. These models are not widely used since they require more accurate values of the outflow velocities, scale lengths, and energies from the chemical processes. Therefore, until better observations of cometary comae are achieved, simple models are best to derive production rates easily for a large number of comets.
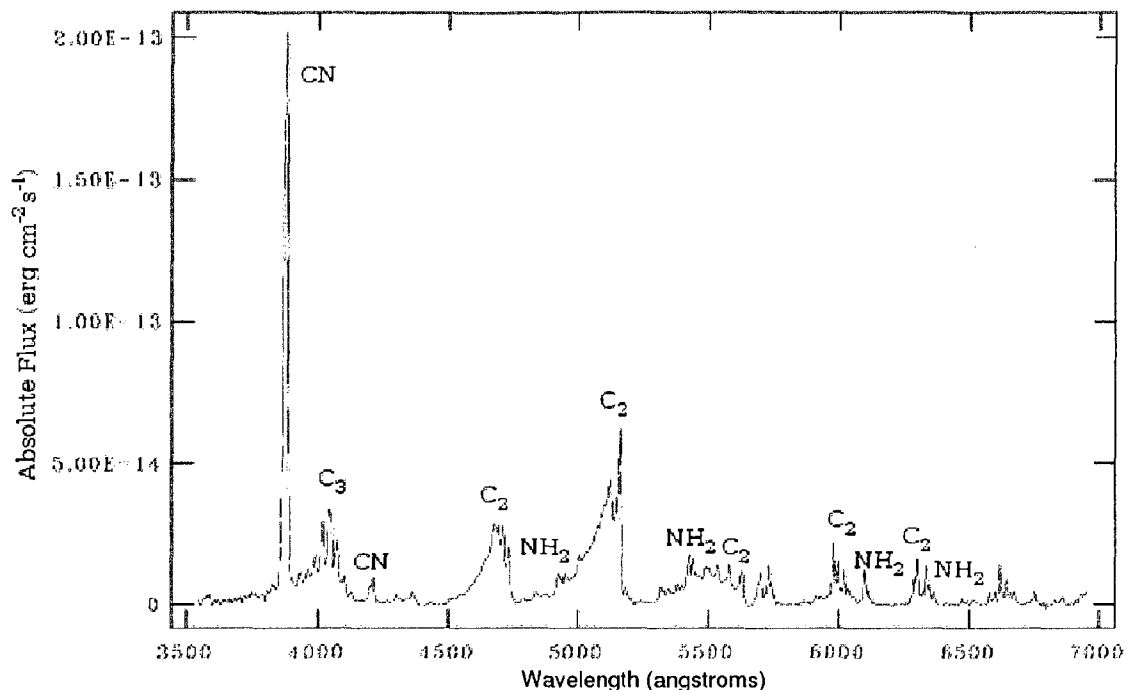
Figure 1.9: An example spectrum of comet 2006 VZ13, obtained 2007 August 13 using the CTIO (see Chapter 3). Major emission lines are labelled.

In this thesis, the production rates for CN (3880 Å), C_2 (4740 and 5160 Å), and C_3 (4056 Å) molecules are derived for a variety of comets (see Chapters 2 and 3). The CN line at 3880 Å is of particular interest because of its strength out to large distances from the Sun and the lack of other lines close by (Feldman, Cochran & Combi, 2004). To illustrate this, Figure 1.9 shows an example of a cometary spectrum acquired of new Oort cloud comet 2006 VZ13 with the Cerro-Tololo Inter-American Observatory (CTIO) 1.5-m telescope (Chapter 3).

Production rate ratios give insight to the composition of the cometary nucleus. The most volatile molecule of the nucleus is water, and abundance ratios are typically calculated as a function of its production rate. However, abundance ratios are also often quoted with respect to CN, for the reasons stated above. For typical production

rate ratios with respect to water, see Bockelée-Morvan et al. (2004), for example.

One of the largest surveys on cometary activity was completed by A'Hearn et al. (1995), where 85 different comets were observed over a period of 16 years. They reported little variation of relative production rates with heliocentric distance or apparition (i.e., how many times a comet has orbited the Sun). Their findings also indicated two major classes of comets: those that are carbon-depleted and those that are not (known as "typical"). Comets that have $\log(Q(C_2)/Q(CN)) < -0.18$ (where $Q(X)$ is the gas production rate of that species) are considered carbon-depleted, while typical comets have values greater than this (criteria set by A'Hearn et al., 1995). This is discussed more in Chapter 3 of this thesis.

A production rate for the dust can also be derived. However, to be able to derive this directly from observations, the particle size distribution, their density, mass, optical properties, and dynamics need to be determined (Jewitt, Morbidelli & Rauer, 2008). These quantities are difficult to determine observationally, so a less complicated model is usually used.

If the cometary dust is assumed to flow away from the nucleus in a uniform manner, without breakup, acceleration, or darkening, then the quantity $Af\rho$ (cm) is proportional to the dust production rate (A'Hearn et al., 1984). The parameters are as follows: A is the Bond albedo, f is the filling factor of the grains in the FOV, and ρ is the linear radius of the telescope aperture at the comet (cm). Together, the $Af\rho$ parameter is a measure of the effective dust scattering area in the FOV, and is not a direct measure of the dust production rate. However, it is often used as a proxy because of the simplicity of its calculation from measurable and observable

parameters. This is given by

$$Af\rho = \frac{(2\Delta r_H)^2}{\rho}\frac{F_\lambda}{F_\odot} \tag{1.9}$$

where F_λ is the mean cometary flux in a given wavelength range (where there are no emission lines), and $F_\odot$ is the solar flux in the same wavelength range (both in erg cm^{-2} s^{-1} Å^{-1}). The heliocentric and geocentric distances are in AU and cm, respectively. The parameters Δ, r_H, and ρ are geometric quantities, while the cometary flux, F_λ, can be derived using spectroscopic observations. The solar flux, $F_\odot$, at a given wavelength can be found in Arvesen, Griffin & Pearson (1969). The value of $Af\rho$ was derived for many comets in A'Hearn et al. (1995) and they noted a correlation between the dust-to-gas ratio (with respect to OH and CN) and perihelion distance, but not with dynamical age of the comet. Similar results are also reported in Chapter 3 of this thesis.

1.8   Thesis Overview

The topic of this thesis was motivated by two main papers: Chamberlin et al. (1996), who described a spectroscopic study to search for emission lines from three asteroids in comet-like orbits, and Hsieh & Jewitt (2006a), who described photometric observations of three MBCs. The overall theme of this thesis is to search for and study cometary activity on small-bodies in our Solar System. In particular, observations were acquired of active comets of different ages and classes, and two techniques were used to search for transition objects.

Chapter 2 describes a feasibility study of a program to search for transition objects

using spectroscopic observations from the 1.2 m Elginfield telescope near London, Ontario. Similar studies have been completed (such as Chamberlin et al., 1996; Harris et al., 2001; Binzel et al., 2004), but have focused on only a few objects. Therefore, this is the first large spectroscopic search for transition objects. Results are compared to similar observations at the Dominion Astrophysical Observatory near Victoria, British Columbia, and to previous studies.

Chapter 3 describes spectroscopic observations of five active comets using the 1.5 m Cerro-Tololo Inter-American Observatory. Of particular interest were the observations of 2006 VZ13, a new Oort cloud comet passing perihelion for the first time during these observations. Gas and dust production rates and ratios were calculated for each comet, and were compared to results from previous studies. This study has been submitted for publication (Gilbert et al., 2009).

Chapter 4 describes a search for main-belt comets using the Canada-France-Hawaii Telescope Legacy Survey. Approximately 950 objects were carefully analyzed using a three-level technique, and over 11,000 objects were investigated by eye to determine whether they showed evidence of cometary activity. This was the first survey of its size, to use archived images, and to search an unbiased sample of the asteroid belt for main-belt comets. This study has been published (Gilbert & Wiegert, 2009).

Finally, Chapter 5 provides a brief summary of the work presented in this thesis, tying together the three projects, and describes future possibilities for these projects specifically and for cometary observations in general.

References

A'Hearn, M. 2004. Cometary science: The present and future. In Festou, M., Keller, H., Weaver, H. (Eds), Comets II. Tuscon: The University of Arizona Press, 17-24.

A'Hearn M., Schleicher D., Feldman P., Millis R., Thompson D. 1984. Comet Bowell 1980b. AJ 89, 579-591.

A'Hearn M., Millis R., Schleicher D., Osip, D., Birch, P., 1995. The ensemble properties of comets: Results from narrowband photometry of 85 comets. 1976-1992, Icarus 118, 223-270.

A'Hearn, M. and 32 collaborators, 2005. Deep Impact: Excavating comet Tempel 1. Science 310, 258-264.

Alfvén, H. 1963. On the early history of the Sun and the formation of the Solar System. ApJ 137, 981-990.

Arvesen J., Griffin R., Pearson B. Jr., 1969. Determination of extraterrestrial solar spectral irradiance from a research aircraft, Appl. Op. 8, 2215-2232.

Biermann, L. 1951. Kometenschweife und Korpuskularstrahlung. ZA 29, 274-286.

Binzel, R., Rivkin, A., Stuart, S., Harris, A., Bus, S., Burbine, T. 2004. Observed spectral properties of near-Earth objects: results for population distribution, source regions, and space weathering processes. Icarus 170, 259-294.

Bockelée-Morvan, D., Crovisier, J., Mumma, M., Weaver, H. 2004. The composition of cometary volatiles. In Festou, M., Keller, H., Weaver, H. (Eds), Comets II. Tuscon: The University of Arizona Press, 391-423.

Boehnhardt, H. 2004. Split comets. In Festou, M., Keller, H., Weaver, H. (Eds), Comets II. Tuscon: The University of Arizona Press, 301-316.

Boice, D. and 11 collaborators, 2002. The Deep Space 1 encounter with comet 19P/Borrelly. EMP 89, 301-324.

Bottke Jr., W., Cellino, A., Paolicchi, P., Binzel, R. 2002. Asteroids III. Tuscan: University of Arizona Press.

Brandt, J. 2007. Physics and chemistry of comets. In McFadden, L.-A., Weissman, P., Johnson, T. (Eds), Encyclopedia of the Solar System. Oxford: Elsevier. 557-574.

Brandt, J., Chapman, R. 2004. Introduction to comets. Cambridge: Cambridge University Press.

Brandt, J., Farquhar, R., Niedner, M., von Rosenvinge, T. 1984. The intercept of comet Giacobini-Zinner (G/Z) by the International Cometary Explorer (ICE). PASP 96, 784-785.

Britt, D., Colsolmagno, G., Lebofsky, L. 2007. Main-belt asteroids. In McFadden, L.-A., Weissman, P., Johnson, T. (Eds), Encyclopedia of the Solar System. Oxford: Elsevier. 349-364.

Bus S., A'Hearn M., Schleicher D., Bowell E., 1991. Detection of CN emission from (2060) Chiron, Science 251, 774-777.

Chamberlin, A., McFadden, L.-A., Schulz, R., Schleicher, D., Bus, S. 1996. 4015 Wilson-Harrington, 2201 Oljato, and 3200 Phaethon: Search for CN emission. Icarus 119, 173-181.

Chambers, J., Halliday, A. 2007. The origin of the Solar System. In McFadden, L.-A., Weissman, P., Johnson, T. (Eds), Encyclopedia of the Solar System. Oxford: Elsevier. 29-52.

Cheng, A. 2004. Collisional evolution of the asteroid belt. Icarus 169, 357-372.

Combi, M., Smyth, W. 1988. Monte Carlo particle-trajectory models for neutral cometary gases. I - Models and equations. II - The spatial morphology of the Lyman-alpha coma. ApJ 327, 1026-1059.

Combi, M., Harris, W., Smyth, W. 2004. Gas dynamics and kinetics in the cometary coma: Theory and observations. In Festou, M., Keller, H., Weaver, H. (Eds), Comets II. Tuscon: The University of Arizona Press, 523-552.

de Pater, I., Lissauer, J. 2005. Planetary sciences. Cambridge: Cambridge University Press.

Dones, L., Weissman, P., Levison, H., Duncan, M. 2004. Oort cloud formation and dynamics. In Festou, M., Keller, H., Weaver, H. (Eds), Comets II. Tuscon: The University of Arizona Press, 153-174.

Duncan, M., Levison, H. 1997. A scattered comet disk and the origin of Jupiter family comets. Science 276, 1670-1672.

Duncan, M., Levison, H., Dones, L. 2004. Dynamical evolution of ecliptic comets. In Festou, M., Keller, H., Weaver, H. (Eds), Comets II. Tuscon: The University of Arizona Press, 193-204.

Edgeworth, K. 1943. The evolution of our planetary system. JBAA 53, 181-188.

Elst, E., Pizarro, O., Pollas, C., Ticha, J., Tichy, M., Moravec, Z., Offutt, W. Marsden, B. 1996. Comet P/1996 N2 (Elst-Pizarro). IAU Circ. 6456, 1.

Feldman P., Cochran A., Combi M., 2003. Spectroscopic investigations of fragment species in the coma. In Festou M., Keller H., Weaver H., eds, Comets II. Tuscon: The University of Arizona Press, 425-448.

Fernández, J. 1980. On the existence of a comet belt beyond Neptune. MNRAS 192, 481-491.

Fernández, J. 2005. Comets: Nature, dynamics, origin, and their cosmogonical relevance. The Netherlands: Springer.

Fernández, J., Gallardo, T., Brunini, A. 2002. Are there many inactive Jupiter-family comets among the near-Earth asteroid population? Icarus 159, 358-368.

Festou, M. 1981. The density distribution of neutral compounds in cometary atmospheres. I - Models and equations. A&A 95, 69-79.

Festou, M., Keller, H., Weaver, H. 2004. Comets II. Tuscon: The University of Arizona Press.

Gilbert, A., Wiegert, P. 2009. Searching for main-belt comets using the Canada-France-Hawaii Telescope Legacy Survey. Icarus 201, 714-718.

Gilbert, A., Wiegert, P., Unda-Sanzana, E., Vaduvescu, O. 2009. Spectroscopic observations of new Oort cloud comet 2006 VZ13 and four other comets. Submitted to MNRAS.

Gray, D. 2006. The observation and analysis of stellar photospheres. New York:

Cambridge University Press.

Harris, A., Delbó, M., Binzel, R., Davies, J., Roberts, J., Tholen, D., Whiteley, R. 2001. Visible to thermal-infrared spectrophotometry of a possible inactive cometary nucleus. Icarus 153, 332-337.

Haser L., 1957. Distribution d'intensite dans la tete d'une comete. Bull. Soc. R. Sci. Liège 43, 740-750.

Hellman, C. 1944. The comet of 1577: Its place in the history of astronomy. New York: AMS Press.

Howell, S. 2006. Handbook of CCD astronomy. New York: Cambridge University Press.

Horner, J., Evans, N., Bailey, M., Asher, D. 2003. The populations of comet-like bodies in the Solar System. MNRAS 343, 1057-1066.

Hsieh, H., Jewitt, D. 2005. Search for active main-belt asteroids: The SAMBA project. BAAS 37, 631 (abstract).

Hsieh, H., Jewitt, D. 2006a. A population of comets in the main asteroid belt. Science 312, 561-563.

Hsieh, H., Jewitt, D. 2006b. Active asteroids: Mystery in the main belt. In Lazzaro, D., Ferraz-Mello, S., Fernández, J. (Eds), Asteroids, Comets, Meteors (IAU S229). Cambridge University Press, Cambridge, UK, 425-437.

Jewitt, D. 2004. From cradle to grave: The rise and demise of the comets. In Festou, M., Keller, H., Weaver, H. (Eds), Comets II. Tuscon: The University of Arizona

Press, 659-676.

Jewitt, D., Morbidelli, A., Rauer, H. 2008. Trans-Neptunian objects and comets. Berlin: Springer.

Jewitt, D., Yang, B., Haghighipour N. 2009. Main-belt comet P/2008 R1 (Garradd). AJ 137, 4313-4321.

Kepler, J. 1596. Mysterium Cosmographicum. Excudebat Georgius Gruppenbachius, Tubingae. Translated by Duncan, A. (1981) The Secrets of the Universe. Abaris, New York.

Kirkwood, D., 1890. On the similarity of certain orbits in the zone of asteroids. PASP 2, 48-49.

Kuiper, G. 1951. On the origin of the solar system. In Hynek, J. (Ed), Astrophysics. New York: McGraw-Hill.

Lagrange, J. 1772. Essai sur le probléme des trois corps. Ouvres, 1783, 3: 229-331.

Lamy, P., Toth, I., Fernández, Y., Weaver, H. 2004. The sizes, shapes, albedos, and colors of cometary nuclei. In Festou, M., Keller, H., Weaver, H. (Eds), Comets II. Tuscon: The University of Arizona Press, 223-264.

Lardner, D. 1853. On the classification of comets and the distribution of their orbits in space. MNRAS 13, 188-192.

Levison, H. 1996. Comet taxonomy. ASP Conf. Ser. 107: Completing the Inventory of the Solar System 107, 173-191.

Levison, H., Dones, L. 2007. Comet populations and cometary dynamics. In Mc-Fadden, L.-A., Weissman, P., Johnson, T. (Eds), Encyclopedia of the Solar System. Oxford: Elsevier. 575-588.

Levison, H., Dones, L., Duncan, M. 2001. The origin of Halley-type comets: Probing the inner Oort cloud. AJ 121, 2253-2267.

Levison, H., Duncan, M. 1997. From the Kuiper belt to Jupiter-family comets: The spatial distribution of ecliptic comets. Icarus 127, 13-32.

McFadden, L.-A., Weissman, P., Johnson, T. (Eds), Encyclopedia of the Solar System. Oxford: Elsevier. 575-588.

Morbidelli, A., Bottke Jr., W., Froeschlé, Ch., Michel, P. 2002. Origin and evolution of near-Earth objects. In Bottke Jr., W., Cellino, A., Paolicchi, P., Binzel, R. (Eds), Asteroids III. Tuscan: University of Arizona Press, 409-422.

Murray, C., Dermott, S. 2005. Solar system dynamics. New York: Cambridge University Press.

Oliver, C., 1930. Comets. Baltimore: Williams & Wilkins.

Oort, J. 1950. The structure of the cloud of comets surrounding the solar system and a hypothesis concerning its origin. BAIN 11, 91-110.

Patzold, M., Edenhofer, P., Bird, M., Volland, H. 1993. The Giotto encounter with Comet P/Grigg-Skjellerup - First results from the Giotto Radio-Science Experiment. A&A 268, L13-L16.

Read, M., Bressi, T., Gehrels, T., Scotti, J., Christensen, E. 2005. Comet P/2005 U1

(Read). IAU Circ. 8624, 1.

Reinhard, R., Battrick, B. 1986. Space missions to Halley's comet. Paris: ESA.

Rodgers, S., Charnley, S., Huebner, W., Boice, D. 2004. Physical processes and chemical reactions in cometary comae. In Festou, M., Keller, H., Weaver, H. (Eds), Comets II. Tuscon: The University of Arizona Press, 505-522.

Sagan, C. and Druyan, A. 1985. Comet. New York: Random House.

Swamy, K. 1986. Physics of comets. Singapore: World Scientific Publishing.

Tatum, J. 1984. Cyanogen radiance/column-density ratio for comets calculated from the Swings effect. AA 135, 183-187.

Tisserand, F. 1896.Traité de Mécanique Céleste IV. Paris: Gauthier-Villars.

Tsou, P. and 19 collaborators, 2004. Stardust encounters comet 81P/Wild 2. JGR 109, E12S01.

Weissman, P., Bottke, W., Levison, H. 2002. Evolution of comets into asteroids. In Bottke Jr., W., Cellino, A., Paolicchi, P., Binzel, R. (Eds), Asteroids III. Tuscan: University of Arizona Press, 669-686.

Whipple, F. 1950a. A comet model. I. The acceleration of comet Encke. ApJ 111, 375-94.

Whipple, F. 1950b. A comet model. II. Physical relations for comets and meteors. ApJ 113, 464-474.

Whipple, F. 1955. A comet model. III. The zodiacal light. ApJ 121, 750-770.

Wiegert, P., Tremaine, S. 1999. The evolution of long period comets. Icarus 137, 84-121.

Yeomans, D., Chodas, P., Sitarski, G., Szutowicz, S., Królikowska, M. 2004. Cometary orbit determination and nongravitational forces. In Festou, M., Keller, H., Weaver, H. (Eds), Comets II. Tuscon: The University of Arizona Press, 137-152.

Zanstra, H., 1929. The excitation of the line- and band-spectra in comets by sunlight. MNRAS 89, 178-97.

Chapter 2

Feasibility of a Program to Search for Transition Objects Using the Elginfield Telescope

*We have reason to suspect that there are a great many more comets,
which being at remote distances from the Sun, and being obscure
and without tail, may for that reason escape our observation.*

- Edmond Halley, *Transactions of the Royal Society of London*, 1706.

2.1 Introduction

The search for and study of transition objects (TOs; objects classified as asteroids, but display comet-like activity) is a relatively new research area in planetary science. TOs are unusual because they are situated in asteroid domains (i.e., main asteroid belt, near-Earth asteroids), but show cometary activity. They may either be comets that

have depleted their volatile ices (main-belt comets, MBCs), or asteroids which contain a small amount of volatiles (activated asteroids, AAs). In both cases, transition objects will usually look asteroidal (point-source) in nature. However, periodically they will "turn on" and display a coma or even a tail, as regular comets do. In this case, imaging techniques can be used to search for such features, particularly near perihelion passage (i.e., Hsieh & Jewitt, 2006; Chapter 4 of this thesis).

Four TOs have been found in the main asteroid belt (MBCs). The first MBC detected was 133P/Elst-Pizzaro in 1996 by Elst et al. (1996). There have been only three other MBCs found: P/2005 U1 (Read et al., 2005), 176P/LINEAR (Hsieh & Jewitt, 2006) and P/2008 R1 (Jewitt, Yang & Haghighipour, 2009). These objects are difficult to find due to their small sizes, low albedos, and only being active for portions of their orbit.

Even if there is sublimation of ices on TOs, gas production may be too low to produce a coma or tail detectable using standard imaging techniques. Cometary material, having strong optical emission lines (including CN, C_2, C_3, etc.), can be identified using spectroscopic observations. The CN line at 3880 Å is of particular interest because of its strength out to large distances from the Sun and the lack of other lines close by (Feldman, Cochran & Combi, 2004). Spectroscopy also has a distinct advantage over imaging when observing faint, diffuse objects (i.e., comae): the light is spread over a large number of pixels in images, while spectra concentrate the light into fewer pixels, increasing the signal-to-noise ratio.

Chamberlin et al. (1996) performed a small survey of three TO candidates and, although they did not observe the CN line, they derived upper limits for the CN gas

production rate. Other studies, such as Harris et al. (2001) (who searched for activity on asteroid 1999 LD31) and Binzel et al. (2004) (who observed spectral properties of over 250 near-Earth objects), focused on spectroscopic observations in the I and R bands, also found no evidence of cometary activity.

The project presented here is meant to study the feasibility of a search program for TOs using the 1.2 m Elginfield telescope, near London, Ontario. A recent study by Hsieh & Jewitt (2006) observed 300 objects over a period of three years, and detected three MBCs: known MBCs 133P and P/2005 U1, and newly discovered 176P. They derived an upper limit of 15 − 150 currently active MBCs. In order to expand and improve on those results, hundreds of objects would need to be observed.

Spectroscopic observations were acquired of 77 different small-bodies over a period of about 1.5 years with the Elginfield telescope. For comparison, similar observations were acquired of 30 objects with the Dominion Astrophysical Observatory (DAO), located near Victoria, British Columbia. Both systems have detectors that are more sensitive in the blue end of the spectrum compared to previous generations. Upper limits for the production rate of CN, and other spectral lines, are calculated and compared to similar studies.

2.2 Observations and Data Reduction

2.2.1 Elginfield

All spectra were obtained using the 1.2 m Elginfield telescope, Santa Barbara Instrument Group (SBIG) ST-7XME CCD camera and SGS spectrograph (Figures 2.1- 2.4).
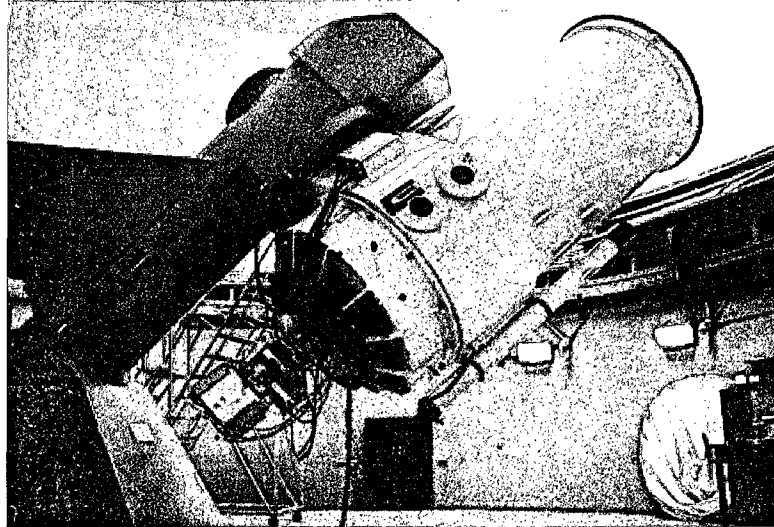
Figure 2.1: Photo of the Elginfield 1.2 m telescope. Courtesy of D. Gray.
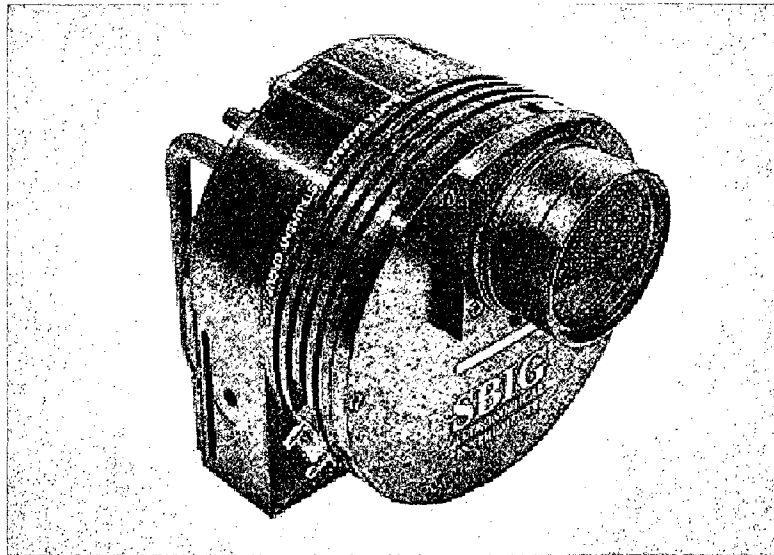
**Figure 2.2:** Photo of the SBIG ST-7XME CCD camera. Courtesy of SBIG.
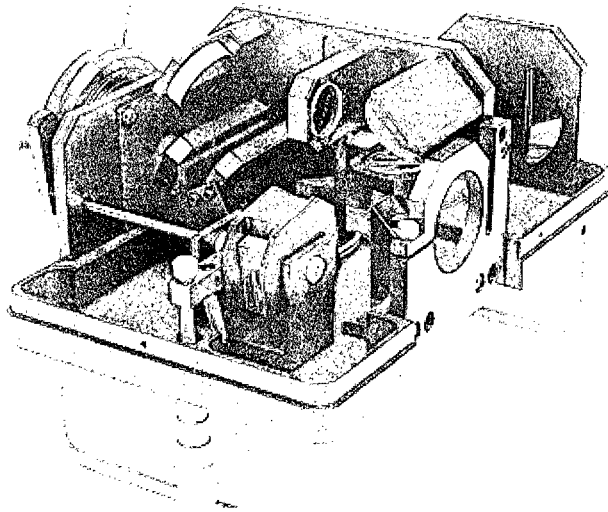
**Figure 2.3:** Photo of the SBIG SGS spectrograph. Courtesy of SBIG.
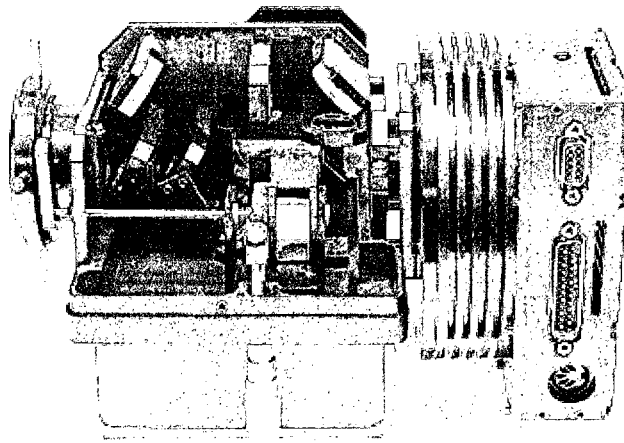
Figure 2.4: Photo of the SBIG ST-7XME CCD camera attached to the SGS spectrograph. Courtesy of SBIG.

The two instruments were chosen because of the relatively high sensitivity in the blue end of the visual spectrum (where the CN line lies) of the CCD, the dual-CCD to allow for auto-guiding, the cooling abilities of the CCD, and their low cost (being off-the-shelf equipment). The CCD and spectrograph were purchased in February 2006. Initial tests were completed using various lamps (mercury, fluorescent and argon) in the lab, and a mounting device was constructed before the instruments were added to the telescope at the Cassegrain focus in April 2006. The instruments and software package (CCDOPS) were very intuitive, and once installed they were ready for use. Two test nights were used in order to become familiarized with the equipment before the project officially began.

The imaging CCD has dimensions of 765×510 pixels, with a pixel size of 9 μm. The spectrograph has two available gratings: 150 lines mm^{-1} (4.3 Å pixel^{-1}) and 600 lines mm^{-1} (1.0 Å pixel^{-1}). Two slit widths are also available: 18 μm and 72 μm. For this study, the lower resolution grating was used with the narrow slit, giving a resolution of 10 Å and a spectral coverage of about 3200 Å. The size of the slit corresponds to a width of 2″ on the sky.

Observations were acquired of 71 asteroids and 6 comets from May 2006 to October 2007 (see Appendix B for a full table of observations). The dark current (arising from thermal noise) was not negligible in these instruments, so dark frames (an exposure with the shutter closed) were obtained after each object spectrum. Comparison lamp (argon or fluorescent) and A-star spectra were recorded each night for wavelength calibration purposes. To correct for solar reflection, a spectrum of a solar-analog star was acquired at the beginning of each night. Separate flat-field exposures were not

obtained. Instead, this correction was made using a portion of the exposure that was not illuminated (i.e., above and below the object spectrum).

2.2.2   Dominion Astrophysical Observatory

To provide a basis for comparison, the 1.8 m DAO telescope and Cassegrain spectrograph were used to acquire spectra of 30 asteroids during 2007 April 15-18 and 2007 August 14-18 (UT) (Figure 2.5). The SITe-2 and SITe-5 CCD detectors were used for the April and August observations, respectively. The SITe-2 CCD is 1852×532 pixels with a pixel size of 15 μm, while the SITe-5 CCD is 1024×1024 pixels with 24-μm pixels. The SITe-5 CCD is more sensitive in the blue end of the spectrum (quantum efficiency of 69% compared to 35% at 4000 Å for the SITe-2 CCD); however, this CCD was not available for use in April 2007.

For the Cassegrain spectrograph, a 300 lines mm^{-1} grating was used, with a dispersion of 60 Å mm^{-1}. This gave a resolution of $\sim$5 Å and a spectral coverage of about 1600 Å. The slit width was set to 71 μm, which corresponds to a width of 1.5" on the sky.

The dark current was negligible with these instruments, so dark frames were not necessary. Comparison lamp (FeAr) and A-star spectra were obtained each night in order to wavelength calibrate the object spectra. To correct for solar reflection, at least one solar-type star was observed each night. As with the Elginfield data, flat fields were not acquired separately, but non-illuminated portions of the object spectra were used for this purpose.
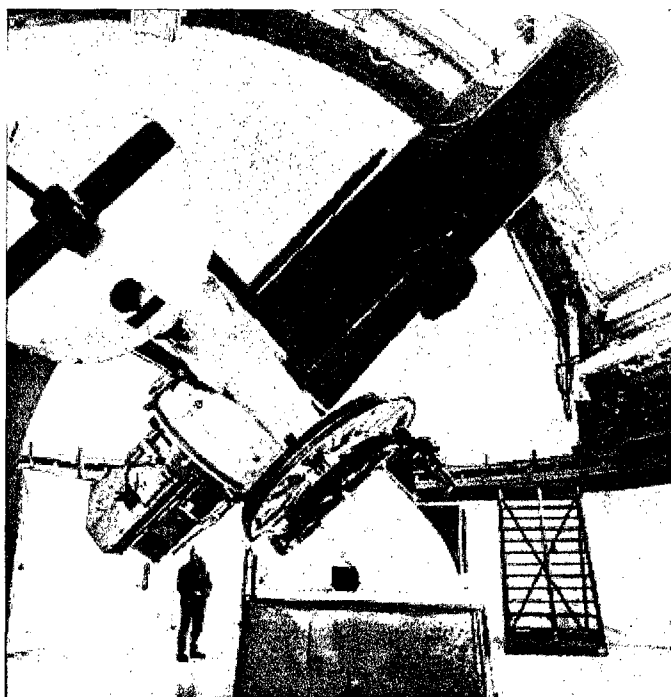
Figure 2.5: Photo of the DAO 1.8 m telescope. Courtesy of D. Balam.

2.3 Data Reduction

Both the Elginfield and DAO data were reduced using the IRAF software package (Tody, 1993). The procedures used for each data set are similar, but with a few minor differences, and are outlined below.

2.3.1 Elginfield

For each object, a dark frame of the same exposure time was subtracted. One-dimensional spectra were then extracted using IRAF's APALL tool, which traced the center of the spectrum and removed cosmic-ray hits. It also subtracted the back-ground sky on either side of the spectrum, which was used as a flat-field correction. Each spectrum was wavelength calibrated using the comparison lamp and/or A-star spectrum. Spectra acquired of the same object on the same night were co-added to

increase the signal-to-noise ratio.

The solar-analog spectrum was used to correct for solar reflection. This was achieved by scaling the stellar spectrum to the same height as the object spectrum and subtracting. This correction was not perfect. To compensate for this difference, the continuum of each object was fit again with a cubic spline function and subtracted.

The object spectra were flux calibrated using observations of the solar-analog star HD 142093 obtained on 2007 July 11. The star was observed several times that night at different airmasses. Using these observations, the effective airmass and system sensitivity were calculated. These were used to calibrate the object spectra obtained with the Elginfield telescope. The final result is a one-dimensional, absolute-flux-calibrated spectrum for each object.

2.3.2 DAO

The one-dimensional extraction, wavelength calibration, solar reflection correction and additional continuum fitting for the DAO data were completed in the same manner described above. The effective airmass and sensitivity function for both CCD detectors were provided by the DAO staff. These were used to flux calibrate the object spectra obtained with the DAO telescope to give one-dimensional, absolute-flux-calibrated spectra.

2.3.3 Challenges

There were some challenges with the data collection and instruments used at the Elginfield observatory. We want to note these in case future observers want to attempt

similar observations. These are all minor issues and do not affect the outcome of the data analysis.

1. A micrometer on the SBIG spectrograph was used to select the central wavelength of the spectra. This was initially set at 5000 Å, which should have a range of $3400 - 6600$ Å according to the documentation. However, when this data was reduced, the spectral range was found to be $4900 - 8100$ Å. The micrometer was reset to 4600 Å so the actual spectral range was $3500 - 6700$ Å. This is why data between May 2006 and February 2007 have a higher wavelength range.

2. On eight nights, the spectrum of the solar-analog star was saturated. In this case, a stellar spectrum from a different night was used to correct for solar reflection. This may have an impact on the quality of the subtraction.

3. All of the Elginfield spectra are tilted due to the economical design of the spectrograph. The lines are tilted by ~ 15 pixels over the whole CCD (Figure 2.6). The width of the CN line is about 60 Å, which corresponds to ~ 14 pixels. Since the tilt over the whole CCD is approximately equal to the width of the CN line, the lines will only become broader when a one-dimensional spectrum is created. Since we were searching purely for evidence of emission lines (i.e., not requiring high-resolution spectroscopy), and with the CN line being the narrowest feature, it was not important to correct the tilt.

4. The sensitivity for the Elginfield system drops rapidly for wavelengths less than 4000 Å (Figure 2.7). Therefore, even though the imaging CCD is sensitive at
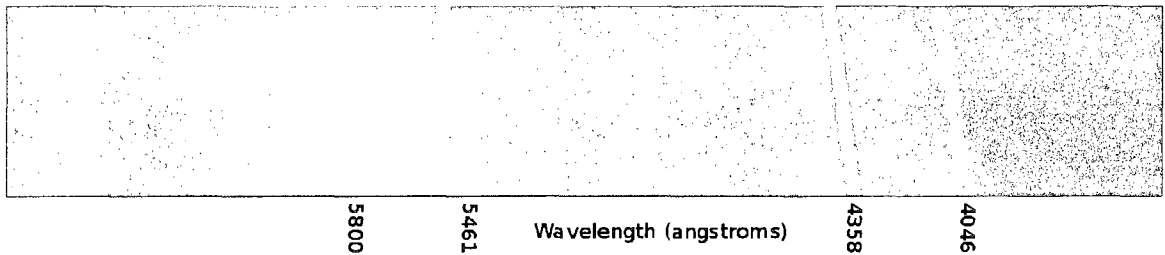
Figure 2.6: A spectrum of a fluorescent lamp to demonstrate the tilt of all spectra taken with the Elginfield telescope system.
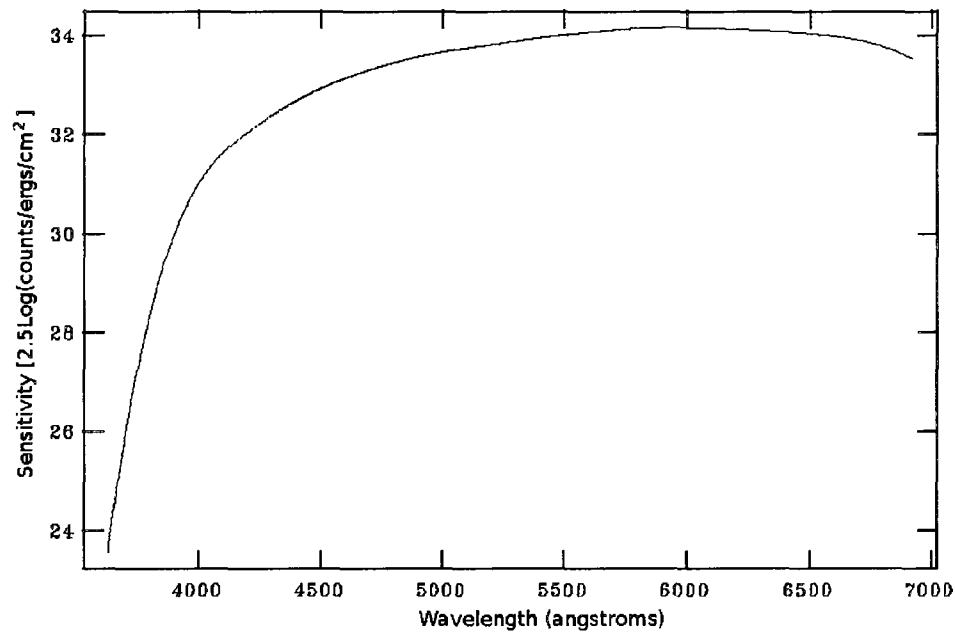

Figure 2.7: Sensitivity function for the Elginfield system. Note the large drop in sensitivity for wavelengths less than 4000 Å.

these wavelengths (Figure 2.8), the spectra will still have low signal-to-noise ratios in that region. The reason for the system efficiency drop is unknown, but could be due to coatings on the telescope mirrors or optics in the spectrograph itself.

5. The limiting magnitude for the Elginfield system was initially calculated to be $V \sim 16$ mag. Although objects this faint could be detected on the guiding CCD, the auto-guiding system could not be used because of the long integration times
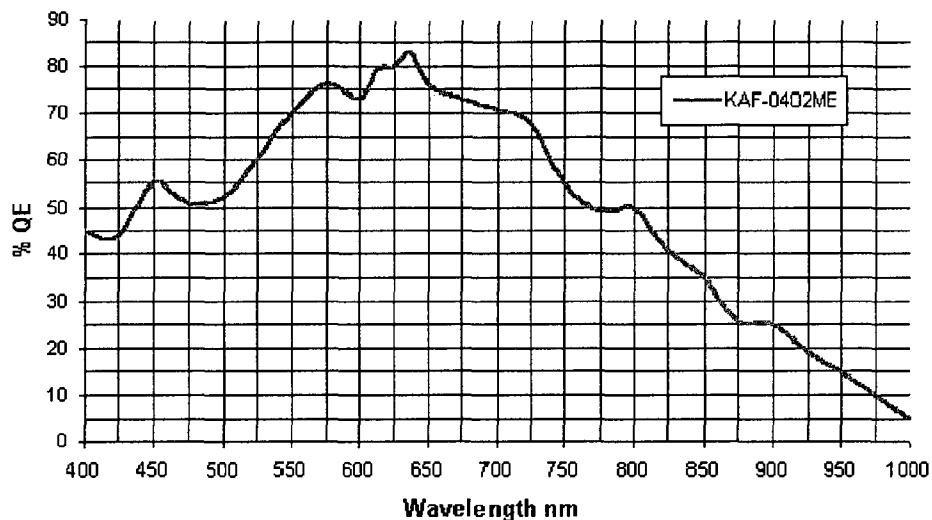
Figure 2.8: Quantum efficiency of the SBIG imaging CCD. Courtesy of SBIG.

needed to track an object ($\gtrsim$ 3 min for an object with $V \sim$ 16 mag). Therefore, most objects observed had $V \lesssim$ 15.

6. Initially, only asteroids with comet-like orbits (i.e., high eccentricities and inclinations) were to be observed; however, there were very few such objects observable on a given night (typically $\lesssim$ 1). Therefore, the target list was expanded to include all observable asteroids within the limiting magnitude.

2.4   Analysis and Results

To determine whether an asteroid shows evidence for cometary activity, emission lines from gas production are searched for. As mentioned previously, the CN line at 3880 Å is generally strong among comets, even out to large distances from the Sun. Due to the micrometer issues mentioned in section 2.3.3 #1, not all spectra have wavelength ranges that encompass this line. To address this, three other emission lines at longer

Table 2.1: Molecule parameters

Molecule	Wavelength Range (Å)	g-factor (erg s^{-1} mol^{-1})[a]
CN ($\Delta v = 0$)[b]	$3840 - 3900$	3.7×10^{-13}
C_3	$3950 - 4100$	1.0×10^{-12}
C_2 ($\Delta v = +1$)	$4550 - 4750$	4.5×10^{-13}
C_2 ($\Delta v = 0$)	$5000 - 5200$	4.5×10^{-13}

[a]values from A'Hearn et al. (1995); mol is short for molecule.
[b]Δv denotes vibrational transition.

wavelengths are looked for (Table 2.1).

The absolute flux upper limits of a given emission line are determined by measuring the zero-to-peak noise in the band (Table 2.1) and multiplying by the number of pixels across the band (as in Fink & Hicks, 1996, and Chapter 3). To derive upper limits of the gas production rate, the following relation is used (discussed in Chapters 1 and 3, and derived in Appendix A):

$$Q = \frac{16\pi \Delta v_e F}{3g\theta}, \tag{2.1}$$

where Δ is the geocentric distance of the comet (cm), v_e is the expansion velocity of the observed molecule (cm s^{-1}), F is the absolute flux (erg cm^{-2} s^{-1}), g is the fluorescence efficiency, or g-factor (erg s^{-1} mol^{-1} - mol is short for molecule), and θ is the slit width (rad). The production rate, Q, has units of mol s^{-1}. The expansion velocity is assumed to be 1 km s^{-1} (c.f., A'Hearn et al., 1995), and the slit width is 2″ and 1.5″ for the Elginfield and DAO telescopes, respectively.

The values of g for each molecule measured are listed in Table 2.1 (A'Hearn et al., 1995). Each are scaled by r_H^{-2} (where r_H is the heliocentric distance) for the gas production rate calculations. The g-factor for the CN molecule deviates from the r_H^{-2} dependence because of the Swings effect (Chapter 1). Its value ranges between

$2.58-4.80\times10^{-13}$ erg s^{-1} mol^{-1} for heliocentric distances of $0.5-6.0$ AU and velocities -50 to $+50$ km s^{-1} (Tatum, 1984). Since many approximations have already been made to calculate the production rate (see Chapters 1 and 3, and Appendix A), and since only the upper limits are being derived, this effect was not taken into account in this study.

No asteroidal object in either data set showed visual evidence for any emission line. The upper limits of the production rates for each object are listed in Appendix B.

2.4.1   Cross Correlation

A more sensitive technique to determine whether an asteroid shows gas emission is to cross-correlate the spectrum with an active comet spectrum. Cross-correlation is a measure of the similarity of two waveforms. It can be achieved using the FXCOR tool in IRAF, which shifts the x-axis (wavelength) of the object's spectrum along the x-axis of the template's (active comet) spectrum, and multiplies the two spectra at each step (size is set by the user) to give a correlation factor. The output gives the maximum correlation factor and what shift had to be applied to the object's spectrum to achieve it. Strong correlations have factors ~ 1, while strong anti-correlations have factors ~ -1.

Since the spectra are wavelength calibrated, we look for the maximum correlation factor to occur at zero wavelength shift. None of the asteroidal objects satisfy this constraint when cross-correlated with a spectrum of comet 17P (Figure 2.9, used because it was the only observed object to show emission lines), and therefore none show evidence of being cometary in nature.

2.4.2 Active Comets

In addition to observing 101 asteroids, six comets were observed with the Elginfield telescope (Table 2.2). Table 2.3 lists the observational geometry and the derived gas production rates for each comet. Comet 17P was observed approximately five days after it increased in brightness by 14 mag (Snodgrass et al., 2007) - the cause of which is unknown, but could have been from an impact, splitting, or a build-up of gas under the surface (Altenhoff et al., 2009) - and was the only object to show distinct emission line features (Figure 2.9). The lack of emission lines from the other comets is most likely due to their heliocentric distances, or their physical ages (i.e., older comets, such as Jupiter-family comets, show weaker/fewer emission lines; see Chapter 3). Therefore, the production rates quoted for 17P are actual values, and the errors are derived using the uncertainty of the location of the continuum. All other production rate values are upper limits.

2.5 Discussion

To determine whether this program is feasible, the resulting upper limits can be compared to previous results. Chamberlin et al. (1996) reported an upper limit of the CN production of $(0.4 - 1) \times 10^{23}$ mol s^{-1} for three candidate TOs. The only spectroscopic observation of a known MBC (2008 R1) gave an upper limit of CN gas production of 1.4×10^{23} mol s^{-1} (Jewitt, Yang & Haghighipour 2009, discussed below). Active comets typically have CN productions of 10^{23-26} mol s^{-1}, for weak to strong activity, respectively (Cochran et al., 1992; A'Hearn et al., 1995; Chapter 3).
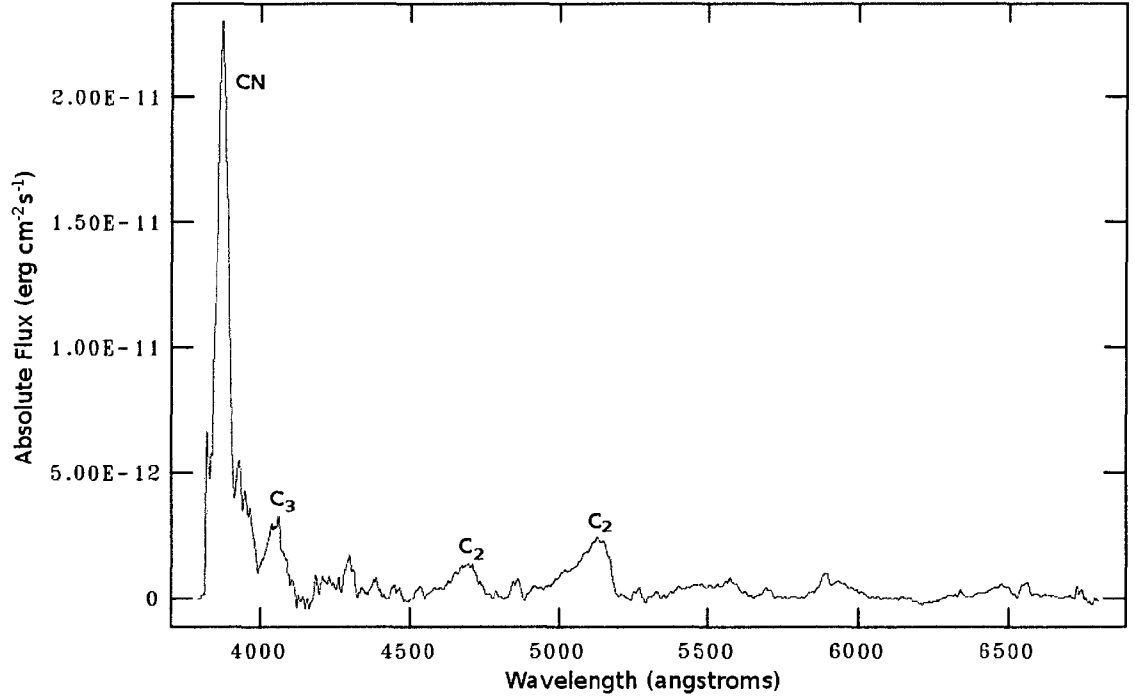
Figure 2.9: Co-added, continuum-subtracted, absolute-flux-calibrated spectrum of comet 17P. The CN, C_3 and two C_2 emission lines discussed in the text are labelled.

Table 2.2: Orbital parameters of observed comets.[a]

Object	a (AU)	e	i (^{o})	T_J	Class[b]
17P	3.617	0.432	19.113	2.859	JFC
29P	5.986	0.044	9.390	2.984	JFC
73P-E	3.062	0.694	11.406	2.782	JFC
102P	3.740	0.472	26.262	2.732	JFC
2006 HR30	7.818	0.843	31.885	1.785	HTC
2006 M4	-4234.370	1.000	111.823	0.071	NOC

[a]All values are from the JPL Small-Body Database Browser; a is the semi-major axis, e is the eccentricity, i is the inclination, and T_J is the Jupiter Tisserand parameter (given by $T_J = a_J/a + 2\cos i\sqrt{a(1 - e^2)/a_J}$).

[b]JFC = Jupiter family comet; HTC = Halley type comet; NOC = new Oort cloud comet.

Table 2.3: Observational geometry[a] and production rates for comets.

Object	Date (UT)	Exp. (s)[b]	Δ (AU)	r_H (AU)	V (mag)[c]	log Q (mol s^{-1})			
						CN	C_3	C_2 ($\Delta v = 1$)	C_2 ($\Delta v = 0$)
17P	29 Oct 2007	3360	2.456	1.626	2.7(T)	27.67 (44)[d]	26.6 (21)	26.76 (17)	27.08 (29)
29P	02 Oct 2006	420	5.295	5.845	14.39(T)	—	—	—	< 27.96
73P-E	02 Oct 2006	720	0.809	1.775	13.68(T)	—	—	—	< 26.16
102P	05 Aug 2006	480	1.921	2.036	19.19(T)	—	—	—	< 26.69
	02 Oct 2006	420	1.583	2.199	19.03(T)	—	—	—	< 26.54
2006 HR30	30 Aug 2006	480	1.142	2.066	16.72(T)	—	—	—	< 26.5
	24 Feb 2007	900	0.916	1.433	13.85(T)	< 27.25	< 26.8	< 26.11	< 25.89
2006 M4	25 Nov 2006	780	1.492	1.311	12.68(T)	—	—	< 26.01	< 26.07

[a]Values of Δ, r_H, and V, are from JPL Horizons.
[b]Refers to total exposure time of co-added observations
[c](T) denotes total magnitude.
[d]Numbers in brackets are percent uncertainty.

On average, the upper limit of the CN production rate was 5×10^{27} and 5×10^{25} mol s^{-1} for the asteroids observed with the Elginfield and DAO telescopes, respectively. This is $2-4$ orders of magnitude higher than those reported by Chamberlin et al. (1996) and Jewitt, Yang & Haghighipour (2009). Therefore, this study is not feasible using the Elginfield instrument package.

This study was limited by the following challenges: the sensitivity function, the auto-guiding, and the number of objects observable each night. Initially, the Elginfield system was derived to be able to observe a signal-to-noise ratio (SNR) of 10, assuming a two-hour exposure of a 16th magnitude object. This SNR would have been sufficient to observe spectral lines. However, because the sensitivity function for the Elginfield system dropped rapidly below 4000 Å (even though the CCD efficiency is $\sim 40\%$ in this wavelength region), the spectra had lower SNRs.

The auto-guiding was not as effective as expected. As stated above, the exposure times needed to track a faint object were fairly long, and therefore the object was no longer on the slit by the time the exposure of the spectral CCD was taken. In addition, the auto-guiding would periodically turn off, or not connect to the telescope properly, and the object would be lost. These issues limited the ability to observe faint objects (i.e., $V \gtrsim 15$), and therefore limited the number of objects that could have been observed.

Finally, there are a limited number of objects that have the required geometries and brightness which are also observable from the location of Elginfield on a given night. For example, on the night of 2009 April 29 UT, there were 12 objects with $\Delta > 1$ AU, $r_H < 2$ AU, and $V < 15$ mag, only eight of which were observable

from Elginfield. Although this number seems reasonable, these are the only objects observable for a certain time period (i.e., an average of 1 − 3 weeks). At this rate, observing hundreds of objects to improve on the results presented in Hsieh & Jewitt (2006) would take many years.

Recently, Jewitt, Yang & Haghighipour (2009) reported spectroscopic observations of newly found MBC 2008 R1 at $r_H = 1.861$ AU. They reported the spectrum showed no emission line features despite an observable coma, and derived an upper limit to the CN production of 1.4×10^{23} mol s^{-1}. They concluded this low gas-production rate is consistent with a scenerio in which most of the gas has left the region of the nucleus, leaving behind a coma consisting mostly of the slower moving dust particles. This implies that, even when MBCs are active, they may not produce emission lines from gas production. Therefore, this may not be an efficient method to search for these types of objects.

2.6   Conclusions

The Elginfield telescope near London, Ontario, does not allow for an improvement on the upper limits of the CN production rates using the current observations. Due to a few challenges (i.e., the sensitivity function, problems with the auto-guiding, and the limited number of observable objects) this project is not feasible.

This equipment can be used to take spectroscopic observations of active comets in order to derive gas production rates of CN, C_3, C_2, and other species. Such obser-vations are ideal for the Elginfield telescope, as it is relatively easy to obtain target-

of-opportunity time on the instrument, and does not require a dedicated (nightly) observer.

The results reported by Jewitt, Yang & Haghighipour (2009) indicate that MBCs may not produce emission lines even when active. This result is inconclusive because 2008 R1 was observed at $r_H = 1.861$ AU, where the coma may be dominated by dust particles. However, if accurate, it indicates searching for MBC candidates using spectroscopic observations would not be effective. It would be beneficial to acquire spectroscopic observations of each known MBC while in active phase to provide additional information.

These results prompted the addition of two studies to this thesis work: spectroscopic observations of active comets, including new Oort cloud comet 2006 VZ13 (Chapter 3), and an extensive search for MBCs using the CFHT Legacy Survey image archives (Chapter 4).

References

A'Hearn, M., Millis, R., Schleicher, D., Osip, D., Birch, P., 1995. The ensemble properties of comets: Results from narrowband photometry of 85 comets, 1976-1992. Icarus 118, 223.

Altenhoff, W., Kreysa, E., Menten, K., Sievers, A., Thum, C., Weiss, A. 2009. Why did comet 17P/Holmes burst out? Nucleus splitting or delayed sublimation? A&A 495, 975-978.

Binzel, R., Rivkin, A., Stuart, S., Harris, A., Bus, S., Burbine, T. 2004. Observed

spectral properties of near-Earth objects: results for population distribution, source regions, and space weathering processes, Icarus 170, 259-294.

Chamberlin, A., McFadden, L.-A., Schulz, R., Schleicher, D., Bus, S. 1996. 4015 Wilson-Harrington, 2201 Oljato, and 3200 Phaethon: Search for CN emission. Icarus 119, 173-181.

Cochran A., Barker E., Ramseyer T. Storrs, A., 1992. The McDonald observatory faint comet survey: Gas production in 17 comets. Icarus, 98, 151-162.

Elst, E., Pizarro, O., Pollas, C., Ticha, J., Tichy, M., Moravec, Z., Offutt, W. Marsden, B. 1996. Comet P/1996 N2 (Elst-Pizarro). IAU Circ. 6456, 1.

Feldman P., Cochran A., Combi M., 2003. Spectroscopic investigations of fragment species in the coma, in Festou M., Keller H., Weaver H., eds, Comets II. Tuscon: The University of Arizona Press, 425-448.

Fink, U., Hicks, M. 1996. A survey of 39 comets using CCD spectroscopy. ApJ 459, 729-743.

Harris, A., Delbó, M., Binzel, R., Davies, J., Roberts, J., Tholen, D., Whiteley, R. 2001. Visible to thermal-infrared spectrophotometry of a possible inactive cometary nucleus. Icarus 153, 332-337.

Hsieh, H., Jewitt, D. 2006. A population of comets in the main asteroid belt. Science 312, 561-563.

Jewitt, D., Yang, B., Haghighipour N. 2009. Main-belt comet P/2008 R1 (Garradd). AJ 137, 4313-4321.

Read, M., Bressi, T., Gehrels, T., Scotti, J., Christensen, E. 2005. Comet P/2005 U1 (Read). IAU Circ. 8624, 1.

Snodgrass, C., Fitzsimmons, A., Boehnhardt, H., Lister, T., Naylor, T., Bell, C., Colas, F., Lecacheux, J., Sostero, G., Guido, E., Young, J., McGaha, J. 2007. Comet 17P/Holmes. CBET 1111, 1.

Tatum, J. 1984. Cyanogen radiance/column-density ratio for comets calculated from the Swings effect. AA 135, 183-187.

Tody, D. 1993, IRAF in the nineties, in Hanisch R.J., Brissenden R.J.V., Barnes J., eds., Astronomical Data Analysis Software and Systems II, A.S.P. Conference Ser. 52, 173-183.

Chapter 3

Spectroscopic Observations of New Oort Cloud Comet 2006 VZ13 and Four Other Comets[1]

This one description ought to be generally agreed upon: [A comet is]
an unusual star of strange appearance...seen trailing fire which streams around it.

- Seneca, Natural Questions, Book 7, "Comets"

3.1 Introduction

As discussed throughout this thesis, the icy nature of comets indicate they have

been preserved at cold temperatures since the early stages of Solar System formation.

Consequently, they are commonly considered to be among the most primitive objects

---

[1]A version of this chapter has been submitted: Gilbert, A.M., Wiegert P.A., Unda-Sanzana, E., Vaduvescu, O., 2009. Spectroscopic observations of new Oort cloud comet 2006 VZ13 and four other comets. Submitted to MNRAS.

in the Solar System. Determining their physical and chemical properties, and how they evolve, is important to our understanding of the formation of planetary systems, both our own and in general.

Several surveys have attempted to study and classify the chemical composition and evolution of comets. A'Hearn et al. (1995) conducted a photometric survey of 85 different comets over almost 20 years. Their findings indicated two major classes of comets: those that are carbon-depleted and those that are not. They found nearly all members of the carbon-depleted class are Jupiter family comets (JFCs), although not all JFCs are carbon-depleted. They also reported little variation of relative gas production rates with heliocentric distance or apparition; however, they noted a correlation between the dust-to-gas ratio and perihelion distance.

Three major spectroscopic surveys have also been conducted: Newburn & Spinrad (1989) reported spectrophotometry of 25 comets; Cochran et al. (1992) derived production rates for 17 faint comets; and Fink & Hicks (1996) surveyed the spectra of 39 comets out to infrared wavelengths. The first two surveys utilized the image dissector technique, while the third used long-slit CCD spectroscopy.

The three surveys found slightly different results. Newburn & Spinrad (1989) reported a correlation between CN and dust, and that the C_2/CN production ratio changed with heliocentric distance. Cochran et al. (1992), however, found the gas production ratios remained constant with activity level and heliocentric distance, except for NH_2/CN. Fink & Hicks (1996) concluded that most comets have roughly the same production rate ratios to within a factor of 2 or 3, although 10% of comets could be considered outliers.

Comet 2006 VZ13 (LINEAR) was discovered in November 2006 (Sponsetti et al., 2006). This is a new Oort cloud comet which passed perihelion on 10 August 2007. This presented a unique opportunity to observe a pristine comet as it passed perihelion, and it was observed with the Cerro-Tololo Inter-American Observatory (CTIO) 1.5-m telescope. In addition, four other comets were observed with the same instrument and under the same observing conditions: 2006 K4 (NEAT), 2006 OF2 (Broughton), 93P/Lovas I, and 2P/Encke. These comets represent a broad range of dynamical class, age, brightness, and heliocentric distance. This allows for a comparison of production rates and ratios between comets of different classes and ages.

In this chapter, spectroscopic observations are presented of five comets, obtained in August 2007 (Table 3.1). The production rates of CN, C_2, and C_3 are calculated, and the production ratios with respect to CN are derived. This analysis technique is similar to that presented in Chapter 2, where upper limits of CN, C_2, and/or C_3 gas production were calculated for almost 100 objects, including six active comets. In addition, dust production rates and dust-to-gas ratios are calculated for the five CTIO comets.

3.2   Observations

Observations of 2006 VZ13, 2006 K4, 2006 OF2, 2P, and 93P were obtained during 2007 August 6–15 (UT) with the CTIO 1.5 m telescope. Table 3.1 lists the orbital parameters for each comet, and Table 3.2 summarizes the observations.

Table 3.1: Orbital elements of the comets.[a]

Comet	a (AU)	e	i (°)	q (AU)	Q (AU)	T_J	Peri. Date (UT)	Comet Class[b]
2P/Encke	2.217	0.847	11.766	0.339	4.095	3.026	2007 Apr 19	NEO
2006 K4	1805.756	0.998	111.333	3.189	3608.323	-0.802	2007 Nov 29	EOC
2006 OF2	-3367.756	1.001	30.171	2.431	n/a	n/a	2008 Sep 15	NOC
2006 VZ13	-4083.355	1.000	134.793	1.015	n/a	n/a	2007 Aug 10	NOC
93P/Lovas 1	4.391	0.612	12.218	1.705	7.078	2.605	2007 Dec 17	JFC

[a]All values are from the JPL Small-Body Database Browser; a is the semi-major axis, e is the eccentricity, i is the inclination, q is the perihelion distance, Q is the aphelion distance, and T_J is the Jupiter Tisserand parameter (given by $T_J = a_J/a + 2\cos i\sqrt{a(1-e^2)/a_J}$).

[b]NEO = near Earth object; EOC = evolved Oort cloud comet; NOC = new Oort cloud comet; JFC = Jupiter family comet.

Table 3.2: CTIO observational parameters.[a]

Comet	Date (UT)	Δ (AU)	r_H (AU)	V (mag)	Exp. Time (s)
2P	07/08/07 00:16	0.9400	1.9114	15.19	3600
	07/08/07 23:56	0.9550	1.9221	15.30	3650
	13/08/07 01:30	1.0381	1.9781	15.92	5400
	14/08/07 01:14	1.0551	1.9890	16.04	5400
2006 K4	07/08/07 01:24	2.6270	3.3713	15.75	3600
	08/08/07 02:08	2.6364	3.3681	15.75	3600
	13/08/07 03:33	2.6869	3.3529	15.78	5400
	14/08/07 03:04	2.6977	3.3500	15.78	5400
	15/08/07 02:33	2.7084	3.3472	15.79	5400
2006 OF2	07/08/07 02:53	3.7934	4.7860	16.33	3600
	08/08/07 03:19	3.7825	4.7782	16.32	3600
	13/08/07 06:32	3.7316	4.7382	16.26	5400
	14/08/07 06:17	3.7226	4.7304	16.25	5400
	15/08/07 05:06	3.7143	4.7229	16.24	5400
2006 VZ13	06/08/07 23:14	1.0207	1.0175	13.26	1800
	07/08/07 23:14	1.0482	1.0165	13.32	1800
	12/08/07 23:22	1.1866	1.0159	13.58	3600
	13/08/07 23:19	1.2142	1.0166	13.64	3600
93P	08/08/07 06:03	1.4603	2.1451	16.61	7200
	15/08/07 07:36	1.3617	2.1059	16.38	9600

[a]The date indicates the start time of the first observation of the comet; Δ is the geocentric distance, r_H is the heliocentric distance, and V is the total magnitude. All values were obtained from the JPL Horizons database. The exposure time is the total of all observations on the given night.

All observations were acquired with the Cerro-Tololo Inter-American Observatory (CTIO) 1.5-m telescope and R–C spectrograph, and were taken under photometric conditions (except for the second half of the night of August 14, which was partly cloudy). The spectrograph had a Loral 1K 1200 × 800 CCD with 15-μm pixels. A Bausch & Lomb reflection grating was used with 300 lines mm^{-1}, a resolution of 8.6 Å, and a coverage of 3450 Å. A 2″ slit was used for all observations. Wavelength scales were approximately 3 Å pixel^{-1} from 3500 to 7000 Å. The CCD spatial scale was 1.13″ pixel^{-1}, with the length of the slit spanning 460″.

Bias and projector flats were obtained at the beginning of each night, and HeAr comparison lamp spectra were recorded before each new object. Each night, images of the twilight sky were obtained, which were used as an approximation of the solar spectrum (to correct for solar reflection). Standard star Feige 110 was also observed to flux calibrate the comet spectra.

3.3 Data Reduction

The data was reduced using IRAF (Tody, 1993). For each observation date, the projector flats were examined to determine portions of the chip that were not illuminated. These sections were trimmed from all images. The bias frames were combined and applied to each twilight sky flat, projector flat, lamp spectrum and object spectrum. The projector flat frames were then combined and applied to the sky flats and object spectra.

One-dimensional spectra of each sky flat and object were extracted using IRAF's

APALL tool, which traced the centre of the profile, subtracted the background sky, and corrected cosmic-ray hits. Each spectrum was wavelength calibrated using a HeAr lamp spectrum. Spectra obtained of the same object on the same night were co-added to increase the signal-to-noise ratio.

The combined sky flat image was used as an approximation of the solar spectrum to correct for solar reflection in the cometary spectra (unfortunately, spectra of a solar-analog star were not acquired). It was necessary to scale the sky flat, since the count rate was much lower than for the comets. This was accomplished by determining the average value of the counts in the 4400–4500 Å range for each comet spectrum. The sky flat was then scaled to the same height, in the same wavelength range, and subtracted. Figure 3.1 shows an example twilight sky spectrum from 2007 August 6, used to correct the comet spectra for solar reflection.

The above continuum correction was not perfect because a twilight sky spectrum was used, and, in general, left 10–20% of the continuum. To compensate for the difference, the continuum of each comet was fit again with a cubic spline function and subtracted.

The comet spectra were flux calibrated using spectra of the standard star, Feige 110. The star was observed several times per night at different airmasses. Using these observations, the effective airmass and system sensitivity function were calculated, which were then used to calibrate the comet spectra.

Figure 3.2 shows the 2007 August 13 spectrum of 2006 VZ13 with the major emission lines labelled (note the similarity to the spectrum of 17P/Holmes (Figure 2.9) presented in Chapter 2). Other known emission lines in this wavelength region include
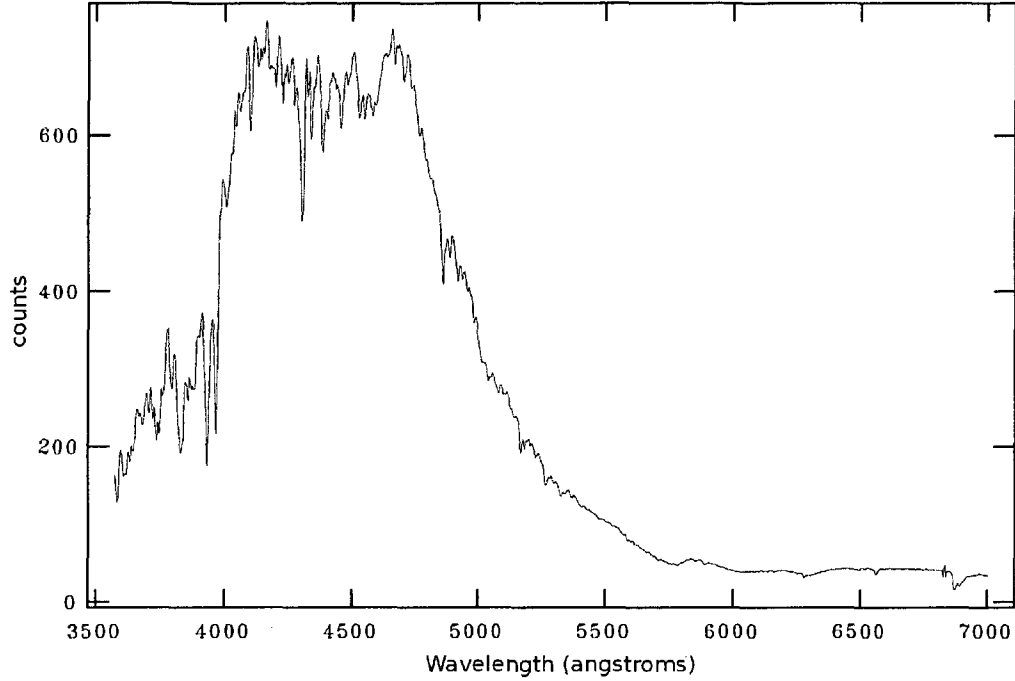
Figure 3.1: An example of the twilight sky spectrum, taken 2007 August 6, used to correct the comet spectra for solar reflection.

CH, NH, OI, CO_2^+, CH^+, OH^+, H_2O^+, and N_2^+ (Feldman, Cochran & Combi, 2004).

In addition, there are cometary emission line features that remain unidentified.

Figures 3.3–3.7 show the final one-dimensional, absolute-flux-calibrated spectra of each comet. All spectra are binned by nine pixels to improve the signal-to-noise ratio (excluding 2006 VZ13). Using the twilight sky spectrum to correct for solar reflection created false lines in the object spectra, such as those seen at approximately 7000 Å, or the absorption feature near 5100 Å.

3.4   Analysis and Results

The absolute flux above the continuum is measured of the CN, C_3, and C_2 emission features for each comet (Table 3.3). The continuum flux is also measured to calculate
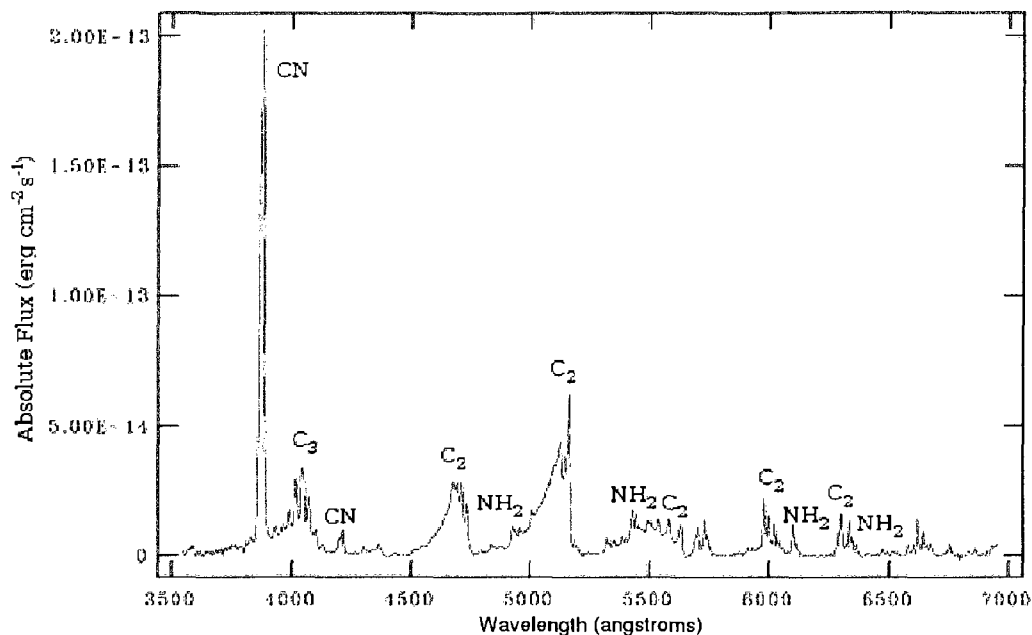
Figure 3.2: Continuum-subtracted, absolute-flux-calibrated spectrum of comet 2006 VZ13, obtained 2007 August 13. Major emission lines are labelled.
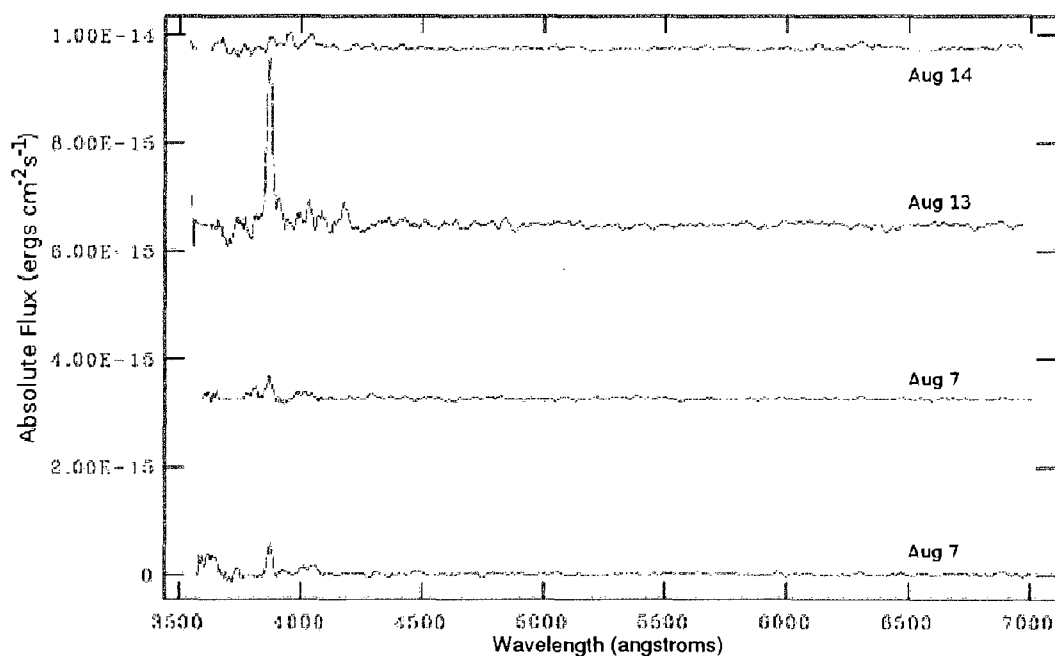
Figure 3.3: Four continuum-subtracted optical spectra of comet 2P/Encke, obtained in August 2007. Spectra are offset by a factor of 3.25×10^{-15} for clarity. Note the strong increase of the CN line on August 13.
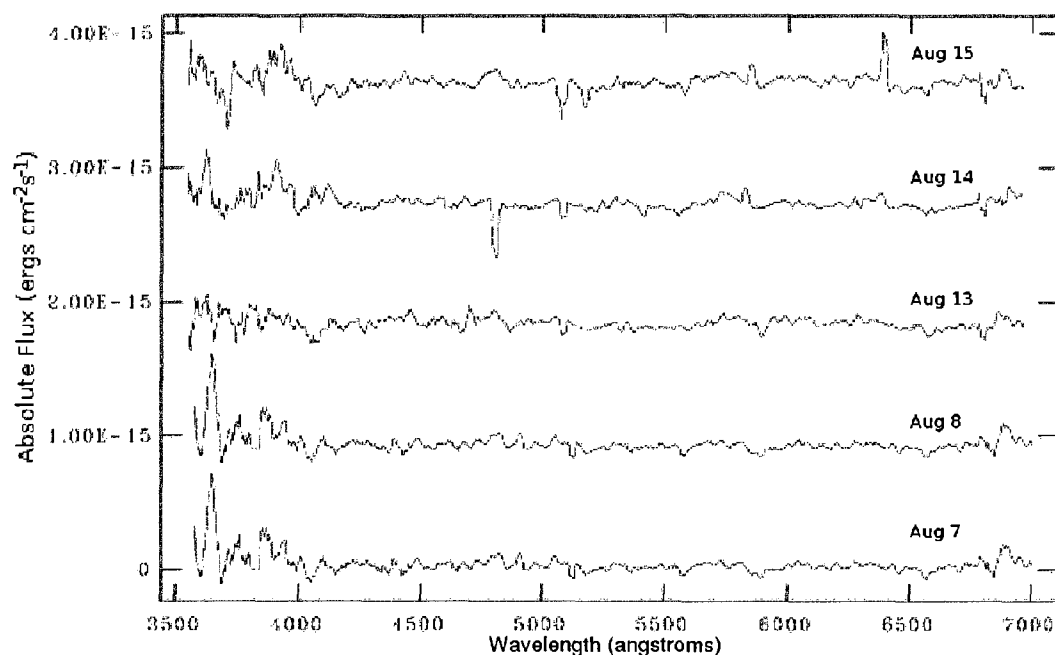
Figure 3.4: Five continuum-subtracted optical spectra of comet 2006 K4, obtained in August 2007. Spectra are offset by a factor of 9.0×10^{-16} for clarity.
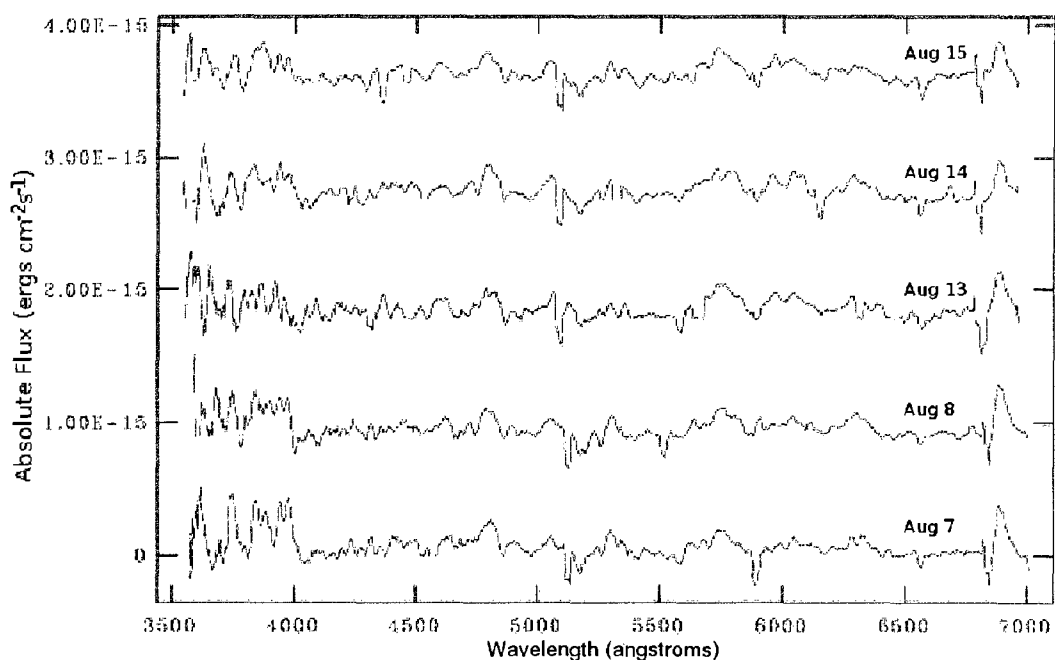
Figure 3.5: Five continuum-subtracted optical spectra of comet 2006 OF2, obtained in August 2007. Spectra are offset by a factor of 9.0×10^{-16} for clarity.
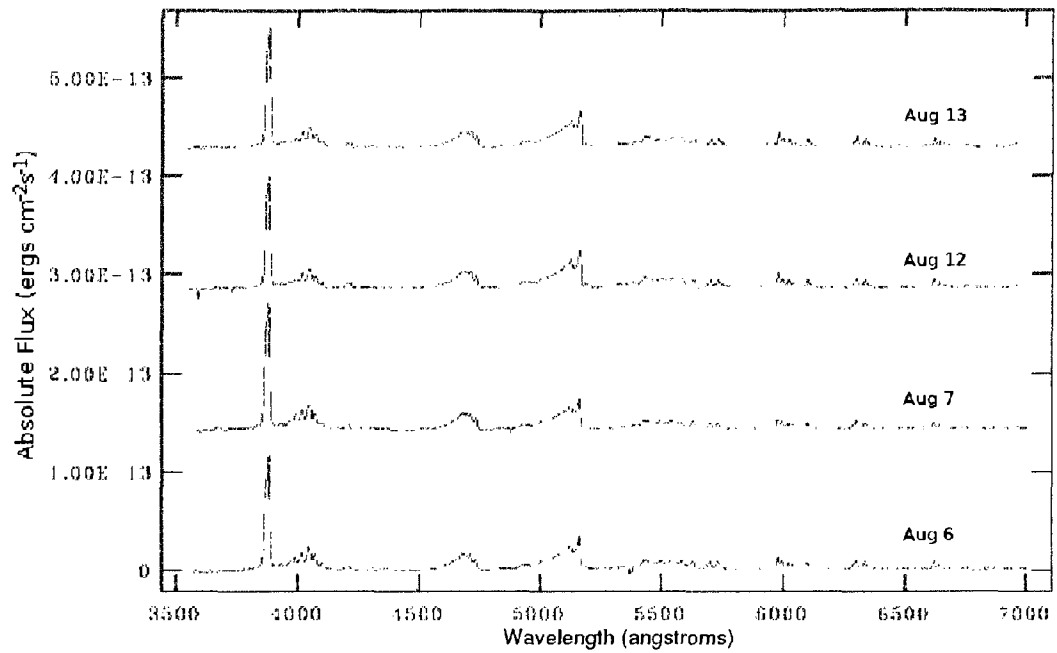
Figure 3.6: Four continuum-subtracted optical spectra of comet 2006 VZ13, obtained in August 2007. Spectra are offset by a factor of 1.45×10^{-13} for clarity.
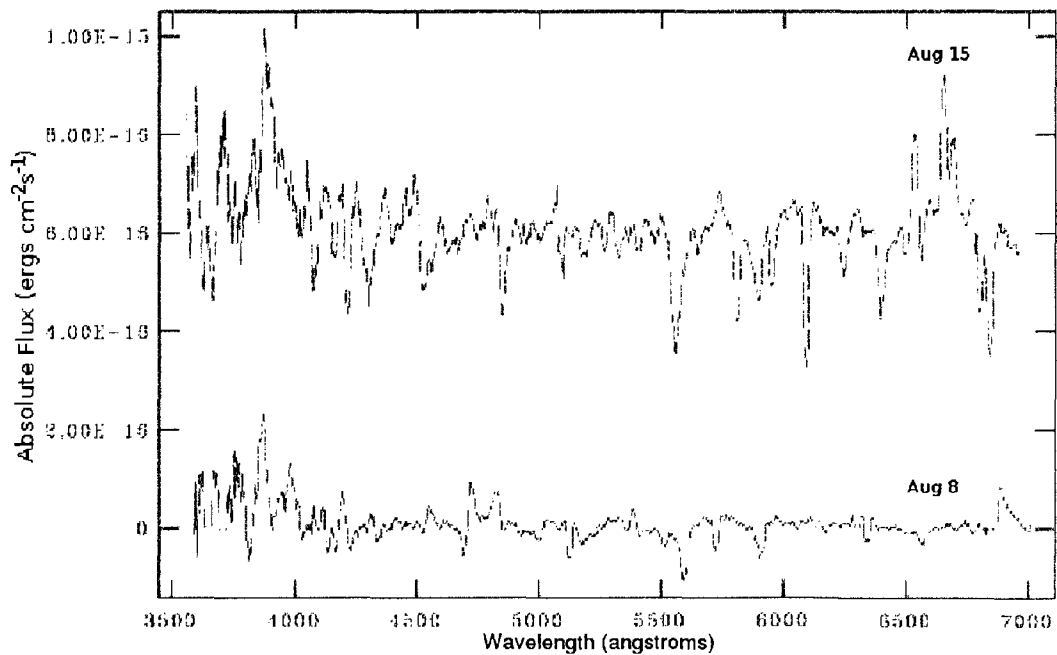
Figure 3.7: Two continuum-subtracted optical spectra of comet 93P, obtained in August 2007. Spectra are offset by a factor of 6.0×10^{-16} for clarity.

Table 3.3: Molecular line widths.

Molecule	Wavelength Range (Å)
CN $(\Delta v = 0)^a$	$3840 - 3900$
C_3	$3950 - 4100$
C_2 $(\Delta v = +1)$	$4550 - 4750$
C_2 $(\Delta v = 0)$	$5000 - 5200$

$^a\Delta v$ denotes vibrational transition.

the dust production rate.

3.4.1   Gas production

The most common procedure to convert flux to a production rate is the Haser model (Haser, 1957, discussed in Chapter 1 and Appendix A). This model assumes the main excitation mechanism is resonance fluorescence, a spherical geometry of the coma, and an exponential decay of both the parent and daughter molecules. However, previous authors (Cochran et al., 1992; A'Hearn et al., 1995) agree that conclusions can be drawn for the chemical composition of comets as long as a consistent model is used (i.e., not just the Haser model).

In this study, it is instead assumed the molecules travel the total distance of their scale length before photodissociation (the other assumptions of the Haser model are preserved). The production rate in this scenario is given by (discussed in Chapters 1 and 2, and derived in Appendix A)

$$Q = \frac{16\pi \Delta v_e F}{3g\theta} \tag{3.1}$$

where Δ is the geocentric distance of the comet (cm), v_e is the expansion velocity of the observed molecule (cm s^{-1}), F is the absolute flux (erg cm^{-2} s^{-1}), g is the fluorescence efficiency, or g-factor (erg s^{-1} mol^{-1}, where mol(s) is short for molecule(s)),

and θ is the slit width (rad). The production rate, Q, has units of mols s^{-1}. The expansion velocity for all molecules is assumed to be 1 km s^{-1}, and the slit width is $2''$.

The values of g at 1 AU are 3.7×10^{-13}, 1.0×10^{-12}, and 4.5×10^{-13} erg s^{-1} mol^{-1} for CN, C_3, and C_2, respectively (A'Hearn et al., 1995). These values are scaled by r_H^{-2} (where r_H is the heliocentric distance) for the production rate calculations. As discussed in Chapters 1 and 2, the g-factor for the CN molecule deviates from this r_H^{-2} dependence due to the Swings effect. However, this effect is not taken into consideration in this study (as in Chapter 2).

The error in the flux measurement is derived using the uncertainty of the location of the continuum. Various investigators use different values for the fluorescence efficiencies and expansion velocities, the uncertainties of which are poorly understood. Therefore, the errors in these parameters are not included in this analysis, in keeping with other studies (e.g. A'Hearn et al., 1995).

For comets showing no emission in a given band, the upper limit of the production rate is determined by measuring the zero-to-peak noise in the band and multiplying by the number of pixels across the band (as in Fink & Hicks, 1996, and Chapter 2). For the $C_2(\Delta v = 0)$ band (where Δv denotes a vibrational transition), lines were visible for most comets; however, because of a large absorption feature within this line near 5100 Å, the flux could not be measured precisely (except for 2006 VZ13). Therefore, only production rate upper limits are quoted in this case. Table 3.4 lists the calculated production rates and ratios for each comet. The numbers in parentheses give the percent error, which is the same percent error found for the flux measurement.

Comet 2P shows variability in CN production, including a very large increase on 2007 August 13, as is clearly demonstrated in Figure 3.3. Variabilities on the order of a day are not unreasonable, as the lifetime of CN molecules is approximately 10^5 s (Cochran, 1985). On 2007 August 13, there is no large increase observed in the dust production, indicating the gas and dust production rates are not related.

The comets behave as expected with heliocentric distance: the CN line is observed in all comets, which is one of the most prominent features in cometary spectra for heliocentric distances less than 3 AU (Feldman, Cochran & Combi, 2004). It has been observed for 2060 Chiron to distances over 11 AU (Bus et al., 1991). Since 2006 VZ13 passes perihelion during the observations, it is expected to show many more, and stronger, emission lines, than the other comets which are at larger heliocentric distances.

The distributions of C_3, $C_2(\Delta v = +1)$, and $C_2(\Delta v = 0)$ production rates, as a function of the CN production rate, are plotted in Figure 3.8. The correlation between the species is apparent. The best-fitting slopes are 0.915 ($\sigma = 0.114$), 1.117 ($\sigma = 0.112$), and 1.241 ($\sigma = 0.101$), respectively. All species seem to show deviations from unity, implying a non-linearity in the production of those molecules (Cochran et al., 1992). However, this effect may be model-dependent, and Cochran (1987) did not report a non-linearity in their study of bright comets. The uncertainties are also large, so the production of the molecules is consistent with a linear relationship.

Table 3.4: Production rates and production rate ratios.

| Comet	r_H (AU)	log Q (mol s^{-1})				log Q-ratios		
		CN (%)	C$_3$ (%)	C$_2$ (%) $\Delta v = +1$	C$_2$ (%) $\Delta v = 0$	C$_3$/CN (%)	C$_2$/CN (%) $\Delta v = +1$	C$_2$/CN (%) $\Delta v = 0$
2P	1.9114	23.84 (2.2)	23.35 (19)	< 23.25	< 23.33	-0.488 (19)	< -0.581	< -0.502
	1.9221	23.75 (0.44)	23.13 (24)	< 23.12	< 23.05	-0.624 (24)	< -0.634	< -0.699
	1.9781	24.71 (17)	23.59 (65)	< 23.55	< 23.53	-1.117 (67)	< -1.156	< -1.179
	1.9890	23.58 (50)	23.63 (137)	< 23.37	< 23.51	0.047 (146)	< -0.219	< -0.075
2006 K4	3.3713	24.74 (18)	< 24.51	< 24.36	< 24.47	< -0.229	< -0.386	< -0.273
	3.3681	24.98 (65)	< 24.74	< 24.34	< 24.36	< -0.239	< -0.636	< -0.615
	3.3529	24.62 (89)	< 24.73	< 25.04	< 24.76	< 0.104	< 0.422	< 0.141
	3.3500	24.81 (146)	< 24.77	< 24.90	< 24.46	< -0.040	< 0.085	< -0.350
	3.3472	24.58 (73)	< 24.71	< 24.40	< 24.36	< 0.128	< -0.184	< -0.221
2006 OF2	4.7860	25.32 (105)	< 25.44	< 25.11	< 25.12	< 0.118	< -0.215	< -0.196
	4.7782	25.27 (124)	< 25.31	25.14 (74)	< 25.13	< 0.041	-0.125 (145)	< -0.142
	4.7382	25.31 (65)	< 25.33	25.48 (74)	< 25.53	< 0.015	0.165 (98)	< 0.215
	4.7304	25.24 (132)	< 25.31	25.41 (40)	< 25.40	< 0.068	0.169 (137)	< 0.162
	4.7229	25.48 (72)	< 25.32	25.45 (69)	< 25.38	< -0.153	-0.023 (100)	< -0.101
2006 VZ13	1.0175	25.58 (10)	24.98 (53)	25.31 (15)	25.54 (29)	-0.603 (54)	-0.268 (18)	-0.041 (31)
	1.0165	25.68 (16)	25.08 (48)	25.34 (19)	25.55 (29)	-0.605 (50)	-0.341 (25)	-0.140 (33)
	1.0159	25.88 (10)	25.21 (46)	25.68 (27)	25.93 (33)	-0.677 (47)	-0.201 (28)	0.046 (35)
	1.0166	25.89 (15)	25.21 (52)	25.60 (28)	25.84 (30)	-0.685 (54)	-0.295 (32)	-0.051 (33)
93P	2.1451	23.87 (35)	< 23.82	< 23.79	< 23.04	< -0.057	< -0.088	< -0.833
	2.1059	24.15 (74)	< 23.94	23.56 (30)	< 23.89	< -0.212	-0.595 (80)	< -0.260
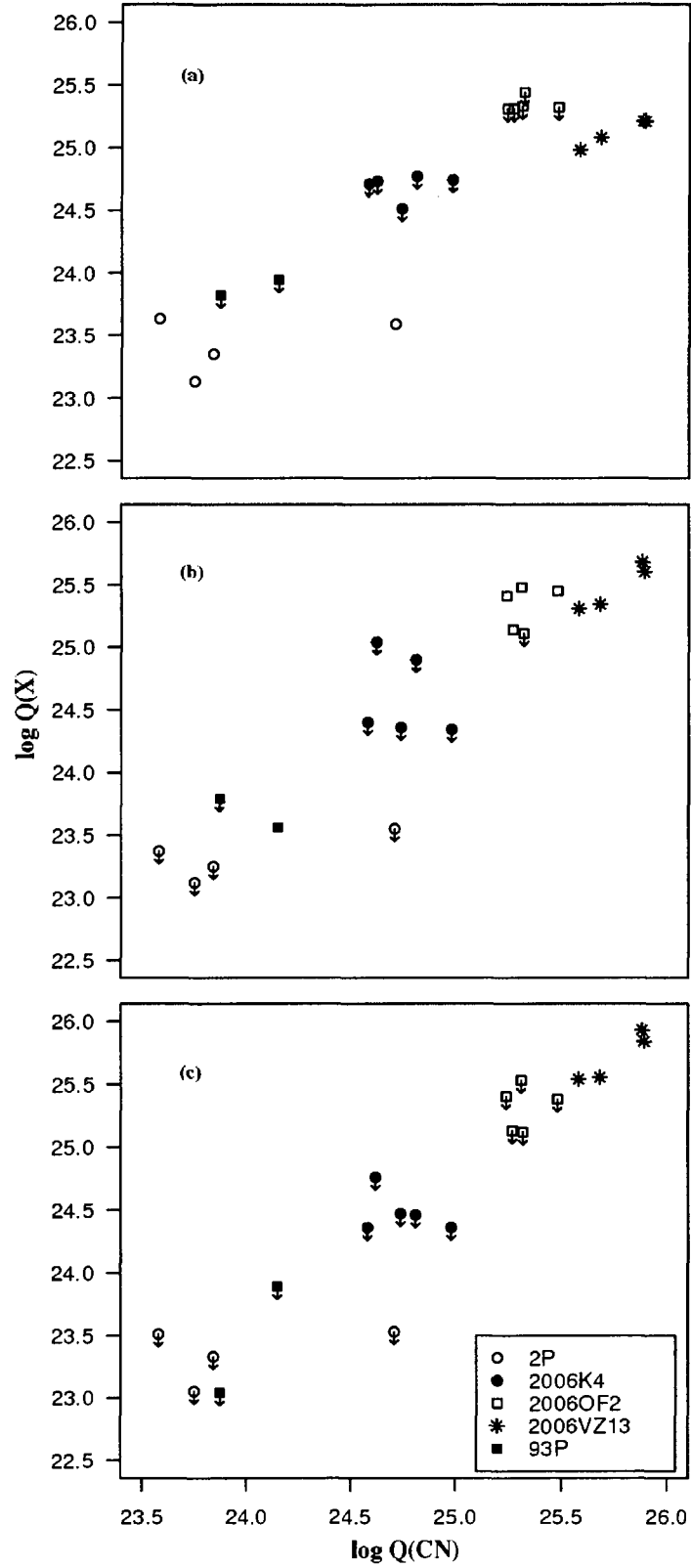
Figure 3.8: Production rates of (a) C_3, (b) $C_2(\Delta v = +1)$, and (c) $C_2(\Delta v = 0)$, with respect to CN. Downward arrows represent upper limits; see Table 3.4 for uncertainties of other points. See text for best-fitting slope parameters.

The comets can be classified according to the criteria listed in A'Hearn et al. (1995): carbon-depleted or "typical". Comets that have $\log(Q(C_2)/Q(CN)) < -0.18$ are considered carbon-depleted, while typical comets have values greater than this. Using the average values of $\log(Q(C_2)/Q(CN))$ (for both $\Delta v = 0$ and $+1$) for each comet, it is found that 2P, 2006 K4, and 93P are carbon-depleted, having average ratios of -0.631, -0.202, and -0.444, respectively. Both 2006 OF2 and 2006 VZ13 could be placed in the typical class, with average ratios of -0.161 ± 0.047 and -0.009, respectively. However, the scatter in the measurements makes this assessment uncertain.

The values of C_2/CN reported in the literature vary widely for individual comets. A'Hearn et al. (1995) report dynamically older comets (i.e., JFCs) are generally carbon depleted, and dynamically newer comets are not. However, they find 2P (a JFC) is a typical comet, with $\log(Q(C_2)/Q(CN)) = -0.06$. Fink & Hicks (1996) also observe comets 2P and 93P, and report ratios of 0.282 and 0.125, respectively, implying both comets have typical composition. In contrast, Newburn & Spinrad (1989) derive a ratio for 2P of -0.184, putting it in the carbon-depleted class, agreeing with the results presented here.

These discrepancies could be due to at least two factors: the model used to calculate the production rate and the orbital parameters at the time of observation. Different models are used for each study, and there are large uncertainties associated with them (discussed above). The orbital parameters at the time of observation are also quite different: A'Hearn et al. (1995) and Fink & Hicks (1996) observed 2P at $0.53 < r_H < 1.23$ AU and $r_H = 0.57$ AU, respectively; while it was observed at

1.91 $< r_H <$ 1.99 AU and $r_H = 1.89$ AU for this study and Newburn & Spinrad (1989), respectively; much greater distances. Fink & Hicks (1996) observed comet 93P at $r_H = 1.68$ AU, while the observations here were from 2.11 $< r_H <$ 2.145 AU. Since comets observed at large heliocentric distances do not produce all emission lines, this affects how comets are classified as either carbon-depleted or typical.

Figure 3.9 shows the production rate ratios (with respect to CN) as a function of heliocentric distance. There appears to be a slight correlation between each ratio and distance. However, because the heliocentric range for each comet is small and the uncertainties for most of the observations are large, this is not conclusive.

3.4.2 Dust production

A proxy for the dust production rate can be calculated using the expression derived by A'Hearn et al. (1984) (discussed in more detail in Chapter 1):

$$Af\rho = \frac{(2\Delta r_H)^2}{\rho} \frac{F_\lambda}{F_\odot} \tag{3.2}$$

where A is the Bond albedo, f is the filling factor of the grains in the field of view, and ρ is the linear radius of the telescope aperture at the comet (cm). F_λ is the mean cometary flux in the range of 6230 $-$ 6270 Å, and $F_\odot$ is the solar flux in the same wavelength range (both in erg cm^{-2} s^{-1} Å^{-1}), calculated here using the values in Arvesen, Griffin & Pearson (1969). The heliocentric (r_H) and geocentric (Δ) distances are in AU and cm, respectively. If the cometary dust is assumed to flow away from the nucleus in a uniform manner, without breakup, acceleration, or darkening, then the quantity $Af\rho$ (cm) is proportional to the dust production rate (A'Hearn et al., 1984; Storrs et al., 1992).
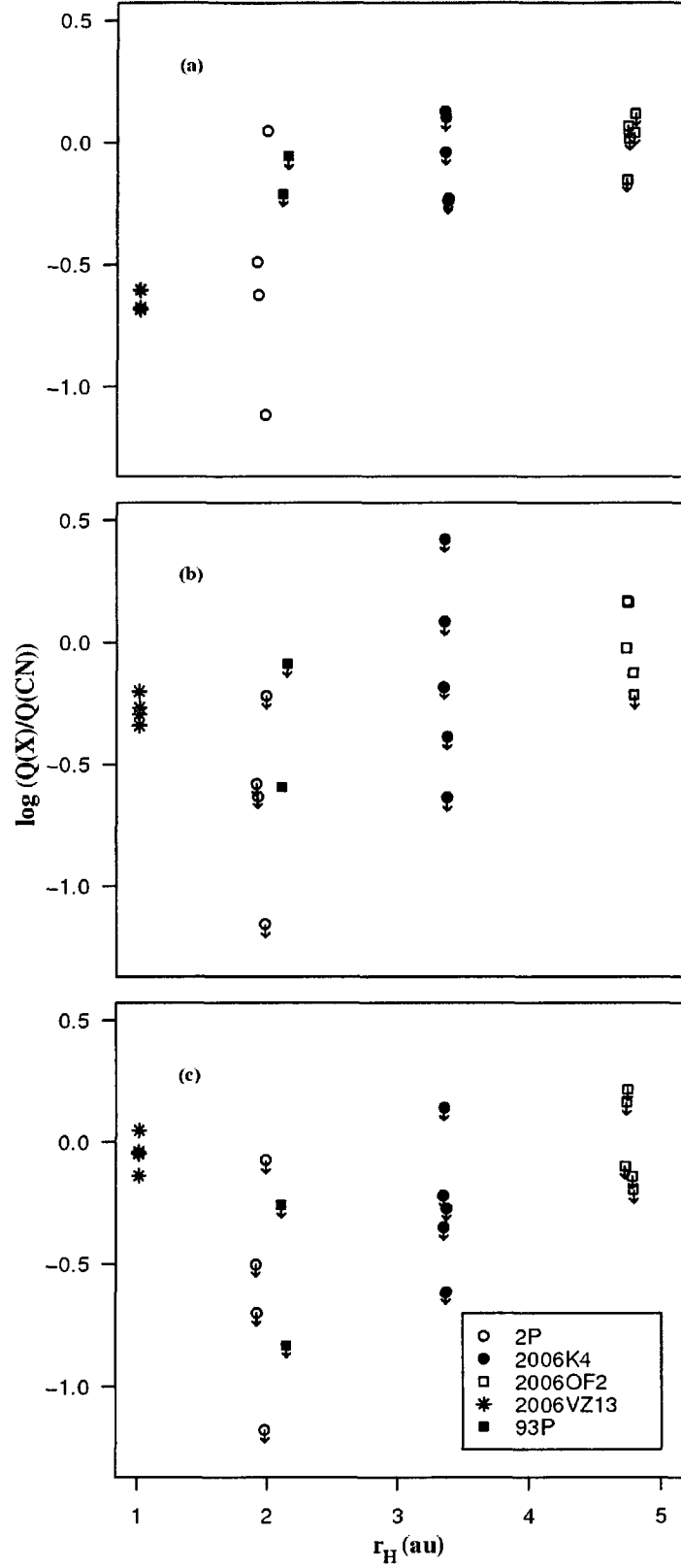
Figure 3.9: Production rate ratios of (a) C_3/CN, (b) $C_2(\Delta v = +1)$/CN, and (c) $C_2(\Delta v = 0)$/CN, as a function of heliocentric distance. Downward arrows represent upper limits; see Table 3.4 for uncertainties of other points.

Table 3.5: Dust production.

Comet	r_H (AU)	$Af\rho$ (%) (cm)	$\log(Af\rho/Q(\mathrm{CN}))$ (%) (cm s mol^{-1})
2P	1.9114	2.02 (46)	-23.53 (46)
	1.9221	1.06 (49)	-23.72 (49)
	1.9781	1.84 (56)	-24.44 (56)
	1.9890	2.96 (34)	-23.11 (34)
2006 K4	3.3713	63.1 (7.1)	-22.94 (7.1)
	3.3681	48.0 (9.2)	-23.29 (9.2)
	3.3529	104 (12)	-22.61 (12)
	3.3500	79.3 (11)	-22.91 (11)
	3.3472	84.8 (12)	-22.65 (12)
2006 OF2	4.7860	398 (3.5)	-22.72 (3.5)
	4.7782	351 (4.2)	-22.72 (4.2)
	4.7382	643 (5.9)	-22.5 (5.9)
	4.7304	617 (5.5)	-22.45 (5.5)
	4.7229	788 (4.5)	-22.58 (4.5)
2006 VZ13	1.0175	6.76 (11)	-24.75 (11)
	1.0165	5.80 (16)	-24.92 (16)
	1.0159	10.3 (20)	-24.87 (20)
	1.0166	9.77 (14)	-24.9 (14)
93P	2.1451	6.01 (10)	-23.09 (10)
	2.1059	12.8 (19)	-23.05 (19)

The continuum flux is measured in the range of 6230–6270 Å of the solar-corrected spectra, where there are no known lines (Fink, 1994; Fink & Hicks, 1996). Table 3.5 lists the dust production rate derived for each comet and the ratio to the production rate of CN. The percent uncertainty in the continuum flux is calculated using the peak-to-peak noise in the wavelength range in question.

The dust-to-gas ratio stays approximately constant for each comet; however, Figure 3.10 shows an overall increase in the dust-to-gas ratio as a function of heliocentric distance. This relationship could be due to a wide range of relative abundance of refractories among the comets, or to different amounts of dust being released with the gas escaping from the surface (A'Hearn et al., 1995). The overall trend is not
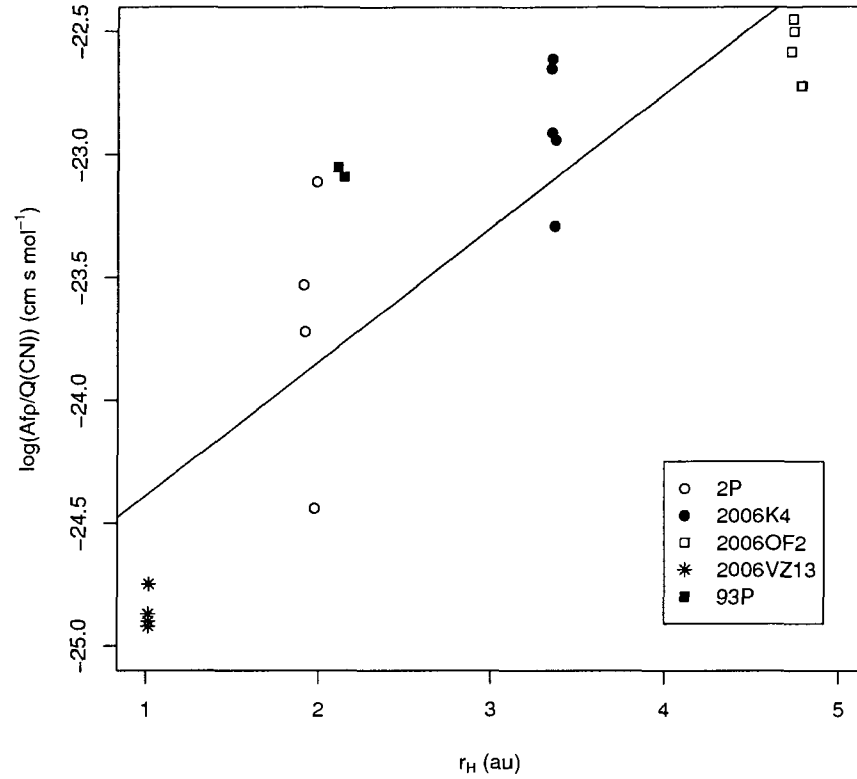
Figure 3.10: Ratio of dust production (in the range of 6231–6267 Å) to CN as a function of heliocentric distance. The slope of the best-fitting line is 0.5464 ($\sigma = 0.0767$). Uncertainties are listed in Table 3.5.

dependent on the age or dynamical class of the comets.

3.5 Conclusions

Spectroscopic observations for five comets are reported. From these spectra, the gas production rates (as in Chapter 2) and production rate ratios have been calculated. When considering the comets as a group, there is a strong correlation between the production rates of C_3 and C_2 with CN. There may also be a correlation between the production rate ratios and heliocentric distance; however, it is unclear how real this effect is due to the large uncertainties in some of the data. Within error, there seems to be a linearity of the production rate ratios, agreeing with past studies (Cochran,

1987; A'Hearn et al., 1995). Using the criteria from A'Hearn et al. (1995), comets 2P, 2006 K4, and 93P are carbon-depleted, while the classes of 2006 VZ13 and 2006 OF2 are inconclusive.

The dust production rate and the dust-to-gas ratio are also calculated for each comet. The ratio stays relatively constant for each comet, but there is an overall dependence on heliocentric distance when considering the comets as a group. There is no observed dependence of the dust-to-gas ratio on the dynamical age or class of the comets.

References

A'Hearn M., Schleicher D., Feldman P., Millis R., Thompson D. 1984. Comet Bowell 1980b, AJ 89, 579-591.

A'Hearn M., Millis R., Schleicher D., Osip, D., Birch, P., 1995. The ensemble properties of comets: Results from narrowband photometry of 85 comets, 1976-1992, Icarus 118, 223-270.

Arvesen J., Griffin R., Pearson B. Jr., 1969. Determination of extraterrestrial solar spectral irradiance from a research aircraft, Appl. Op. 8, 2215-2232.

Bus S., A'Hearn M., Schleicher D., Bowell E., 1991. Detection of CN emission from (2060) Chiron, Science 251, 774-777.

Cochran A., 1985. A re-evaluation of the Haser model scale lengths for comets, AJ 90, 2609-2614.

Cochran A., 1987. Another look at abundance correlations among comets, AJ 93, 231-238.

Cochran A., Barker E., Ramseyer T. Storrs, A. 1992. The McDonald observatory faint comet survey: Gas production in 17 comets, Icarus 98, 151-162.

Feldman P., Cochran A., Combi M., 2003. Spectroscopic investigations of fragment species in the coma, in Festou M., Keller H., Weaver H., eds, Comets II. Tuscon: The University of Arizona Press, 425-448.

Fink U., 1994. The trend of production rates with heliocentric distance for comet P/Halley, ApJ 423, 461-473.

Fink U., Hicks M., 1996. A survey of 39 comets using CCD spectroscopy, ApJ 459, 729-743.

Haser L., 1957. Distribution d'intensite dans la tete d'une comete, Bull. Soc. R. Sci. Liège 43, 740-750.

Newburn R., Spinrad H., 1989. Spectrophotometry of 25 comets: Post-Halley updates for 17 comets plus new observations for eight additional comets, AJ 97, 552-569.

Sposetti S. et al., 2006. 2006 VZ13, MPEC Circ. 2006-W03.

Storrs A., Cochran A., Barker E., 1992. Spectrophotometry of the continuum in 18 comets, Icarus 98, 163-178.

Tody, D. 1993, IRAF in the nineties, in Hanisch R.J., Brissenden R.J.V., Barnes J., eds., Astronomical Data Analysis Software and Systems II, A.S.P. Conference Ser. 52, 173-183.

Chapter 4

Searching for Main-Belt Comets Using the Canada-France-Hawaii Telescope Legacy Survey[1]

We think ourselves unhappy when a comet appears,
but the misfortune is the comet's.

- Bernard de Fontenelle, *The Plurality of Worlds*, Paris, 1686.

4.1 Introduction

Historically, asteroids and comets have been thought as two separate populations in

the Solar System. Having differing volatile fractions, a common distinction between

the two is comets display a coma, while asteroids do not. In addition, the two

---

[1]A version of this chapter has been published: Gilbert, A.M., Wiegert, P.A. 2009. Searching for main-belt comets using the Canada-France-Hawaii Telescope Legacy Survey, Icarus 201, 714-718.

populations differ dynamically. See Chapter 1 for more details about the relationships between comets and asteroids.

A standard criterion used to differentiate between a cometary or asteroidal orbit is the Tisserand parameter with respect to Jupiter,

$$T_J = \frac{a_J}{a} + 2\cos i \sqrt{\frac{a}{a_J}(1 - e^2)}, \tag{4.1}$$

where a_J is the semi-major axis of Jupiter, and a, e, and i are the semi-major axis, eccentricity, and inclination of the object, respectively. Comets typically have $T_J < 3$, while asteroids have $T_J > 3$.

Recently, surveys such as those discussed in Fernández, Jewitt, & Sheppard (2005), Jewitt (2005), and Licandro et al. (2008) have discovered a significant number of asteroids in comet-like orbits (main-belt comets, MBCs). There are also objects in asteroid-like orbits that show bursts of cometary activity (activated asteroids, AAs; i.e., 7968 = 133P/Elst-Pizzaro; Elst et al., 1996) or are associated with meteor streams (i.e., near-Earth object 3200 Phaethon; Whipple, 1983). These observations have made the boundary between comets and asteroids less obvious. Intermediate objects may be comets that are extinct, dormant, or dead. Conversely, they may be asteroids with higher volatile content.

Objects that display comet-like activity (i.e., show a coma or a tail) but are in asteroid-like orbits are known as main-belt comets (MBCs) or activated asteroids (AAs) (Hsieh & Jewitt, 2006a). These objects are most likely native to the asteroid belt (Fernández, Gallardo, & Brunini, 2002) and may be activated by a collision with a small-body (Boehnhardt et al., 1998; Toth, 2000). Hsieh & Jewitt (2005,

2006b) carry out the first survey to search for MBCs and, as of this writing, only four MBCs have been found: 133P/Elst-Pizzaro (Elst et al., 1996), P/2005 U1 (Read et al., 2005), 176P/LINEAR (Hsieh & Jewitt, 2006a), and P/2008 R1 (Jewitt, Yang & Haghighipour, 2009, discovered after the publication of this study).

In this chapter, a study is presented using the Canada-France-Hawaii Telescope (CFHT) Legacy Survey data to search for cometary activity in dynamically asteroidal bodies. This study uses images to search for MBCs, as opposed to the spectroscopic search for transition objects presented in Chapter 2.

The first (smaller) data set is subjected to stringent tests designed to detect weak activity. These objects are examined by comparing their full-width-half-maximum (FWHM) measurements and brightness profiles to those of stars of similar magnitude. If the profile of the asteroid is broader than those of the stars, it may indicate the presence of a coma. For such objects, the star profiles are subtracted from the profile of the asteroid, and an unpaired T-test is used to compare the residuals with the background to determine whether they are significantly different. A second (larger) data set is visually examined for evidence of stronger cometary activity. Using results from both methods, upper limits are derived for the number of weakly and strongly active MBCs and are compared to those expected from collisional activation of asteroids. Finally, measurements are presented of the known MBC 176P/LINEAR in the CFHT archive.

4.2   Observations and Data Reduction

All images were acquired with MegaCam on the 3.6-m CFHT in Hawaii. The images were taken as part of the Very Wide (VW) segment of the CFHT Legacy Survey (CFHTLS; Jones et al., 2006; Kavelaars et al., 2009). The asteroids forming the first data set were observed on 2004 December 15 − 16, 2005 January 16 − 17, and 2006 May 1 − 2 and 25 − 26. All observations were taken in either the g' (4145 − 5600 Å) or r' (5673 − 6892 Å) filters, with exposure times of 90 s and 110 s, respectively. The limiting magnitude for a 90% probability of a 3σ detection in the g' filter was 22.5, and 21.75 for the r' filter. The average seeing size was 1″ in both filters.

The observations for the second data set were taken on various dates between August 2003 and January 2008. The exposure times for the g' and r' filters were 70 − 110 s and 110 − 180 s, respectively, yielding comparable limiting magnitudes to the observations above.

The images were pre-processed using the Elixer pipeline (Magnier & Cuillandre, 2004). A fine astrometric correction was applied by the TERAPIX data-processing center, and the data was stored at the Canadian Astronomical Data Centre (CADC). Source Extractor (Bertin & Arnouts, 1996) and additional software designed for detecting moving bodies were used to find asteroidal objects. A more detailed explanation of the observations and data reduction process for the smaller data set are found in Wiegert et al. (2007), which used that data to investigate the size distribution of kilometer-sized main-belt asteroids (MBAs) as a function of color.

For both data sets, each field was typically observed three times on the first night,

approximately 45 minutes apart, and once the following night. This allowed for a reasonable determination of orbit parameters for main-belt objects. The observations were taken at opposition and were not selected based on their possible main-belt content. Unlike other searches for MBCs, which focus on individual objects (Chamberlin et al., 1996; Luu & Jewitt, 1990) or asteroid families (Hsieh & Jewitt, 2006a), this was a relatively unbiased survey of the main-belt. This allowed for a determination of the upper limit of MBCs expected for the whole main-belt, rather than for a sub-population. In this study, observations from the first night were utilized to search for cometary activity. When a second night of data was acquired, it was used for orbit refinement.

4.3   Data Analysis

4.3.1   Three-Level Analysis

To determine whether an asteroid showed evidence of cometary activity, three levels of analysis were chosen, each refining the number of possible MBC candidates. The investigation began with 1468 asteroids that were determined to be small-bodies in the main-belt by visual inspection of image triplets (Wiegert et al., 2007) (each of these objects were also included in the visual investigation discussed below). The analysis was limited to objects with magnitudes less than 21.5 since the wings of the seeing profiles of fainter asteroids became too noisy for reliable examination in subsequent stages. Applying this limit left 952 objects to be examined.

In the first level of analysis the FWHM measurements of the objects and stars

were compared. Each asteroid image was rotated by the angle of the direction of motion, calculated from the right ascension (RA) and declination (Dec) coordinates, such that the direction of motion lied on the horizontal axis. The FWHM was measured perpendicular to the direction of motion using IRAF's IMEXAMINE tool. The FWHM along the direction of motion of the asteroid was not measured, since the images were trailed.

All stars in the image were divided into magnitude bins (0.25-mag wide) and the median FWHM of each bin was calculated. The FWHMs of each asteroid and stars in the same magnitude bin were compared. If the FWHM of the asteroid was greater than 110% of the FWHM of the stars in two or more observations the asteroid was passed to the next analysis level. The arbitrary limit of 110% was chosen to provide a substantial number of asteroids with the highest FWHMs. Of the initial 952 asteroids, 415 passed this test.

In the second level of analysis, the brightness profile of each asteroid was compared to three stars of similar magnitude (±0.25 mag) on the same image and CCD chip. This eliminated the effect of imaging variances across the CCD. The brightness profiles were created from a 20×20 matrix of pixel counts. The counts of the columns were averaged, the background was subtracted and the columns were plotted as a function of the line number. Each profile was subsequently scaled to a height of unity.

The profiles of the asteroids were examined for interesting features (i.e., extended wings) when compared visually to the stars. Although this process was subjective, the intention was to select objects having scaled counts in the wings more than 0.05 higher than the stars. An example of a typical extended profile that passed this test is
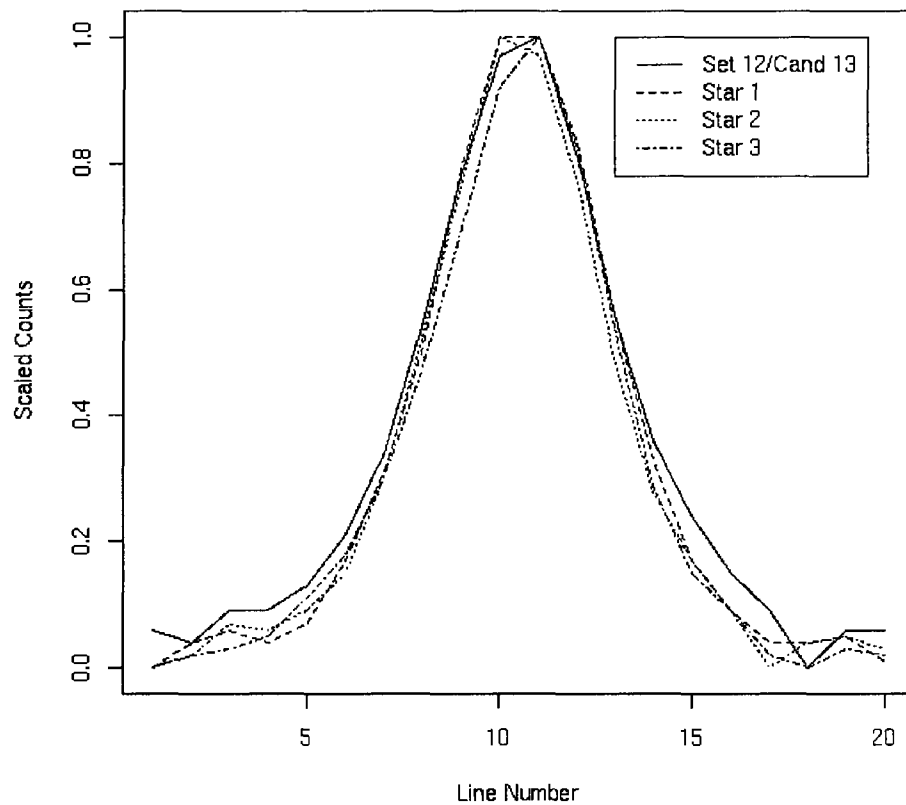
Figure 4.1: The solid black line represents the brightness profile of an asteroid in the sample, while the three dotted lines represent the profiles of three comparison stars on the same chip. The asteroid shows slightly more counts in the wings, possibly due to a coma.

shown in Fig. 4.1. There were 65 asteroids that showed a similar feature to Figure 4.1 and subsequently passed this test.

In the third level of analysis, the three star profiles were subtracted from the asteroid profile and an unpaired T-test (a method which tests the null hypothesis that the population means related to two independent, random samples from an approximately normal distribution are equal; Lichten, 1999) was used to compare the

residuals with the background noise. The T-value is given by:

$$T = \frac{\bar{x}_1 - \bar{x}_2}{s_{\bar{x}_1 - \bar{x}_2}}, \tag{4.2}$$

where

$$s_{\bar{x}_1 - \bar{x}_2} = \sqrt{\frac{(\nu_1 - 1)\sigma_1^2 + (\nu_2 - 1)\sigma_2^2}{(\nu_1 + \nu_2 - 2)} \left(\frac{1}{\nu_1} + \frac{1}{\nu_2} \right)}, \tag{4.3}$$

and $\bar{x}$, ν, and σ represent the mean, degrees of freedom, and standard deviations for the two populations, respectively.

Using this method, 14 objects had residuals that were significantly different (i.e., $T > 2$ for $\alpha = 0.05$, where α is the risk factor, or how many times out of 100 it would be expected to see a statistically significant difference even if there were not one) from the background in at least two observations.

The images of those 14 objects were examined more carefully. All of the asteroids were either overlapping or near a background object, internal reflections, or artifacts due to bright stars, thus making the object appear more extended. Therefore, no asteroids passed the final analysis level, or could be considered good MBC candidates.

4.3.2 Visual Investigation

The larger data set consisted of a total of 11615 objects which were visually inspected (as in Hsieh & Jewitt, 2006a). Some of these objects were outside the main-belt and were excluded from this analysis, leaving 11438 objects to be examined. A single known comet was found among the non-main-belt detections: active Centaur 166P/NEAT ($a = 13.88$ AU, $q = 8.56$ AU, $e = 0.383$, $i = 15.36^{\circ}$) in a distinctly active phase.

An unknown object, observed on 2007 September 14, was discovered to show cometary activity. Its on-sky motion was consistent with being an MBC, but the orbit was poorly constrained. No known comets were found in the same region using MPChecker and Jet Propulsion Laboratory (JPL) Horizons. A report to the Minor Planet Center (MPC) did not produce any response linking it to another known body, either cometary or asteroidal; therefore, these are concluded to be the discovery observations of this object, pending further information from the MPC. It remains unclear whether this object is an MBC.

Three observations of this object were taken over a 79-minute arc on one night and a fourth was taken approximately 48 hours later. The apparent magnitude varied from 21.2 to 21.6 in the r' filter. This yielded an absolute magnitude of 16.2 or a diameter, D, of $1.5 - 3.5$ km for albedos ranging from 0.05 to 0.25 (assuming the main-belt orbit calculated below). A faint, but distinct, coma/tail of approximately $10''$ in length was visible in all images (Figure 4.2).

Since this process was completed 12 months following the observations, telescopic follow-up at the time of discovery was impractical. A search of the CFHT archive found no other images that were expected to contain the comet.

The observations were taken near opposition (phase angle of 4°). The motion over 48 hours was consistent with an MBA and, assuming the usual Vaisala circular orbit (where the object is assumed to be at a particular distance and near perihelion), parameters of $a \sim 3.9$ AU and $i \sim 13^o$ were derived. However, the arc was too short to conclude this definitively, and the motion could also be fit with slightly smaller residuals (RMS $0.04''$ versus $0.14''$) by a more traditional cometary orbit with $a \sim 6$
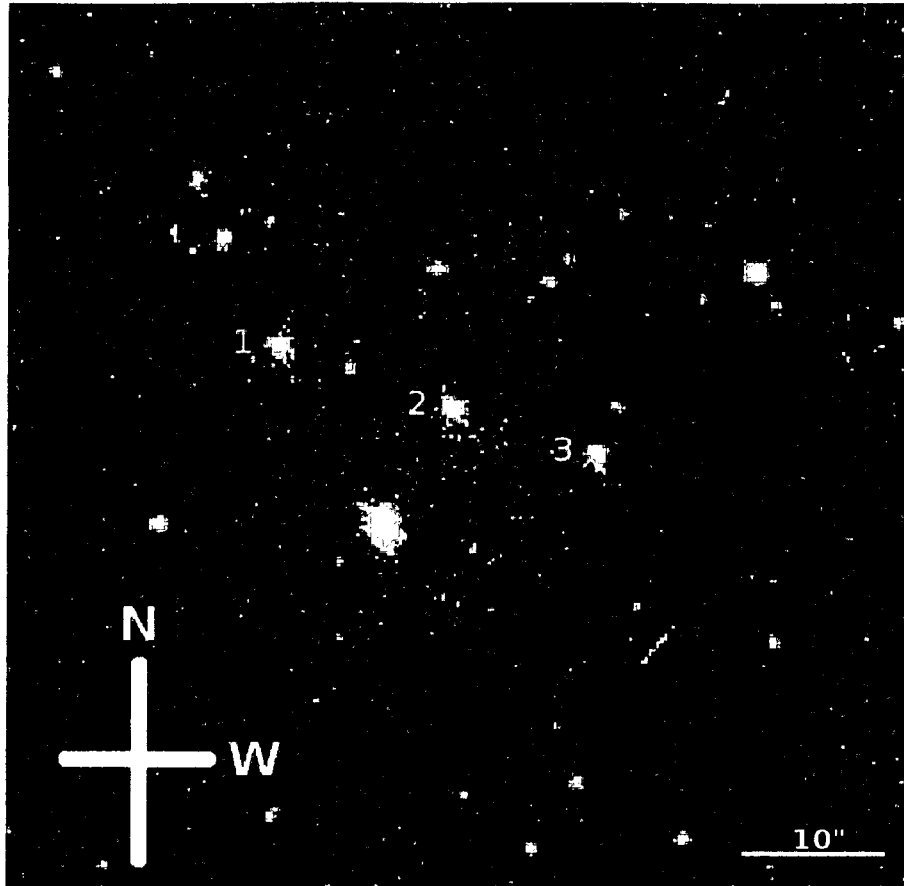
Figure 4.2: A combination of three images, taken 45 minutes apart, of the unknown comet observed 2007 September 14. The comet moves East to West in the sky. A tail of $\sim 10''$ is seen to the right (West) of the object. See Figure 4.4 for a profile of this object.

Table 4.1: Observations of the unknown comet.[a]

Obs. Date (UT)	RA	Dec	mag
2007 09 14.27098	22 51 27.56	+09 59 35.9	21.3
2007 09 14.30181	22 51 26.38	+09 59 29.6	21.2
2007 09 14.32586	22 51 25.45	+09 59 24.8	21.2
2007 09 16.29386	22 50 12.88	+09 52 33.4	21.6

[a]Each image was taken in the r' filter and had exposure times of 180 s.

AU, $e \sim 0.6$ and $q \sim 2.5$ AU. The nominal best fit cometary orbit would have passed perihelion in November 2006, about a year before the object was observed in September 2007.

Statistically, this object is more likely to be a true comet rather than an MBC because of the relative rarity of the latter (Hsieh & Jewitt, 2006a). Its true nature will only be revealed once it is recovered. The observations, as reported to the MPC, appear in Table 4.1.

The unknown comet and 166P were used to verify the three-level analysis technique. Figures 4.3 and 4.4 show the brightness profiles of 166P and the unknown comet compared to three stars, respectively. Both objects passed the three levels of analysis. No other objects in this data set show cometary activity.

4.3.3 Survey Sensitivity

The amount of cometary activity that can be observed using the CFHTLS VW data can be approximated by calculating the mass loss rate:

$$\frac{dM}{dt} = \frac{0.001 \pi \bar{\rho} a \eta r_e^2}{\phi r_h^{1/2} \Delta}, \tag{4.4}$$
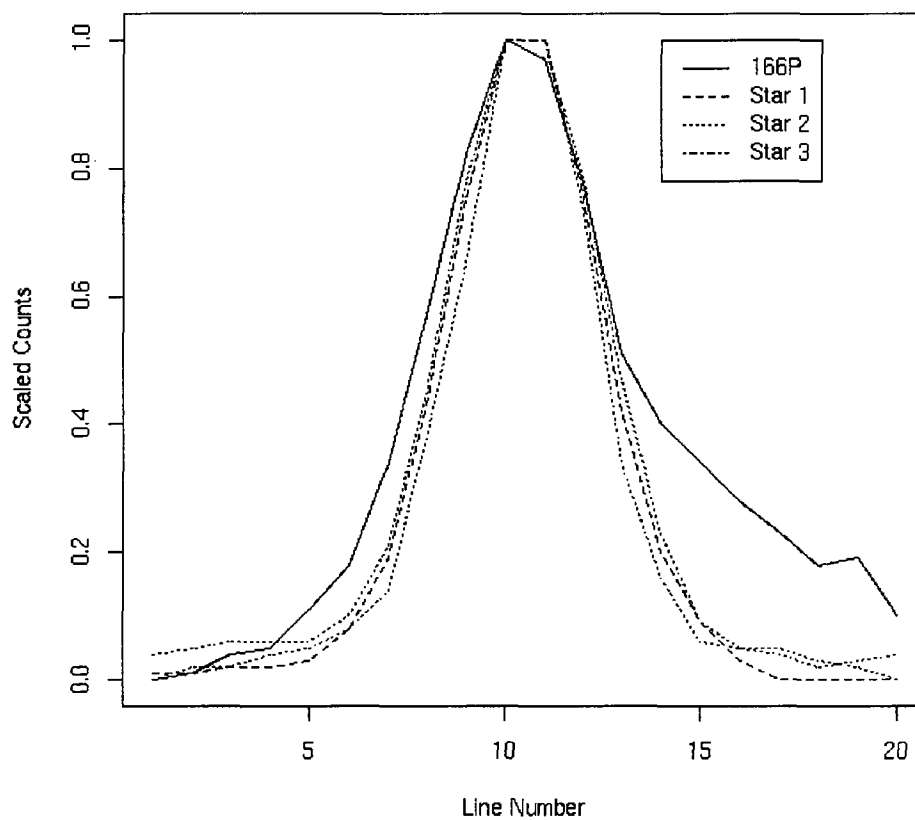
Figure 4.3: Brightness profile of 166P (solid line) and three comparison stars (dotted lines).
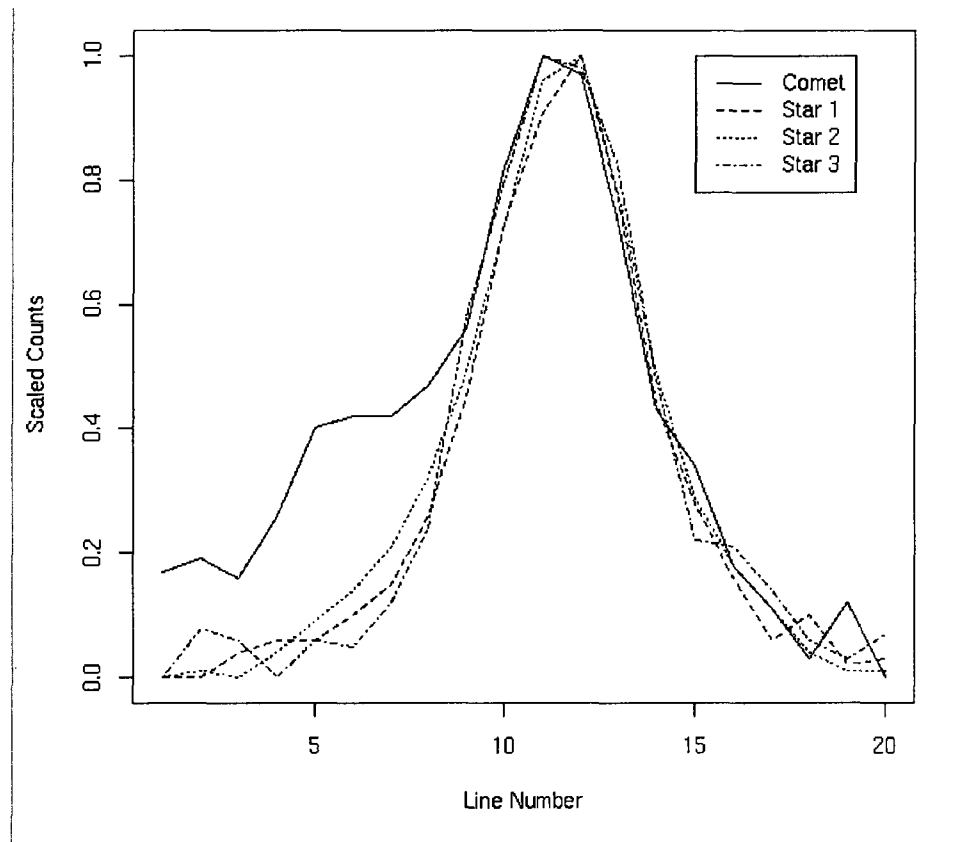
Figure 4.4: Brightness profile of the unknown comet (solid line) and three comparison stars (dotted lines).

(Luu & Jewitt, 1992) where $\rho = 1000$ kg m^{-3} is the assumed grain density, $\bar{a} = 0.5 \times 10^{-6}$ m is the assumed weighted mean grain radius, r_e is the effective radius of the object (m), ϕ is the projected radius in arcseconds, and r_H and Δ are the heliocentric and geocentric distances, respectively (AU). The quantity η is the ratio of the scattering cross sections of the coma and nucleus, where $\eta = 0$ indicating no coma and $\eta = 1$ indicating equal areas in the coma and nucleus.

To calculate η, each of the 14 objects that passed the T-test above is used. The nucleus is approximated by taking the averaged sum of the counts of the star profiles. The lower limit of an observable coma is approximated by the residuals of the star profiles subtracted from the asteroid profile. By dividing the residual counts by the star profile counts, a value for η is derived to have a range of $0.0015 - 0.017$.

The lower limit for the mass loss can then be calculated using equation 4.4. For the 14 objects used, the mass loss ranges from $0.002 - 0.045$ kg s^{-1}. Therefore, 0.002 kg s^{-1} is the lower detection limit for mass loss with the CFHTLS VW data. For comparison, mass loss rates for typical comets are 10^{1-4} kg s^{-1} (Luu & Jewitt, 1992; Jewitt, Yang & Haghighipour, 2009). Upper limits for mass loss from MBCs have been derived to be on the order of 0.01 kg s^{-1} (Luu & Jewitt, 1992; Jewitt & Hsieh, 2006; Jewitt, Yang & Haghighipour, 2009). Therefore, cometary activity from these objects would be observable using the CFHTLS VW data.

4.4 Results

4.4.1 Expected Number of Active MBCs

Two of the four known MBCs (133P/Elst-Pizzaro and 176P/LINEAR) are members of the Themis family of asteroids in the outer asteroid belt ($3.05 < a < 3.22$ AU, $0.12 < e < 0.19$, $0.69^o < i < 2.23^o$; Zappala et al., 1990). MBC P/2005 U1 is just outside this family because of its slightly higher eccentricity ($e = 0.25$), while P/2008 R1 has a higher eccentricity and inclination than the others ($e = 0.342$, $i = 15.9^o$). The unknown comet from this survey resides in the outer belt ($a \sim 3.9$ AU), though its inclination of 13° is incompatible with the Themis family.

Inside 3.2 AU, interior temperatures of asteroids are higher and may prevent the survival of ice (Hsieh & Jewitt, 2006a). Therefore, when deriving the expected numbers of MBCs, it is initially assumed that MBCs must be located in the outer belt, beyond 3.0 AU.

The objects in this study range in size down to $D \sim 1$ km and $D \sim 1.5$ km for the large and small data sets, respectively. From the cumulative size distribution given in Cheng (2004), the number of asteroids with $D \gtrsim 1$ km is $\sim 1 \times 10^6$, while for $D \gtrsim 1.5$ km it is $\sim 6 \times 10^5$. Using the de-biased number of asteroids as a function of magnitude derived by Jedicke & Metcalfe (1998), $\sim 30\%$ of asteroids with absolute magnitude less than 16 have $3.0 < a < 5.0$ AU. Extrapolating to smaller sizes, it is estimated that $\sim 30\%$ of all asteroids ($\sim 3 \times 10^5$ with $D \gtrsim 1$ km and $\sim 1.8 \times 10^5$ with $D \gtrsim 1.5$ km) are in the outer belt.

In this study, zero or one MBC candidate was found, and this number can be used

to derive upper limits of the number of expected MBCs in the main-belt. In the first data set, 216 of 952 objects fall within $3.0 < a < 5.0$ AU, which is consistent with the 30% figure stated above. Assuming MBCs only occur in the outer belt gives an upper limit of 1/216 (0.46%). The total number of asteroids expected in this region (1.8×10^5) gives an upper limit of 830 ± 86 currently weakly active MBCs, where the uncertainty is $\pm 3\sigma$ (assuming a Poisson distribution).

Using the 11438 objects from the second data set, the limit is constrained further. Although visual inspection may be insufficient to detect faint comae associated with weak activity, it is capable of determining stronger activity, as demonstrated by the detection of two moderately active comets. Of the 11438 objects, 2667 have orbits with $3.0 < a < 5.0$ AU, giving an upper limit of 0.037%, or 110 ± 31 strongly active MBCs. This limit agrees with the the $15 - 150$ range derived by Hsieh & Jewitt (2006a).

If MBCs can occur anywhere in the main-belt, the active fractions for weakly and strongly active MBCs change to 0.11% and 0.009%, respectively. Using the total number of 6×10^5 asteroids in the whole main-belt with $D \gtrsim 1.5$ km, the upper limit for weakly active MBCs becomes 630 ± 77. For strongly active MBCs, the upper limit is 87 ± 28, assuming there are 1×10^6 asteroids with $D \gtrsim 1$ km.

4.4.2 Comparison with Collisional Lifetimes

The upper limits derived for MBCs are compared with those expected from collisional activation of MBAs. The activation timescale for MBCs is unknown, but if collisional, is most likely comparable to the time between significant sub-catastrophic impacts.

This rate is approximately the destructional lifetime, which is derived by Cheng (2004) to be 10^8 years for asteroids with $D \sim 1 - 5$ km (the size range of the majority of the objects in this study). This is chosen as a first estimate of the collisional activation interval of MBCs.

Assuming there are 3×10^5 asteroids in the outer main-belt with $D \sim 1 - 5$ km, and the active lifetimes of these objects after a collision is 10^{3-4} years (Hsieh & Jewitt, 2006; Díaz & Gil-Hutton, 2008), there should be $3 - 30$ active asteroids due to collisions. This is consistent with the upper limit derived for active MBCs. This derivation assumes MBCs remain consistently active for thousands of years after activation, though observations indicate their activity is intermittent (Hsieh, 2007; see below).

4.4.3 Main-Belt Comet 176P/LINEAR

The CFHT image archive was searched for observations of three of the known MBCs (MBC P/2008 R1 was discovered after publication of this study). Only one was found, 176P/LINEAR, which was observed on 2005 June 10 and 2007 January 15. For analysis, three 60-s observations from 2005 June 10 were used, with seven and two minutes between observations, respectively. There were three 150-s observations from 2007 January 15, taken ~ 40 minutes apart.

The profiles of 176P and stars of similar magnitude were compared, and the unpaired T-test (Equation 4.2) was performed on both sets of observations. None of the images passed the T-test, indicating 176P was not active during these times.

Hsieh (2007) determined 176P was active during November and December 2005,

just after perihelion. However, it was observed to be inactive shortly before and after this, in October 2005 and February 2006. With an orbital period of 5.71 years, 176P would be expected to be inactive during June 2005, when it was approaching perihelion, and January 2007, when it was about half way between aphelion and perihelion. Figure 4.5 shows the orbital position of the active and inactive phases of 176P.

4.5 Conclusions

In this study, 952 asteroids are examined using three levels of analysis and 11438 are inspected visually. This is the largest search for MBCs using images as of this writing. This study has some advantages over the study presented in Chapter 2: using archived data from the CFHTLS greatly increases the number of objects in the sample, fainter objects are detected, and a broad sample of the asteroid population in the main-belt is obtained.

In the larger set, one unknown object is discovered to display cometary activity. Since the orbit determination for this object has large uncertainties, it is possible it is an MBC. Statistically, however, it is more likely to be a true comet. The unknown comet, as well as 166P, are used to successfully test the three-level analysis technique. No other object shows evidence of cometary activity, so there are zero or one MBC candidates in the survey.

An upper limit is derived for weakly active MBCs to be 830 ± 86 for objects with $D \gtrsim 1.5$ km and $3.0 < a < 5.0$ AU. The larger sample of visually inspected objects
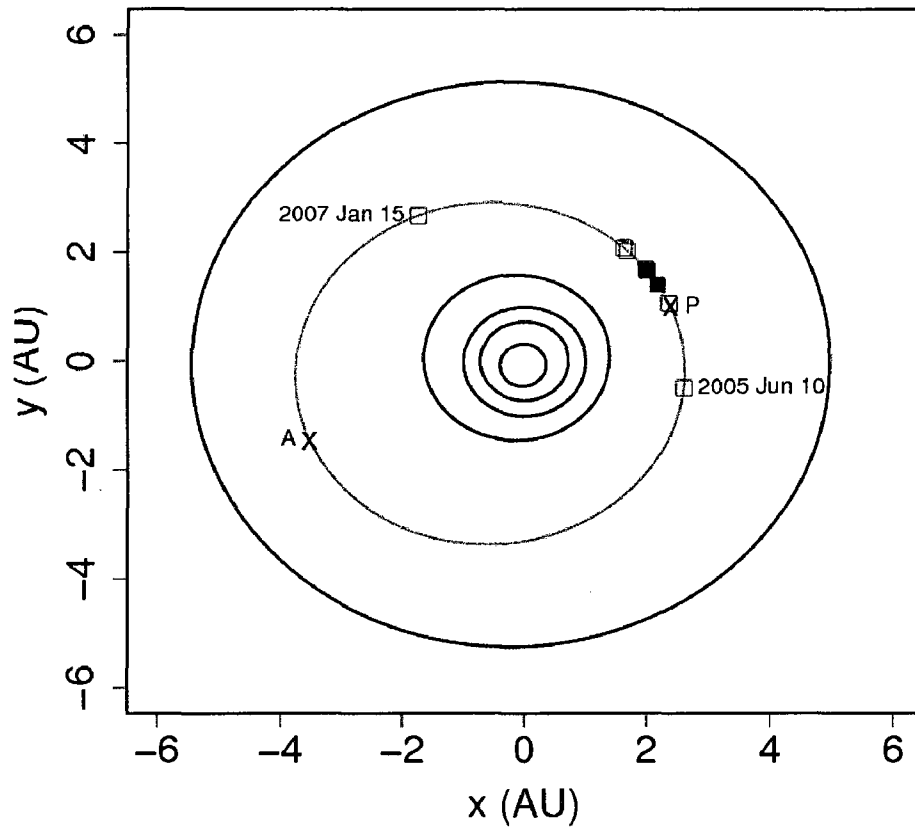
Figure 4.5: Orbital diagram of 176P showing its inactive and active phases. Orbits of Mercury, Venus, Earth, Mars, and Jupiter are shown in black, while the orbit of 176P is in gray. Aphelion (A) and perihelion (P) positions are also marked. Solid and open squares show positions where 176P is active and inactive, respectively. The two positions marked with dates are from the current study; all other positions are from Hsieh & Jewitt (2006a) or Hsieh (2007).

in the outer main-belt with $D \gtrsim 1$ km produces an upper limit of 110 ± 31 strongly active MBCs. Expanding to the whole main-belt, upper limits are 630 ± 77 and 87 ± 28 for weakly and strongly active MBCs, respectively. These agree with previous limits derived by Hsieh & Jewitt (2006a) and are in good agreement with what is expected from collisional activation of asteroids. It is concluded that the activity of MBCs is consistent with activation caused by collisions with other small main-belt objects.

References

Bertin, E., Arnouts, S. 1996. SExtractor: Software for source extraction. A&AS 117, 393-404.

Boehnhardt, H., Sekanina, Z., Fiedler, A., Rauer, H., Schulz, R., Tozzi, G. 1998. Impact-induced activity of the asteroid-comet P/1996 N2 (Elst-Pizarro): Yes or no? HiA 11A, 233.

Chamberlin, A., McFadden, L.-A., Schulz, R., Schleicher, D., Bus, S. 1996. 4015 Wilson-Harrington, 2201 Oljato, and 3200 Phaethon: Search for CN emission. Icarus 119, 173-181.

Cheng, A. 2004. Collisional evolution of the asteroid belt. Icarus 169, 357-372.

Díaz, C., Gil-Hutton, R. 2008. Collisional activation of asteroids in cometary orbits. A&A 487, 363-367.

Elst, E., Pizarro, O., Pollas, C., Ticha, J., Tichy, M., Moravec, Z., Offutt, W. Marsden, B. 1996. Comet P/1996 N2 (Elst-Pizarro). IAU Circ. 6456, 1.

Fernández, J., Gallardo, T., Brunini, A. 2002. Are there many inactive Jupiter-family comets among the near-Earth asteroid population? Icarus 159, 358-368.

Fernández, Y., Jewitt, D., Sheppard, S. 2005. Albedos of asteroids in comet-like orbits. AJ 130, 308-318.

Hsieh, H. 2007. Comets amongst the asteroids: Icy bodies in the inner Solar System. Thesis, University of Hawaii.

Hsieh, H., Jewitt, D. 2005. Search for active main-belt asteroids: The SAMBA project. BAAS 37, 631 (abstract).

Hsieh, H., Jewitt, D. 2006a. A population of comets in the main asteroid belt. Science 312, 561-563.

Hsieh, H., Jewitt, D. 2006b. Active asteroids: Mystery in the main belt. In Lazzaro, D., Ferraz-Mello, S., Fernández, J. (Eds), Asteroids, Comets, Meteors (IAU S229). Cambridge University Press, Cambridge, UK, 425-437.

Jedicke, R., Metcalfe, T. 1998. The orbital and absolute magnitude distributions of main belt asteroids. Icarus 131, 245-260.

Jewitt, D. 2005. A first look at the Damocloids. AJ 129, 530-538.

Jewitt, D., Hsieh, H. 2006. Physical observations of 2005 UD: A mini-Phaethon. AJ 132, 1624-1629.

Jewitt, D., Yang, B., Haghighipour N. 2009. Main-belt comet P/2008 R1 (Garradd). AJ 137, 4313-4321.

Jones, R., 16 colleagues 2006. The CFEPS Kuiper Belt survey: Strategy and presurvey results. Icarus 185, 508-522.

Licandro, J., Alvarez-Candal, A., de León, J., Pinilla-Alonso, N., Lazzaro, D., Campins, H. 2008. Spectral properties of asteroids in cometary orbits. A&A 481, 861-877.

Lichten, W. 1999. Data and error analysis. Prentice-Hall, New Jersey, USA.

Luu, J., Jewitt, D. 1990. Cometary activity in 2060 Chiron. AJ 100, 913-932.

Luu, J., Jewitt, D. 1992. High resolution surface brightness profiles of near-Earth asteroids. Icarus 97, 276-287.

Magnier, E., Cuillandre, J.-C. 2004. The Elixir system: Data characterization and calibration at the Canada-France-Hawaii Telescope. PASP 116, 449-464.

Read, M., Bressi, T., Gehrels, T., Scotti, J., Christensen, E. 2005. Comet P/2005 U1 (Read). IAU Circ. 8624, 1.

Toth, I., 2000. Impact-generated activity period of the asteroid 7968 Elst-Pizarro in 1996: Identification of the asteroid 427 Galene as the most probable parent body of the impactors. A&A 360, 375-380.

Whipple, F. 1983. 1983 TB and the Geminid Meteors. IAU Circ. 3881, 1.

Wiegert, P., Balam, D., Moss, A., Veillet, C., Connors, M., Shelton, I. 2007. Evidence for a color dependence in the size distribution of main-belt asteroids. AJ 133, 1609-1614.

Zappala, V., Cellino, A., Farinella, P., Knezevic, Z. 1990. Asteroid families - Identification by hierarchical clustering and reliability assessment. AJ 100, 2030-2046.

Chapter 5

Summary and Future Work

Hung by the heavens with black, yield day to night!
Comets, importing change of time and states,
Brandish your crystal tresses in the sky...

- William Shakespeare, *Henry VI*, Part I, I, i.

5.1 Thesis Summary

This thesis was based on three separate, yet related, projects which studied cometary

activity on small-bodies in our Solar System. In particular, observations were acquired

of active comets of different dynamical lifetimes and at different points in their orbit,

and two techniques were used to search for transition objects (TOs) or main-belt

comets (MBCs).

Chapter 2 described a feasibility study of a program to search for TOs using

the 1.2 m Elginfield telescope near London, Ontario. Spectroscopic observations

were acquired of 95 objects with both the Elginfield and Dominion Astrophysical

Observatory (DAO) telescopes.

This study revealed that previous observations by Chamberlin et al. (1996) could not be improved upon with the Elginfield instrument package. Due to a few challenges (notably the sensitivity function, problems with the auto-guiding, and the limited number of observable objects) this project was not feasible, and using spectroscopic observations was a difficult method to use to search for TOs. However, observations of active comets with the SBIG instrumentation proved to be useful; particularly of comet 17P, which was observed with the Elginfield telescope five days after its dramatic brightness increase.

The results from the feasibility study presented in Chapter 2 lead to the addition of two other projects to this thesis. The first, presented in Chapter 3, was a spectroscopic study of five active comets observed with the 1.5 m telescope at the Cerro-Tololo Inter-American Observatory (CTIO). Production rates of CN, C_2, and C_3, as well as production ratios with respect to CN, were derived for each comet. There was a strong correlation between the production rates of C_2 and C_3 with CN when the comets were considered as a group.

Comets 2P/Encke, 2006 K4, and 93P/Lovas I were classified as carbon-depleted based on criteria from A'Hearn et al. (1995); however, the results for 2006 VZ13 and 2006 OF2 (both new Oort cloud comets) were inconclusive. In addition, dust production rates and dust-to-gas ratios were calculated for the five comets, and there was an overall dependence on heliocentric distance when considering the comets together. There was no observed dependence of the dust-to-gas ratio on dynamical age or class of the comets.

Three comets observed with the CTIO (2006 K4, 2006 OF2, and 2006 VZ13) had never been observed spectroscopically. The observations of 2006 VZ13 were of particular interest, as it was observed during its first perihelion passage, therefore giving insight to the composition of a coma from a newly active comet. This study has been submitted for publication (Gilbert et al., 2009).

Chapter 4 presented a study which used archived images from the Canada-France-Hawaii Telescope Legacy Survey (CFHTLS) to search for MBCs. Over 950 objects were analyzed using a three-level technique to search for evidence of cometary activity, such as a coma or tail. In addition, visual inspection was completed of over 11,000 objects, making this the largest search for MBCs using images. It was also the first MBC search of its kind that did not focus on specific objects (such as Chamberlin et al. 1996; Luu & Jewitt 1990) or asteroid families (i.e., Hsieh & Jewitt 2006). This allowed for a determination of an MBC upper limit for the whole main-belt, rather than for a sub-population.

Two objects were found to display cometary activity: 166P (a known active Centaur) and another unknown comet. Unfortunately, because of the short arc of this second object, the orbit determination was not well constrained. Searches for this object in other archives yielded no results, and it remains unclear whether it is an MBC. No other object showed evidence of a coma or tail.

The CFHTLS study agreed with, and expanded on, previously derived upper limits for the number of expected MBCs calculated by Hsieh & Jewitt (2006) . Upper limits of the number of weakly and strongly active MBCs in the main-belt were derived to be 630 ± 77 and 87 ± 28, respectively. The three-level technique is a seemingly simple,

yet effective and sensitive way to search for cometary activity. Visual investigation also proves to be useful, although it may not be as sensitive. This study has been published (Gilbert & Wiegert, 2009).

5.2 Future Work

We are far from understanding the composition of active comets or just about everything about the new class of objects known as TOs or MBCs. There are many observations, models, and theories that can be improved in order to increase our knowledge of the different classes of comets and how they evolve both physically and dynamically. A small sample of ideas for future work, which are related to the three projects presented in this thesis, is discussed here.

5.2.1 Elginfield Instruments

Although the Elginfield project was not deemed feasible, observations could be continued to attempt to lower the upper limits of the production rates (i.e., by taking longer exposures). However, because of the large drop in the system efficiency at about 4000 Å, it is suggested to search for other emission lines besides CN at 3880 Å. The SBIG instrument package could also be used to acquire spectroscopic observations of active comets (and other astronomical objects in general).

5.2.2 Active Comets

Spectroscopic observations of additional active comets are needed in order to create a catalogue of cometary composition, and to confirm or add to the classes given

by A'Hearn et al. (1995). In addition, observations of active comets at different points along their orbit, and also through multiple apparitions, will allow for a better understanding of how the gas and dust production of comets evolve with distance from the Sun and/or with the dynamical lifetime of the comet. Observing comets as they dynamically evolve would also be beneficial in order to shed additional light on the fading problem, and perhaps how, or if, they become TOs.

5.2.3 Main-Belt Comet Observations

More observational surveys to search for MBCs are needed in order to further constrain the upper limit on the number of MBCs expected in the main-belt. These surveys should concentrate on observing a large number of main-belt objects throughout the population. For example, using image or spectrum archives would be an excellent source of observations for this type of study, particularly large survey programs like the CFHTLS. Monitoring programs of good TO candidates (i.e., objects classified as asteroids, but with comet-like orbits) would also be beneficial, since it is not well understood when these objects may turn on or off. Finally, additional image and spectroscopic observations of known MBCs throughout their orbit will greatly increase our knowledge of these objects.

Active comets have been studied for centuries, but the topic of TOs and MBCs is relatively new in the area of planetary science. Understanding the composition, activity, and dynamics of these objects will help us understand the physical and dynamical evolution of comets, their connection to asteroids, and the environment and formation of the early Solar System.

References

A'Hearn M., Millis R., Schleicher D., Osip, D., Birch, P., 1995. The ensemble properties of comets: Results from narrowband photometry of 85 comets. 1976-1992, Icarus 118, 223-270.

Chamberlin, A., McFadden, L.-A., Schulz, R., Schleicher, D., Bus, S. 1996. 4015 Wilson-Harrington, 2201 Oljato, and 3200 Phaethon: Search for CN emission. Icarus 119, 173-181.

Gilbert, A., Wiegert, P. 2009. Searching for main-belt comets using the Canada-France-Hawaii Telescope Legacy Survey. Icarus 201, 714-718.

Gilbert, A., Wiegert, P., Unda-Sanzana, E., Vaduvescu, O. 2009. Spectroscopic observations of new Oort cloud comet 2006 VZ13 and four other comets. Submitted to MNRAS.

Hsieh, H., Jewitt, D. 2006. A population of comets in the main asteroid belt. Science 312, 561-563.

Luu, J., Jewitt, D. 1990. Cometary activity in 2060 Chiron. AJ 100, 913-932.

Appendix A

Production Rate Derivation

A.1 Our Model

To calculate the gas production rate for a given molecule, it is assumed in this thesis that the molecule, once released from the nucleus, travels the total distance of its scale length before being destroyed (l, which gives the radius of the cloud, r_o; see below). First, consider a point source of N molecules with a luminosity per molecule $g = L/N$ (i.e., the fluorescence efficiency, or g-factor; erg s^{-1} molecule^{-1}). The energy (erg) received from a comet at geocentric distance Δ (cm) by a telescope of aperture, A (cm^2), during an exposure of time T (s) is

$$E = \frac{AgNT}{4\pi\Delta^2}.$$
(A.1)

The brightness (or flux - erg cm^{-2} s^{-1}) per unit area per second received by the telescope is

$$F = \frac{E}{AT} = \frac{gN}{4\pi\Delta^2},$$
(A.2)

and the number of photons received is

$$N_p = \frac{A}{4\pi\Delta^2} \frac{gNT}{h\nu},$$
(A.3)

where h is Planck's constant $(6.6262 \times 10^{-27}$ erg s$^{-1})$ and ν is the frequency of the photon (Hz, or s^{-1}).

Now, instead of a point source, consider a cylinder of gas of column density N_c (molecules cm^{-2}), which subtends a solid angle Ω (sr) when seen from Earth. The column density is given by

$$N_c = \frac{N}{\Omega\Delta^2}.$$
(A.4)

Using Equation A.2 for flux above gives

$$N_c = \frac{4\pi F}{g\Omega}.$$
(A.5)

Now, instead of a simple cylinder, consider an expanding spherical cloud of gas being produced at a rate of Q molecules s^{-1}. Assuming the molecule has a lifetime τ (s) against photodissociation, and an expansion velocity of the observed molecule, v_e (cm s^{-1}), the radius of the cloud (or scale length, cm) is

$$r_o = v_e\tau,$$
(A.6)

and the total number of molecules in the cloud is

$$N = Q\tau.$$
(A.7)

Using Equation A.2 for flux above gives

$$F = \frac{gQ\tau}{4\pi\Delta^2},$$
(A.8)
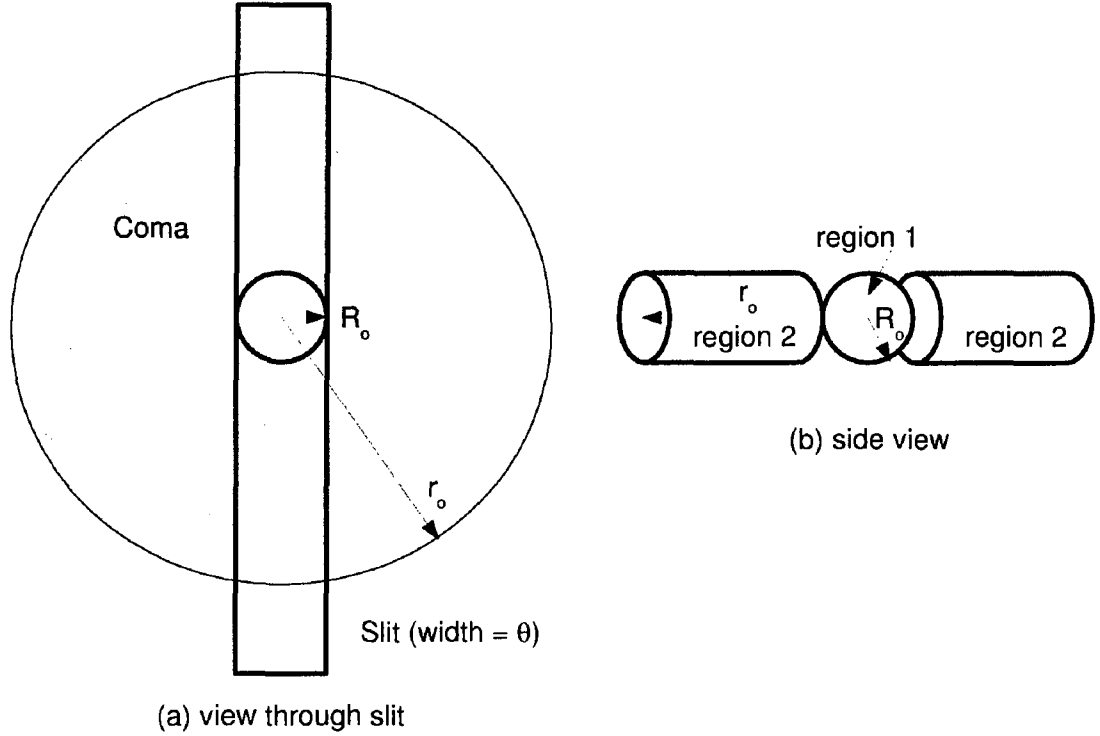
Figure A.1: Schematic of the geometry for deriving the gas production rate: (a) view of a cometary coma of radius r_o as seen through the slit of width θ (R_o is the radius of the coma that can fit in the slit); (b) side view through the coma, approximated by two cylinders and a central sphere.

or, solving for Q,

$$Q = \frac{4\pi\Delta^2 F}{g\tau}.$$
(A.9)

In terms of N_p, this becomes

$$Q = \frac{4\pi\Delta^2 N_p h\nu}{g\tau}.$$
(A.10)

The above derivation assumes all photons from the coma are observed. However, for this thesis, we consider the case where the amount of the cometary coma observed is set by the slit size. We will ignore any light coming above or below the spherical region that fits in the slit (Figure A.1), because it is only a small contribution.

For simplicity, this case can be approximated by the regions shown in Figure A.1(b).

An equation for the flux received from the central sphere (region 1) can be derived as follows: The radius of the object that can fit into the slit of width θ (rad) can be found from

$$\tan\left(\frac{\theta}{2}\right) = \frac{R_o}{\Delta}, \tag{A.11}$$

where R_o (cm) is the radius of the slit at the distance of the comet. Using the small angle approximation (i.e., $\tan(x) \simeq x$),

$$R_o = \frac{\theta}{2}\Delta. \tag{A.12}$$

The number of molecules in the central spherical region can be found by intergrating the number density of particles in each spherical shell, $n(r)$, over the volume of the sphere:

$$N_1 = \int_0^{R_o} n(r)dV = \int_0^{R_o} \frac{Q}{4\pi R^2 v_e} 4\pi R^2 dr = \frac{QR_o}{v_e}, \tag{A.13}$$

Using Equation A.12, this becomes

$$N_1 = \frac{Q\theta\Delta}{2v_e}. \tag{A.14}$$

The number of photons received at a telescope of aperture A, using equations above, is

$$N_{p,1} = \frac{gNAT}{8\pi\Delta^2 h\nu}. \tag{A.15}$$

Substituting in Equation A.14 gives

$$N_{p,1} = \frac{gAT}{8\pi\Delta^2 h\nu} \frac{Q\theta\Delta}{v_e}. \tag{A.16}$$

Solving this expression for Q,

$$Q_1 = \frac{8\pi\Delta h\nu N_p v_e}{gAT\theta}. \tag{A.17}$$

The flux, or brightness, received at the telescope is given by

$$F_1 = \frac{N_p h\nu}{AT}.$$ (A.18)

Using Equation A.17 for Q above gives

$$F_1 = \frac{Qg\theta}{8\pi\Delta v_e}.$$ (A.19)

An expression for the flux received from the cylinders in front and behind the central sphere [region 2 in Figure A.1(b)] is derived as follows: The number of molecules in the two cylinders can be found by integrating the number density, $n(r)$, of particles in each slice (disk) of radius R_o over the volume of the cylinders:

$$N_2 = 2\int_{R_o}^{r_o} n(r)dV = 2\int_{R_o}^{r_o} \frac{Q}{4\pi r^2 v_e}\pi R_o^2 dr = \frac{2QR_o^2}{4v_e}\int_{R_o}^{r_o}\frac{dr}{r^2} = \frac{QR_o^2}{2v_e}\left(\frac{1}{R_o} - \frac{1}{r_o}\right),$$ (A.20)

where r_o (cm) is the radius of the whole coma, which is given by the scale length of the molecule, l (cm). The scale length $l \gg R_o$, and $R_o = (\theta\Delta)/2$. This gives

$$N_2 \approx \frac{QR_o^2}{2v_e}\frac{1}{R_o} = \frac{Q\theta\Delta}{4v_e}.$$ (A.21)

The flux received from the cylinders is

$$F_2 = \frac{Ng}{4\pi\Delta^2} = \frac{Q\theta g}{16\pi\Delta v_e}.$$ (A.22)

Combining Equations A.19 and A.22 gives the total flux received:

$$F_{total} = \frac{3Q\theta g}{16\pi\Delta v_e}.$$ (A.23)

Solving for Q, the final expression for the gas production rate is

$$Q_{total} = \frac{16\pi\Delta v_e F}{3g\theta}.$$ (A.24)

Table A.1: Example parameters from the CN molecule from observations of comet 2006 VZ13, observed 6 August 2007.

Parameter (units)	Value	Description
v_e (cm/s)	1×10^5	velocity of observed molecule
Δ (AU)	1.0207	geocentric distance
F (erg cm^{-2} s^{-1})	2.58×10^{-12}	flux
g (erg s^{-1} mol^{-1})	3.57×10^{-13}	g-factor for CN at Δ
R_o (cm)	7.4×10^7	radius of aperture at comet
l_{CN} (cm)	2.1×10^{10}	scale length of CN
θ (rad)	4.848×10^{-6}	slit width

Table A.1 lists parameters for the CN molecule from observations of comet 2006 VZ13, when observed on 2007 August 6 (see Tables 3.2 and 3.4 in Chapter 3). Using Equation A.24, the production rate for CN is $Q_{CN} = 3.81 \times 10^{25}$ molecules s^{-1}.

A.2   Haser Model

The Haser model also uses the same geometry as pictured in Figure A.1, but instead assumes the particles decay exponentially. If we assume the scale length of the daughter molecule is larger than that of the parent molecule (which is the case for the three molecules discussed in this thesis - CN, C_2, and C_3), then the number density of particles in each shell/disk is

$$n(r) = \frac{Qe^{-r/l}}{4\pi r^2 v_e},$$

$$(A.25)$$

Therefore, the number of molecules in the spherical region in Figure A.1 (region 1) is given by

$$N_1 = \int_0^{R_o} n(r)dV = \int_0^{R_o} \frac{Qe^{-r/l}}{4\pi R^2 v_e} 4\pi R^2 dr = \frac{Ql}{v_e}(1 - e^{-R_o/l}),$$

$$(A.26)$$

and the number of molecules in the two cylindrical regions (region 2) is

$$N_2 = 2 \int_{R_o}^{\infty} n(r) dV = 2 \int_{R_o}^{\infty} \frac{Qe^{-r/l}}{4\pi r^2 v_e} \pi R_o^2 dr = \frac{QR_o^2}{2v_e} \int_{R_o}^{\infty} \frac{e^{-r/l}}{r^2} dr. \tag{A.27}$$

The solution of the integral is

$$\int_{R_o}^{\infty} \frac{e^{-r/l}}{r^2} dr = \left[\frac{-\text{Ei}(-r/l)}{r} - \frac{e^{-r/l}}{r} \right]_{R_o}^{\infty}, \tag{A.28}$$

where $\text{Ei}(x)$ is the exponential integral, given by

$$\text{Ei}(x) = - \int_{-x}^{\infty} \frac{e^{-t}}{t} dt. \tag{A.29}$$

This integral can be solved numerically. Using Equations A.26 - A.28, the total number of molecules in the regions given by Figure A.1 is

$$N_{total} = \frac{Q}{v_e} \left[l(1 - e^{-R_o/l}) + \frac{R_o^2}{2} \left(\frac{-\text{Ei}(-r/l)}{l} - \frac{e^{-r/l}}{r} \right)_{R_o}^{\infty} \right]. \tag{A.30}$$

As mentioned at the beginning of this appendix, the g-factor is luminosity per molecule. Therefore,

$$N = \frac{L}{g} = \frac{4\pi \Delta^2 F}{g}. \tag{A.31}$$

Setting Equations A.30 and A.31 equal to each other, let X denote the value in square brackets in Equation A.30, and solving for Q gives

$$Q_{total} = \frac{4\pi \Delta^2 v_e F}{gX}. \tag{A.32}$$

Using the values in Table A.1, the production rate for CN using the Haser model is 2.87×10^{25} molecules s^{-1}. This value was derived using our model to be 3.81×10^{25} molecules s^{-1}, which is about a 25% difference. The uncertainties in the CN production rate derived for comet 2006 VZ13 in Chapter 3 (see Table 3.4) were

between $10 - 16\%$, and were higher for the other comets. Therefore, although our

model is based on simple approximations, it is reasonable based on the uncertainties

involved in the production rate calculation.

Appendix B

Elginfield and DAO Observations

Notes:

1. Exp. (s) refers to total exposure time of co-added observations.

2. All production rates are upper limits except for comet 17P (where the number in brackets is percent error).

3. A 'T'designation for magnitude refers to the total magnitude of a comet; all magnitudes are from JPL Horizons.

4. Objects that have more than one observation per night (denoted by 'a', 'b', etc.) indicates there was more than one object visible in the field of view.

Table B.1: Observational geometry and production rates for objects observed using the Elginfield telescope.

Date (UT)	Object	Exp. (s)	Δ (AU)	r_H (AU)	V (mag)	log Q (mol s^{-1})			
						CN	C_3	C_2 ($\Delta v = 1$)	C_2 ($\Delta v = 0$)
2006 June 18	2	90	2.532	3.291	9.55	–	–	–	27.90
2006 July 03	2	20	2.525	3.308	9.54	–	–	–	28.60
	660	120	1.325	2.266	11.94	–	–	–	27.06
2006 July 24	25	60	1.231	1.838	10.90	–	–	–	27.27
	11405	300	0.164	1.076	13.51	–	–	–	25.25
2006 Aug 05	102P	480	1.921	2.036	19.19(T)	–	–	–	26.69
	415	360	1.642	2.544	13.08	–	–	–	27.01
	4420	300	0.896	1.862	14.10	–	–	–	26.37
	75	480	0.913	1.871	10.86	–	–	–	26.88
2006 Aug 12	132	480	2.749	3.006	14.78	–	–	–	27.44
	14211	960	0.774	1.710	15.29	–	–	–	26.11
	217	480	1.722	2.174	13.88	–	–	–	26.87
	879	180	1.577	2.141	15.74	–	–	–	26.79
2006 Aug 30	2651	180	1.403	2.084	14.59	–	–	–	27.00
	415	480	1.461	2.463	12.35	–	–	–	27.07
	75	480	0.851	1.859	10.19	–	–	–	27.16
	7604	300	0.985	1.978	15.70	–	–	–	26.53
	HR30	480	1.142	2.066	16.72(T)	–	–	–	26.50
2006 Oct 02	101679	1020	0.811	1.738	15.49	–	–	–	25.94
	102P	420	1.583	2.199	19.03(T)	–	–	–	26.55
	129	420	2.051	3.018	11.26	–	–	–	27.81
	180	420	2.123	3.033	14.98	–	–	–	26.99
	2006RZ	300	0.040	1.027	15.23	–	–	–	24.39
	211	420	1.776	2.767	11.62	–	–	–	26.92

Table B.1: Elginfield observations cont.

Date (UT)	Object	Exp. (s)	Δ (AU)	r_H (AU)	V (mag)	CN	C_3	C_2 (Δv = 1)	C_2 (Δv = 0)
								log Q (mol s^{-1})	
	29P	420	5.295	5.845	14.39(T)	–	–	–	27.96
	389	420	2.102	2.724	12.32	–	–	–	26.79
	409	420	1.711	2.691	11.04	–	–	–	27.53
	68	420	1.309	2.270	9.86	–	–	–	27.85
	73PE	720	0.809	1.775	13.68(T)	–	–	–	26.16
	74a	420	1.423	2.166	12.01	–	–	–	26.51
	74b	420	1.423	2.166	12.01	–	–	–	26.71
2006 Oct 06	1980	1200	0.456	1.115	14.71	–	–	–	25.00
	1998UO1	1500	0.235	1.186	15.24	–	–	–	25.09
	2001CB21	1680	0.546	1.008	14.87	–	–	–	25.60
	393	600	3.505	3.498	14.66	–	–	–	27.12
	880a	900	1.428	2.157	14.98	–	–	–	26.59
	880b	900	1.428	2.157	14.98	–	–	–	26.52
2006 Oct 08	1866	900	0.837	1.092	14.97	–	–	25.49	25.40
	1980	900	0.449	1.119	14.66	–	–	25.28	25.20
	344	1800	3.512	3.414	14.44	–	–	26.92	26.61
	36	900	2.248	2.109	13.03	–	–	26.52	26.43
	3682	900	1.603	2.074	15.35	–	–	26.52	26.22
	393	600	3.480	3.502	14.65	–	–	27.49	27.47
	7496	900	1.386	2.043	15.54	–	–	26.47	26.43
2006 Nov 25	132	900	1.769	2.616	13.32	–	–	26.84	26.61
	1550	600	0.885	1.861	13.39	–	–	26.33	26.11
	1980	600	0.339	1.300	13.13	–	–	25.85	25.48
	2006M4	780	1.492	1.311	12.68(T)	–	–	26.01	26.07
	2651	600	1.180	2.003	13.98	–	–	26.31	26.11
	33	600	3.729	3.712	14.92	–	–	27.30	27.17

Table B.1: Elginfield observations cont.

Date (UT)	Object	Exp. (s)	Δ (AU)	r_H (AU)	V (mag)	CN	C_3	C_2 ($\Delta v = 1$)	C_2 ($\Delta v = 0$)
								log Q (mol s^{-1})	
	344	480	2.843	3.411	13.92	—	—	27.32	27.11
	3682	600	1.306	2.223	14.55	—	—	26.65	26.28
	393	600	2.895	3.574	14.16	—	—	27.46	27.02
	415	600	1.863	2.196	13.47	—	—	26.96	26.68
	5143	900	0.462	1.350	14.33	—	—	25.53	25.30
	7496	600	1.124	2.087	14.51	—	—	26.35	26.18
	75	300	1.487	1.940	12.43	—	—	26.60	26.68
	880	600	1.304	2.281	14.22	—	—	26.75	26.29
	3	300	3.362	2.844	10.92	—	—	27.45	27.39
2007 Feb 24	1362	900	2.125	2.708	15.95	27.97	26.84	26.62	26.48
	324	900	2.821	3.587	12.60	28.29	27.95	27.10	26.94
	36	1800	1.633	2.542	12.24	27.91	26.88	26.63	26.56
	393a	900	3.046	3.667	14.34	28.62	28.23	27.36	27.09
	393b	1500	3.046	3.667	14.34	28.49	27.31	27.13	26.92
	HR30	900	0.916	1.433	13.85(T)	27.25	26.80	26.11	25.89
2007 Mar 12	132	900	2.457	2.148	13.98	28.35	27.39	26.83	26.68
	20	900	1.334	2.131	9.66	27.52	26.50	26.48	26.41
	324	900	2.681	3.589	12.32	28.52	27.66	27.27	27.29
	344	1200	2.812	3.338	13.89	28.19	27.05	27.67	26.70
	747	900	2.974	3.790	13.54	28.63	27.53	27.23	27.10
2007 Mar 24	132	900	2.614	2.095	13.93	27.74	27.15	26.64	26.43
	344	900	2.955	3.324	14.02	28.49	27.82	27.75	27.02
	36	900	1.935	2.634	12.93	27.90	27.12	27.05	26.54
	372	900	1.964	2.532	11.86	27.87	27.00	27.21	26.55
	419	900	2.981	3.187	12.96	28.67	27.60	27.47	26.85
	41	900	3.041	3.015	14.24	28.11	27.17	27.06	27.00

Table B.1: Elginfield observations cont.

Date (UT)	Object	Exp. (s)	Δ (AU)	r_H (AU)	V (mag)	log Q (mol s^{-1})			
						CN	C_3	C_2 ($\Delta v = 1$)	C_2 ($\Delta v = 0$)
	696	900	2.421	3.084	14.22	28.19	27.22	27.64	26.67
	965	900	1.859	2.510	14.15	27.84	26.99	26.82	26.28
	97	900	1.875	2.168	11.91	27.63	26.67	27.09	26.52
2007 Apr 29	130	1200	3.485	2.745	12.67	28.47	26.95	26.97	26.73
	324	814.9	3.584	2.694	12.38	28.70	27.51	27.60	27.19
	372	1800	2.613	4.494	12.49	27.75	27.75	27.14	27.17
	3	600	3.162	2.219	10.00	28.08	27.28	27.30	27.17
	516	562.02	1.986	1.090	10.76	27.50	26.58	26.34	26.33
	599	1495.6	3.386	2.568	14.18	28.01	26.97	27.13	26.67
	7304	784.5	1.509	0.542	13.79	26.47	25.50	25.38	25.39
	747	1800	3.887	2.970	13.50	27.88	26.97	26.88	26.71
	796	790.7	3.189	2.183	13.47	28.14	27.18	27.11	26.64
2007 Apr 30	344	1800	3.274	3.412	14.31	28.46	27.03	27.18	27.03
2007 May 13	225	1200	2.526	2.023	13.34	27.86	26.84	26.91	26.66
	225b	600	2.526	2.023	13.34	28.37	27.34	28.14	27.07
	323	1800	3.099	2.306	14.78	28.35	26.98	26.87	27.21
	324	1361.75	3.579	2.815	12.62	28.33	27.68	27.44	27.34
	50	1800	3.147	2.138	13.55	27.86	27.26	26.97	27.00
	796	600	3.159	2.178	13.75	28.06	27.19	27.20	27.02
	3	300	3.184	2.340	10.26	28.29	27.86	27.50	27.51
2007 May 14	1021	1200	3.353	2.448	14.16	28.15	27.48	27.10	27.05
	36	1800	2.796	2.724	13.90	28.26	27.14	27.04	26.80
	516a	600	1.969	1.167	11.06	27.74	27.01	26.83	26.45
	516b	900	1.969	1.167	11.06	27.80	26.82	26.59	26.52
	7304	1800	1.504	0.548	13.91	26.58	25.60	25.50	25.13

Table B.1: Elginfield observations cont.

Date (UT)	Object	Exp. (s)	Δ (AU)	r_H (AU)	V (mag)	CN	C_3	C_2 ($\Delta v = 1$)	C_2 ($\Delta v = 0$)
							log Q (mol s^{-1})		
	747	1200	3.885	3.094	13.71	28.55	27.83	28.16	27.22
2007 May 23	3	1200	3.198	2.452	10.44	28.61	27.53	27.31	27.81
	324	263.84	3.575	2.924	12.77	28.93	27.92	27.64	27.51
2007 May 28	225	1130	1.871	2.513	13.11	28.15	27.29	26.99	26.96
	372	995.5	2.928	2.683	12.68	29.54	28.65	28.56	28.61
	391	1800	1.513	1.828	13.71	27.87	26.98	26.55	26.34
	50	900	2.413	3.118	13.84	29.08	27.48	27.69	27.12
	747	600	3.251	3.903	13.95	28.85	27.69	27.67	27.55
2007 June 30	1021	1800	3.276	2.355	14.02	28.00	27.02	26.82	26.75
	102	900	2.009	1.812	13.30	27.58	26.81	26.73	27.01
	391	900	1.733	1.201	13.13	27.20	26.09	25.99	25.62
2007 July 01	183	900	2.375	1.764	13.88	27.80	26.97	26.75	26.53
	225	1800	2.492	1.626	12.60	27.44	26.64	26.53	26.45
	3	1200	3.250	3.002	11.03	28.34	27.82	27.39	27.03
2007 July 07	2109	600	2.254	1.260	14.71	27.28	26.72	26.24	26.17
	391	1200	1.715	1.141	13.00	28.01	26.03	25.85	25.85
	747	1200	3.947	3.824	14.37	28.57	27.75	27.51	27.05
	3	300	3.257	3.093	11.10	28.62	27.85	28.00	27.45
2007 July 12	137	600	2.243	1.485	11.48	28.90	27.27	26.76	26.60
	194	1200	2.009	1.155	10.41	27.18	26.60	26.09	26.00
	702	300	3.130	2.225	11.99	29.34	28.13	27.27	27.16
	80	600	2.010	1.032	10.25	28.45	27.33	26.64	26.29
	85	600	2.318	1.453	10.96	28.84	27.01	26.79	26.69
2007 Aug 27	115	600	2.126	1.136	9.91	27.59	26.90	26.63	26.94
	137	1200	2.435	1.642	11.99	27.02	26.70	26.50	26.42
	391	1200	1.626	0.778	11.86	26.84	25.87	25.55	25.49

Table B.1: Elginfield observations cont.

Date (UT)	Object	Exp. (s)	Δ (AU)	r_H (AU)	V (mag)	CN	log Q (mol s^{-1})		
							C_3	C_2 ($\Delta v = 1$)	C_2 ($\Delta v = 0$)
	654	1800	2.786	1.827	12.62	28.08	26.65	26.61	26.53
	85	900	2.245	1.820	11.68	28.12	27.03	26.72	26.76
2007 Oct 29	115	300	2.014	1.328	10.79	28.03	26.95	26.80	26.56
	176	600	2.742	2.146	12.71	28.08	27.04	27.33	26.79
	391	600	1.632	0.740	11.60	26.91	25.84	25.76	25.68
	4954	600	0.303	1.142	12.26	26.46	25.38	25.51	25.42
	654	1800	2.716	2.294	13.52	27.93	26.73	26.72	26.41
	98	1800	2.807	1.841	12.72	27.67	26.76	26.58	26.42
	17P	3360	2.456	1.626	2.7(T)	27.67 (44)	26.60 (21)	26.77 (17)	27.08 (29)

Table B.2: Observational geometry and production rates for objects observed using the DAO telescope.

Date (UT)	Object	Exp. (s)	Δ (AU)	r_H (AU)	V (mag)	log Q (mol s^{-1})			
						CN	C_3	C_2 ($\Delta v = 1$)	C_2 ($\Delta v = 0$)
2007 Apr 15	130	2100	2.903	3.506	12.87	26.18	25.85	25.51	25.11
	33	3000	3.166	3.825	14.55	26.11	26.26	25.45	25.40
	36	1800	2.257	2.705	13.42	25.58	25.46	25.10	24.93
	372	900	2.283	2.581	12.28	25.95	25.75	25.44	25.18
	3	300	2.150	3.139	9.75	26.46	26.47	26.14	26.23
	599	1800	2.488	3.408	13.98	25.46	25.26	25.25	24.87
	7304	3600	0.563	1.524	13.89	24.28	23.90	23.75	23.79
	747	1500	2.905	3.845	13.36	25.72	25.54	25.77	25.29
	952	1800	2.708	3.711	14.33	26.02	25.74	25.30	25.82
2007 Apr 17	28	1200	1.636	3.619	10.70	25.34	25.37	25.04	25.38
	455	1800	2.819	3.427	14.61	25.81	25.55	25.28	25.55
	97	1200	2.202	2.226	12.28	25.27	25.59	25.15	24.79
2007 Apr 18	1278	562	1.867	2.786	15.04	25.71	26.20	25.41	24.97
	164	3600	2.876	3.502	14.71	25.99	25.63	25.89	25.56
	273	871	1.274	2.211	13.24	25.48	25.10	24.94	24.48
	323	1800	2.209	3.094	14.57	25.32	25.52	25.09	24.79
	7304	3600	0.556	1.520	13.85	24.00	23.90	23.83	23.16
2007 Aug 14	102	3000	1.993	1.357	12.58	26.29	26.37	26.70	26.73
	1565	3600	1.688	0.846	14.30	24.25	23.80	24.18	23.86
	225	3600	2.486	1.621	12.58	24.97	25.26	25.09	25.33
	391	3600	1.642	0.856	12.18	25.07	25.43	25.44	25.53
2007 Aug 15	1222	3600	2.175	1.333	13.58	24.60	24.49	24.86	24.60
	12	1800	1.944	1.235	10.10	26.03	26.33	25.57	25.73
	1585	3600	2.696	1.686	14.20	25.25	25.41	24.84	24.65

Table B.2: DAO observations cont.

Date (UT)	Object	Exp. (s)	Δ (AU)	r_H (AU)	V (mag)	$\log Q$ (mol s^{-1})			
						CN	C_3	C_2 ($\Delta v = 1$)	C_2 ($\Delta v = 0$)
	176	2400	2.828	1.918	12.26	25.57	25.90	25.76	25.92
	430	3600	2.389	1.829	14.60	24.81	24.71	24.76	24.96
2007 Aug 16	3163	3600	1.607	0.622	14.38	24.20	23.82	23.72	23.80
	3628	1800	1.782	0.914	14.77	24.28	24.20	24.17	24.18
	46436	3600	1.833	0.876	14.77	25.19	24.45	23.97	24.09
	7870	3600	1.884	0.885	14.94	24.32	24.18	24.19	24.26
2007 Aug 18	455	1800	2.606	1.857	13.64	25.10	25.38	25.20	25.23

Curriculum Vitae

Alyssa M. Gilbert (née Moldowan)
Department of Physics and Astronomy
The University of Western Ontario
London, Ontario, Canada
N6A 3K7

Education

Bachelor of Science (Physics)	University of Calgary Department of Physics and Astronomy Calgary, AB, Canada 1997-2002
Master of Science (Astronomy)	University of Manitoba Department of Physics and Astronomy 2003-2005
Doctorate of Philosophy (Astronomy)	University of Western Ontario Department of Physics and Astronomy London, ON, Canada 2005-2009

Awards

Ontario Graduate Scholarship in Science and Technology	2008/05 - 2009/04
Ontario Graduate Scholarship in Science and Technology	2007/05 - 2008/04
Western Graduate Research Scholarship	2005/09 - 2009/05
Western Graduate Thesis Award	2008/01
Western Graduate Thesis Award	2006/01

Related work experience

May 2006 - May 2009	Program Coordinator, Exploring the Stars University of Western Ontario, London, ON Supervisor: Dr. M. Campbell-Brown
Jan. 2004 - Aug. 2009	Program Coordinator, Let's Talk Science University of Western Ontario, London, ON; University of Manitoba, Winnipeg, MB Supervisor: S. McKee
Sept. 2005 - May 2006	Teaching Assistant University of Western Ontario, London, ON Supervisors: Dr. A. Sigut, Dr. K. Kaluarachchi, Dr. P. Brown
Sept. 2003 - May 2005	Teaching Assistant University of Manitoba, Winnipeg, MB Supervisor: I. Cameron
Apr. 2003 - July 2003	Summer Research Assistant University of Manitoba, Winnipeg, MB Supervisor: Dr. S. Safi-Harb
May 2000 - Sept. 2000	Summer Research Assistant University of Calgary, Calgary, AB Supervisor: H. Graumann

Publications

Journal articles

Gilbert, A., Wiegert, P. 2009, Searching for main-belt comets using the Canada-France-Hawaii Telescope Legacy Survey. *Icarus* 201, 714-718.

Gilbert. A., Wiegert, P., Undo-Sanzana, E., Vaduvescu, O. 2009, Spectroscopic observations of new Oort cloud comet 2006 VZ13 and four other comets. Submitted to *MNRAS*.

Moldowan, A., Safi-Harb, S., Fuchs, Y., Dubner, G, 2005, A multi-wavelength study of the western lobe of W50 powered by the galactic microquasar SS 433. *AdSpR* 35, 1062-1065.

Conference proceedings

Moldowan, A., Wiegert, P. 2008. More results from the CFHTLS search for main-belt comets. *BAAS* 40 (Ithaca, NY) p.493.

Moldowan, A., Wiegert, P. 2008. Continuing the Search for Main Belt Comets with the CFHT Legacy Survey. *LPI* 1405 (Baltimore, MA) 8026.

Moldowan, A., Wiegert, P., Moss, A. 2007. Searching for Main Belt Comets with the CFHT Legacy Survey. *BAAS* 39 (Orlando, FL) p.525.

Moldowan, A., Safi-Harb, S. 2005. Chandra and RXTE Study of the Western Lobe of W50 and Galactic Microquasar SS 433. *JRASC* 99 (Montreal, QC) p.141.

Moldowan, A., Safi-Harb, S. 2004. RXTE and Chandra Study of SS433/W50. *BAAS* 36 (New Orleans, LA) p.939.